Masteroppgave

NTNU
Norges teknisk-naturvitenskapelige universitet
Fakultet for informasjonsteknologi og elektroteknikk
Institutt for elkrafteknikk

Ingrid Nytun Nergård

Detection and diagnosis of field-joint fault and static eccentricity in synchronous generators through analysis of the stray magnetic field.

Masteroppgave i Energi og Miljø
Veileder: Arne Nysveen
Medveileder: Hossein Ehya
Juni 2023

NTNU
Kunnskap for en bedre verden

Ingrid Nytun Nergård

Detection and diagnosis of field-joint fault and static eccentricity in synchronous generators through analysis of the stray magnetic field.

Masteroppgave i Energi og Miljø
Veileder: Arne Nysveen
Medveileder: Hossein Ehya
Juni 2023

Norges teknisk-naturvitenskapelige universitet
Fakultet for informasjonsteknologi og elektroteknikk
Institutt for elkraftteknikk

NTNU
Kunnskap for en bedre verden

Abstract

This Master's thesis investigates the fault signatures of field-joint fault and static eccentricity in the external magnetic field of salient-pole synchronous generators. The results were obtained from finite element modelling and simulations of two generators. The findings were also tested and examined using stray flux data from real hydroelectric generators.

The Master's work was initiated by a preproject. The motivation for the preproject was to investigate fault signatures from frayed field-joints in the stator core of salient-pole synchronous generators, in the stray magnetic field. Through simulations, it was discovered that faulty field-joints alter the voltages induced in stray flux sensors. Furthermore, the voltage alterations have similarities to static eccentricity, as neither of the faults change the magnetic field's frequency spectrum. These findings substantiated an expansion into a Master's thesis.

The Master's work continued the research on field-joints and incorporated the study of static eccentricity. It also further investigated the properties of static eccentricity in the stray magnetic field, with the intent of determining the severity and position of a static eccentricity fault. The method developed to compute the severity percentage, exploited the RMS voltage difference in four sensors, with absolute errors ranging from 0 % to 35 %. The angle was computed using time-series data mining and the radius of gyration, computed from the same sensors, with absolute errors ranging from 0° to 50°. The results were collected from simulated models generated with the finite element method. It was evident that both methods had the lowest and most stable errors in the models without field-joint fault. It was concluded that field-joints have a larger impact on the stray magnetic field than static eccentricity, particularly near the field-joints. Additionally, it was discovered that the presence of static eccentricity does not aggravate or disturb the identification of faulty field-joints.

Finally, an algorithm was developed to distinguish field-joint fault and static eccentricity from other synchronous generator faults. The algorithm can also be used to determine the severity and angular position of the static eccentricity, although results may be ambiguous. This algorithm contributes to facilitating the health diagnosis of synchronous generators. Future research, however, should focus on establishing methods with higher precision, particularly for calculating the severity of a static eccentricity fault.

Sammendrag

Denne masteroppgaven undersøker feilsignaturene til deleskjøtfeil og statisk eksentrisitet i det ytre magnetfeltet til en synkrongenerator med utstikkende poler. Resultatene ble oppnådd ved finite element-modellering og simuleringer av to generatorer. De trukkede konklusjonene ble også testet på fluksdata fra det ytre magnetfeltet til ekte vannkraftgeneratorer.

Masterarbeidet ble initiert med et forprosjekt. Motivasjonen bak forprosjektet var å undersøke feilsignaturen til slitte deleskjøter i statorkjernen til synkrongeneratorer med utstikkende poler, i det ytre magnetfeltet. Gjennom simuleringer ble det oppdaget at slitte deleskjøter endrer de induserte spenningene i sensorene som måler ekstern magnetisk fluks. Videre ble det oppdaget at endringene har likheter til statisk eksentrisitet, ettersom ingen av feilene endrer magnetfeltets frekvensspektrum. Disse funnene underbygget argumentet for å utvide forprosjektet til en masteroppgave.

Forskningen til masteroppgaven har videreført arbeidet med deleskjøter, og innarbeidet en studie av statisk eksentrisitet. Egenskapene til statisk eksentrisitet i det ytre magnetfeltet har blitt undersøkt, med den hensikt å bestemme alvorlighetsgrad og posisjon til en statisk eksentrisitetsfeil. Metoden utviklet for å bestemme alvorlighetsgraden i prosent, utnyttet forskjellene i RMS-spenninger i fire sensorer, med absoluttfeil fra 0 % til 35 %. Vinkelen ble beregnet ved tidsseriedatautvinning og gyradius, beregnet fra de samme sensorene, med absoluttfeil fra 0° til 50°. Resultatene ble hentet fra simulerte modeller laget med finite element-metoden. Det var tydelig at begge metoder hadde lavest og mest stabil feil i modellene uten deleskjøter. Konklusjonen var at deleskjøter har større påvirkning på det ytre magnetfeltet enn hva statisk eksentrisitet har, særlig i umiddelbar nærhet av deleskjøtene. Videre ble det oppdaget at tilstedeværelse av statisk eksentrisitet hverken forverrer eller forstyrrer identifiseringen av feil på deleskjøtene.

Til slutt ble en algoritme utviklet for å kunne skille deleskjøtfeil og statisk eksentrisitet fra andre synkrongeneratorfeil. Algoritmen kan potensielt også brukes til å bestemme vinkelposisjon og alvorlighetsgrad til statisk eksentrisitet, selv om resultatene kan være tvetydige. Denne algoritmen bidrar til forenklet diagnostikk av synkrongeneratorhelse. Fremtidig forskning bør likevel fokusere på å etablere metoder med bedre presisjonsgrad, særlig for å bestemme alvorlighetsgraden til en statisk eksentrisitetsfeil.

Preface and acknowledgement

This Master's thesis represents the final chapter of my time as a student in the five year study program Energy and Environment ("Energi og Miljø"), culminating in a Master's degree in electrical power engineering from the Norwegian University of Science and Technology (NTNU). Initiated with an introductory project in the autumn of 2022, the Master's work began in earnest in January of 2023 and is completed in June this same year. Excluding the preproject, it is weighted 30 credits.

As I now approach the finish line, or perhaps the light at the end of the tunnel, I cannot help but reflect back on the ups and downs of this five year journey. The memories are mostly happy ones, like when I think about all friends and connections made, but I have also spent many a long evening struggling to understand complex concepts, and failed to do so, and I have doubted myself more than ever before in my life. Nevertheless, here I am now with a Master's thesis, whatever that is worth. I congratulate you, dear reader, on making it this far, and wish you luck and joy getting through the rest of it.

Before delving into the many wonders of synchronous generator health diagnostics, one thing has to be made very clear: I would never have been able to write this thesis without the help and support of many wonderful people. Some are not mentioned, and for that I apologize. Hope you don't mind. For the lucky rest:

I want to thank my two supervisors, Arne Nysveen and Hossein Ehya, from the bottom of my heart. Arne, thank you for sharing your enthusiasm about generators. It is refreshing to work with someone with such a strong passion for their field. Hossein, thank you for your guidance and patience, for providing knowledge and background literature for me to read, and for answering my silly little questions. Sorry for the times I knocked at your door when you were in the middle of something.

I also want to say thank you to the guys at Statkraft, who generously accommodated for me (and Hossein) to visit their hydropower plants. Thank you to Anders, who even drove me there. I also appreciate the time and knowledge shared by Per Einar, who guided us through the power plants, explaining the functioning and challenges of the specific generators. My practical understanding increased a lot that day thanks to you two! A sincere thank you to Kristoffer, who joined Hossein and me for the field test, which ended up taking a lot more time than initially anticipated. I hope some of the findings presented in this thesis can be of value to you all.

Table of contents

List of tables

List of figures

List of abbreviations

2D	=	two-dimensional
3D	=	three-dimensional
abs	=	absolute value
asym	=	asymmetric
ASYM TIGHT	=	asymmetric tight field-joint
ASYM LOOSE	=	asymmetric loose field-joint
deg	=	degrees
DFT	=	discrete Fourier transform
E	=	east
emf	=	electromotive force
EX	=	expected value
FEM	=	finite element method
FFT	=	fast Fourier transform
FJ	=	field-joint
FT	=	Fourier transform
IG	=	industrial generator
mmf	=	magneto-motive force
N	=	north
NE	=	northeast
NTNU	=	the Norwegian University of Science and Technology
NW	=	northwest
PDE	=	partial differential equation
RMS	=	root mean square
RoG	=	radius of gyration
rpm	=	revolutions per minute
S	=	south
SD	=	standard deviation
SE	=	static eccentricity OR southeast
SEFJ	=	static eccentricity and field-joint fault
SEV	=	severity
SSE	=	error sum of squares
SYM	=	symmetric field-joints
SV	=	space vector
SW	=	southwest
TSDM	=	time-series data mining
W	=	west

List of symbols

A	=	magnetic vector potential
B	=	magnetic flux density
d	=	thickness of one stator laminate
D	=	electric displacement field
E	=	electric field
EX	=	expected value
emf, F	=	electromagnetic force
f	=	time-dependent function
F	=	Fourier-transform of f
$\mathcal{F}$	=	Magnetomotive Force (MMF)
H	=	magnetizing field
i, I	=	current
j	=	imaginary number
J_f	=	free current density
K	=	attenuation factor between the air gap and the stray magnetic field
K_e	=	a constant related to the calculation of eddy-current losses
l	=	physical length or time lag
m, L	=	variables related to time-series data mining
n	=	counting variable
$\hat{n}_F$	=	unit vector of direction equal to a force $\vec{F}$
N	=	number of turns in a winding or number of elements in a sequence
n_s	=	rotor synchronous speed
p	=	pole pairs
ΔP_e	=	eddy-current losses
P_n	=	nominal power
Q	=	quadrant
r	=	radius of gyration
$\mathcal{R}$	=	magnetic reluctance
S	=	a surface or sensor
SD	=	standard deviation
SEV	=	severity
SSE	=	error sum of squares
SV	=	space vector
t	=	time
V	=	voltage
y	=	linear model
x	=	discrete values
X_k	=	discrete Fourier transform of $\{x_n\} = \{x_0, x_1, ..., x_N\}$

α	=	share of an angle
β	=	line coefficient or share of an angle
Γ	=	volume
μ	=	magnetic permeability
ρ	=	material density
ρ_f	=	electric charge density
σ	=	material conductivity
Σ	=	surface
θ	=	angle
$\boldsymbol{\phi}$	=	magnetic flux
ω	=	rotational speed

Subscripts

air	=	air material
el	=	electrical
ext	=	external
FJ	=	field-joint
fm	=	ferromagnetic material
int	=	interior
m	=	mechanical
n	=	counting variable
r	=	rotor or relative or radial component
$r, stray$	=	radial component of stray magnetic field
rn	=	normal component of a radial component
s	=	stator
Si	=	silicon steel material
x	=	horizontal axis (abscissa)
y	=	vertical axis (ordinate)

Chapter 1

Introduction

This first chapter serves as an introduction to the Master's thesis. It contains some useful and hopefully interesting background information on the thesis topics, as well as information about the work methods, and it outlines the most evident thesis limitations. The final page of the chapter presents an overview of the thesis structure, with a concise description for each chapter.

1.1 Project motivation

Synchronous generators, and more specifically salient-pole synchronous generators, are substantial in the production of hydroelectricity. In Norway, more than 85 % of the electricity is produced from hydropower [1]. Given electricity's integral role in a functional society, it is crucial that the generators are healthy and maintenance performed regularly. Faults must be detected and treated in the early stage, to prevent irreversible damage. As synchronous generators often are custom-made for their specific purpose, part replacement is costly and only performed when necessary.

Hydroelectric generators that were manufactured for the Norwegian market before approximately the year 2000, may feature field-joints in the stator core. These joints are a product of core segmentation for transportation purposes, from a workshop to the production site. After years of operation the field-joints get frayed and weakened, which has led to increased vibrations in some generators [20]. Frayed insulation between field-joints may also cause short circuit currents and undesired heating in the generator. As little research has been conducted on this subject, more scientific investigation is necessary to facilitate detection of faulty field-joints in an early stage. Challenges regarding the field-joints, in addition to economic considerations, are reasons why hydroelectric generators manufactured for Norwegian power plants no longer have field-joints in the stator core [22].

In recent years, the hydropower industry has witnessed a demand for an efficient fault detection technique capable of discovering generator faults in the early stage. A pioneering, yet straightforward, method has been proven effective on various machine faults. The method involves the use of magnetic sensors to measure a generator's stray magnetic field. The results can be analyzed

to deduct what type of faults the generator might have. As a noninvasive method that does not require a significant amount of downtime [4], it has significant potential.

During the preproject leading up to this Master's thesis, faults in the field-joints of a synchronous generator were explored using the aforementioned method. It was discovered that the fault signature of frayed field-joints exhibit properties similar to static eccentricity, another typical fault in synchronous generators. Therefore, a significant portion of this thesis work has been dedicated to discover the expression of static eccentricity in the stray magnetic field, and discerning it from other faults.

In the upcoming chapters, this work seeks to enhance the scientific understanding of these faults, and their signature on the stray magnetic field, contributing to a development of more efficient and cost-effective maintenance practices for hydroelectric generators.

1.2 Project objective and work method

This Master's Thesis is a continuation of the specialization project that was conducted in the fall of 2022 [2], which initiated the research on field-joint fault detection by means of stray magnetic field analysis. The aim of the project is to advance the field of synchronous generator health diagnosis by developing a method for early detection and characterization of two specific faults in salient-pole synchronous generators: field-joint fault and static eccentricity. It further intends to distinguish between these faults using the unique signatures they produce in the stray magnetic field.

The work method adopted for this project has been iterative and empirical. Data has been collected from both computer simulated models of faulty generators, and from stray magnetic field sensor measurements of actual generators exhibiting potential faults. The data was analyzed using a combination of simple and more advanced pattern recognition techniques. The goal was to identify unique signatures associated with each type of fault, and distinguish between them. Finally, an algorithm was developed based on the research findings. The algorithm aims to detect the two faults, and if possible differentiate between them, based on sensor measurements of the generator's stray magnetic field.

1.3 Thesis limitations

This study has several limitations that should be taken into consideration while reading the thesis. First, the computer simulated models of the generators were idealized and do not fully capture the complexities in real-world generators. The major simplification procedure was to only analyze two-dimensional models and ignore three-dimensional effects during the model simulations. The faults introduced in the models were also idealized, and may not inflict the same fault dissipation as they would in a real generator. Also, while the magnetic sensors used to perform the generator

field test were highly sensitive, they may not capture every aspect of the stray magnetic field alterations caused by the faults.

Next, the sample size of both simulated generator models and real-world generators exhibiting faults was limited, which might deteriorate the generalizability of the conclusions. The reader should also remember that this study focuses only on two specific faults in synchronous generators: field-joint fault and static eccentricity fault. The full list of potential issues is a lot longer, and a more extensive study would be required to form a sufficient picture of the health of an actual synchronous generator.

Finally, the methods and algorithm developed in this thesis work is based on the data collection from models of two specific generators. Other generators may have different design and performance specifications, which cause their stray magnetic field to react differently to faults. The performance of the methods and algorithm may therefore vary when applied to data from other generators with different types of faults.

1.4 Report outline

Chapter 1: Introduction serves as an introduction to the work presented in this Master's thesis, including some background information and motivation on the problem, the project objective, and the main limitations which restrict the results.

Chapter 2: Theory chapter is a theory chapter, containing the most relevant theory background necessary to be able to understand the subsequent work methods and results.

Chapter 3: Modelling and simulations describes the generators, and the software used to model the generators and the electromagnetic fields. The process of fault application is explained. Tables of all the simulations conducted are presented.

Chapter 4: Pattern recognition methods explains in detail the five main pattern recognition methods used to analyze the voltages induced in the stray magnetic field sensors. The first method originates from the preproject. The next four are new to this Master's project.

Chapter 5: Pattern recognition results on simulated models presents the results obtained when the methods from the previous chapter are carried out on the simulations of the laboratory generator and industrial generator models.

Chapter 6: Stray flux test on field-joints in a synchronous generator describes a field test performed on the field-joints of an operative synchronous generator with salient poles. The generator is suspected to have field-joint fault. The test method is accounted for, along with the test results.

Chapter 7: Stray flux test on static eccentricity in two generators presents the obtained results from static eccentricity pattern recognition methods attempted on field test measurements. Data from two generators are analyzed.

Chapter 8: Discussion of results contains the analyses and discussions necessary to interpret the results obtained in chapter 6, 7 and 8. An algorithm is presented to distinguish field-joint fault from static eccentricity fault by means of the methods developed in the Master's work. Finally, some natural next research step are presented.

Chapter 9: Conclusions is the concluding chapter. It summarizes the main findings and conclusions discovered throughout the work of this Master's thesis.

Chapter 2

Theory chapter

This chapter presents the core theoretical principles relevant to the thesis work, which are integral to understand the obtained results and conclusions. Advanced concepts and equations related to electromagnetism and the field of synchronous generators are explained in a direct manner, with a focus on comprehension rather than intricate detail knowledge. The analysis tools employed for pattern recognition are accounted for and briefly explained.

2.1 Introduction to magnetic circuits and magnetic induction

Electromagnetic energy conversion is the foundation behind electric machines and their functioning. Therefore, some repetition on the fundamental knowledge about electromagnetics is essential before explaining the operation of a synchronous generator.

2.1.1 Magnetic circuits

A simple magnetic circuit is given in figure 2.1a. It shows an excitation winding with N turns wound around a gray material. The gray material is ferromagnetic, which means that it can be magnetized. The winding is excited with a current i. The current through the wound coil is the reason for a force $\mathcal{F}$, also known as the magnetomotive force (mmf). This force establishes a magnetic field $\vec{H}$, governed by ampere's law and in direction according to the right hand rule. Ampere's law in the form relevant for this explanation is given in equation (2.1). It states the relationship between the current i and a magnetic field $\vec{H}$ on some path $\vec{l}$. Here, l is the mean path around the ferromagnetic material, marked as a stippled line in figure 2.1a.

$$\mathcal{F} = Ni = \oint_l \vec{H} \cdot d\vec{l} \tag{2.1}$$

The magnetic field depends on the a quantity $\vec{B}$ called the magnetic flux density, the permeability μ_r of the ferromagnetic material and the permeability of vacuum μ_0, as given in equation (2.2). Permeability is a value that indicates how susceptible a material is to magnetization.

$$\vec{B} = \mu_0 \mu_r \vec{H} \tag{2.2}$$

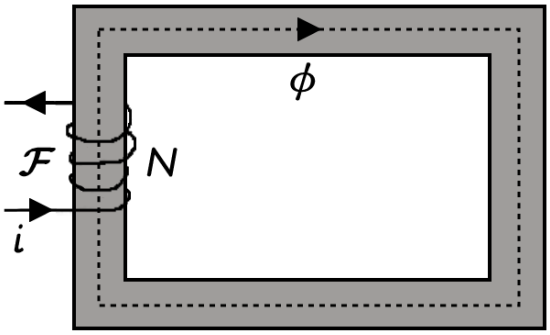

(a) The simplest magnetic circuit: A force $\mathcal{F}$, current in a coil with N turns, drives a magnetic flux ϕ in a ferromagnetic material.

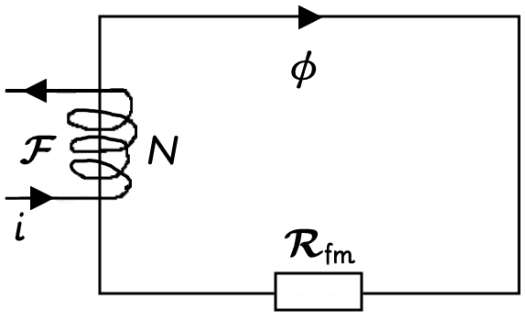

(b) The magnetic circuit equivalent of **(a)**. The ferromagnetic material is represented as magnetic reluctance $\mathcal{R}_{fm}$.

Figure 2.1: The simplest magnetic circuit in **(a)**, and its circuit equivalent in **(b)**.

The permeability of vacuum μ_0 is a constant given by $\mu_0 = 4\pi \cdot 10^{-7}$, while the relative permeability of a ferromagnetic material μ_r is typically a value between 2000-6000 [8]. The relative permeability of both vacuum and air is approximately $\mu \approx 1$. As the permeability is a property that states how easily a material is magnetized, one understands that ferromagnetic materials are magnetized a lot easier than vacuum and air.

The magnetic flux density $\vec{B}$ is, as stated in the name, a density. The magnetic flux density summed up on a surface S is called the magnetic flux ϕ, defined as in equation (2.3). With this, one can begin the discussion of magnetization as a quantity. From equation (2.2), one understands that most of the magnetic flux activated by the mmf is located in the ferromagnetic material. A small part, called the leakage flux, still flows outside of the magnetic material. In this introductory review, the leakage flux is neglected and all flux is assumed to flow in the ferromagnetic path.

$$\phi = \int_S \vec{B} \cdot d\vec{S} \tag{2.3}$$

With all flux assumed to flow in the ferromagnetic material, the magnetic field strength can be averaged to a constant value H_{ave} along the mean material length l_{ave}. This reduces equation (2.1) to $\mathcal{F} = Ni = H_{ave} l_{ave}$ and equation (2.3) to $\phi = B_{ave} S_{ave}$. From this, one can observe that the magnetic flux is inversely proportional to the mmf. The ratio constant $\mathcal{R}$, given in equation (2.4), is called the reluctance. The inverse of the reluctance is called the permeance $\mathcal{P}$.

$$\mathcal{R} = \frac{\mathcal{F}}{\phi} = \frac{l_{ave}}{\mu_0 \mu_r S_{ave}} = \frac{1}{\mathcal{P}} \tag{2.4}$$

From the relationship $\mathcal{F} = \mathcal{R}\phi$, one can draw an analogy from the magnetic circuit to an electric circuit governed by ohm's law $V = RI$. The mmf $\mathcal{F}$ here corresponds to the voltage V, the magnetic flux ϕ to the current I and the reluctance $\mathcal{R}$ to the resistance R. With the electrical analogy, a magnetic circuit can be drawn in a circuit diagram just like an electric circuit, as shown in figure 2.1b.

2.1.1.1 B-H relationship and magnetic saturation

The linear relationship $\mathcal{F} = \mathcal{R}\phi$ is valid as long as the relative permeability μ_r is constant. However, this is not always the case for ferromagnetic materials. This is due to the composition of the materials: ferromagnetic materials consist of microscopic domains made out of orientable dipole grains. Each dipole has its own tiny magnetic field. When exposed to an external magnetic field, the dipole grains are oriented in the direction of the field. This is effectively magnetization. Before the mmf is imposed on the material, the domains are randomly oriented. The magnetic field of the dipoles are cancelled out by other dipoles. As the mmf magnetizes the material, the fields no longer cancel out. Instead, they align and combine their fields to a total magnetic field which may extend the material. The stronger the applied mmf, the more dipoles are oriented, until effectively they are all as aligned as possible. When this occurs, the material is said to have reached saturation.

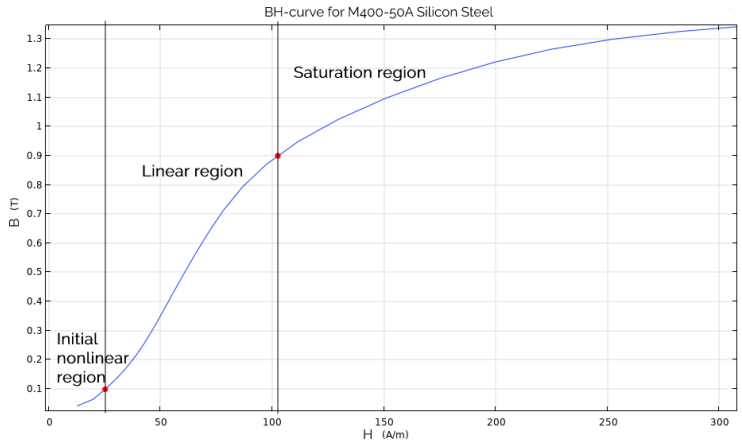

Figure 2.2: BH-curve for a type of silicon steel.

On figure 2.2, the B-H relationship curve for a ferromagnetic material (silicon steel) is pictured. One can observe that after a certain strength in the applied magnetic field H, there is hardly any increase in magnetic flux density B. This is where the material reaches saturation. The linear region, where the assumption $\mathcal{F} = \mathcal{R}\phi$ holds because $\mu_r = \frac{H}{B}$ is approximately constant, is marked between the two red dots on the curve.

2.1.2 Magnetic induction

A time-varying magnetic flux through a winding with N turns induces an electromagnetic force (emf) on the winding governed by Faraday's law of induction, for this purpose presented as in equation (2.5).

$$emf = -N\frac{d\phi}{dt} \tag{2.5}$$

The negative sign in equation (2.5) implies that the direction of the emf opposes the direction of the current inducing the magnetic flux.

The magnetic flux can be time-varying through the winding in several ways. One way is to have a constant flux, and physically move the winding. Another way is to keep the winding physically still, but make the magnetic flux vary with time by inducing it through an alternating current. A third way is to combine the two methods. These practices are utilized in the theory behind electromagnetic energy conversion in electric machines, which is further elaborated in section 2.2.2.

The electromagnetic force acting in the magnetic field is called Lorentz force [16]. When acting on an electric conductor leading current I in a uniform magnetic field, the total force $\vec{F}$ can be defined as in equation (2.6). Here, l is the length of the conductor and $\sin\theta$ is the angle between the direction of the magnetic field and the conductor. In machine configurations, this angle is often 90°, reducing the term to 1 [8]. The term $\hat{n}_F$ is a unit vector in the direction of the force.

$$\vec{F} = I\vec{l} \times \vec{B} = BIl \cdot \sin(\theta) \cdot \hat{n}_F \tag{2.6}$$

Because of the cross product in the equation's middle term, one understands that the direction of the force can be found by the left hand rule. The equation is fundamental for the generation of torque in electrical machines [16].

2.2 Synchronous generators

Electric generators convert mechanical energy to electric energy. The most common type of generator to generate electric power is the synchronous generator. These next sections explain the most common concepts for physical structure, function and electromagnetic theory of synchronous generators.

2.2.1 Key components and functionality of a salient-pole synchronous generator

A cross-sectional view of a salient-pole synchronous generator with the naming of the different parts included is presented in figure 2.3. There are, naturally, many more parts that could be included or more detailed in a more accurate model. However, for the purpose of the analysis presented in this thesis, the parts pictured in figure 2.3 have been deemed sufficient and thus these parts are given the most attention. The purpose of the different parts are explained in the following paragraphs.

An electric machine's two main components are the rotor and the stator. The rotor is a rotating part, and is in a synchronous generator typically enclosed within the stator as in figure 2.3. The stator is a static part, and typically the outer part. The space between the rotor and the stator is called the air gap. This gap is crucial for rotor rotation to be possible, as the friction between rotor and stator otherwise would be too high.

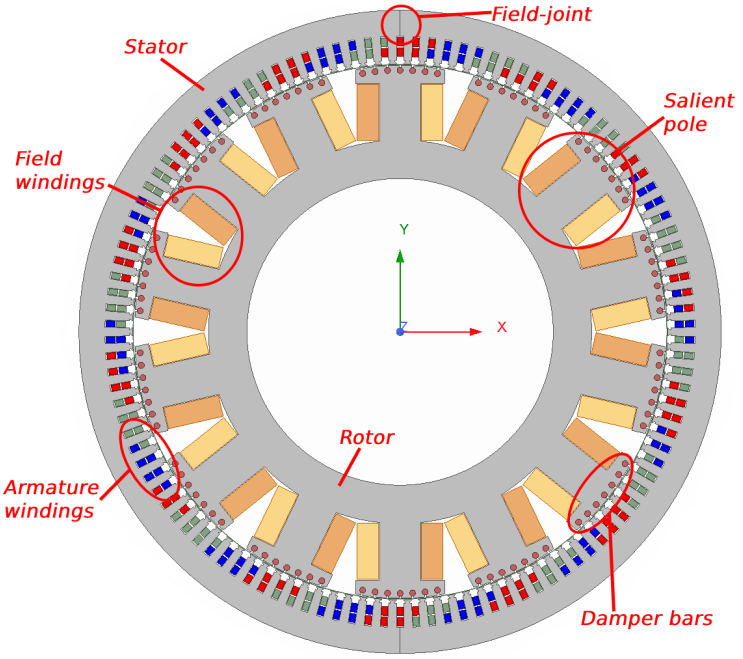

Figure 2.3: Illustration of a salient-pole synchronous generator, with naming of the most important components.

Synchronous generators operate on the principle that the rotational speed of the rotor is the same as the speed of the rotating magnetic field in the stator. The synchronous speed n_s is set by the electrical frequency and the number of poles, given by equation (2.7), where c is the electrical frequency and p is the number of pole pairs. Equation (2.7) gives the synchronous speed in number of rotations per minute (rpm).

$$n_s = \frac{60c}{p} \tag{2.7}$$

The synchronous machine's driving field is induced from direct currents that are applied to the rotor windings, also called the field windings. The field windings are the yellow rectangular blocks on figure 2.3. Field windings can also be observed on figure 2.4. The direct currents induce a magnetic flux which flows in paths around the poles, as indicated in the dotted lines in figure 2.4a. An external mechanical force causes the turbine to rotate. The turbine is connected to the rotor through the shaft, and thus the force also rotates the rotor. In the case of a hydroelectric generator the mechanical force is falling or running water. The direct currents produce a magnetic field, which rotates at the same speed as the rotor.

The windings on the stator are called the armature windings. They are the blue, red and green blocks on the stator in figure 2.3. The armature windings are three-phase windings wound for the same number of poles as the rotor. Each phase winding is represented by one color (red, green or blue) on figure 2.3, and each phase winding is placed 120 electrical degrees apart. When a balanced three-phase current flows in the armature windings, a rotating magnetic field is produced. The speed of the rotating magnetic field is the same as the synchronous speed because of the way it is wound.

Synchronous generators can mainly have two different types of rotors: salient-pole type or cylindrical rotor. A salient-pole rotor has protruding poles as in figure 2.4a. These types of synchronous machines are best suited for low rotational speed and a high number of poles. By low rotational speed is meant less than 1000 rpm [3]. salient-pole rotors are cheaper to manufacture than the cylindrical type, and a high number of poles is advantageous when producing a clean 50 Hz stator current [3]. For these reasons, most hydroelectric generators are salient-pole generators [6]. As is also marked on the illustration, the generator in figure 2.3 has a rotor with salient poles. The other type of rotor is the cylindrical type, illustrated in figure 2.4b, which may also be called a turbo generator. This rotor type is better suited for higher rotational speed because of its more aerodynamic shape, which leads to lower windage losses in the air gap than a salient-pole rotor [3]. It normally has only two or four poles.

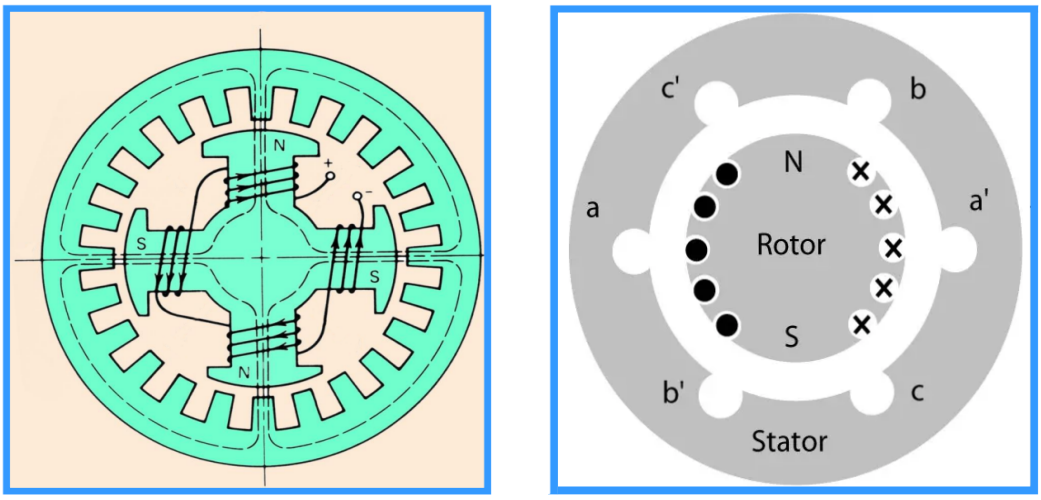

(a) Illustration of a salient-pole generator. The dotted lines represent the magnetic flux circuit path.

(b) Illustration of a generator with a cylindrical type rotor. Illustration from [31].

Figure 2.4: Two simple illustrations of synchronous generators, **(a)** of a generator with a salient-pole rotor and **(b)** of a generator with a cylindrical rotor.

It can be observed from equation (2.5) that the shape of the induced emf depends on the shape of the magnetic flux. In synchronous generators it is desirable with a sinusoidal emf and therefore the magnetic flux density distribution should also be sinusoidal. In salient-pole generators this is achieved by shaping the pole shoe, so that the air gap is shortest at the middle of the pole shoe and gradually becomes longer towards the sides [8]. In cylindrical generators it is achieved by means of a distributed field winding.

At the pole shoes of the salient poles on the rotor on figure 2.3, a third type of winding can be observed. This is called the damper bars, or damper winding. This is a short-circuited winding which dampen the oscillatory effect of disturbances in the machine [12]. Disturbances can be e.g. load changes, presence of harmonics in the load, torque changes or mechanical vibrations in the rotor driving force [12]. Rotor oscillations due to these disturbances cause a relative movement of the damper bars with respect to the air gap magnetic field. This induces an emf in the damper

bar opposing the oscillations, as of Faraday's law. One therefore understands that the damper winding contributes to dynamic stability in the generator.

2.2.2 Electromagnetic induction in a synchronous generator

As explained in section 2.1.1, a current in a coil wound around a ferromagnetic material causes a magnetic flux ϕ to circulate the material. In a salient-pole synchronous generator, the coil is wound around the salient poles, as shown in figure 2.4a. The magnetic flux take the path of least resistance and flow mostly in the rotor and stator yokes, following the stippled lines in the same figure. It can also be observed that in order to follow the path of least resistance, the flux splits in half in the stator yoke, flowing either to the left or to the right, before reentering the rotor. To follow this path, the flux must cross the air gap twice. The magnetic circuit for the flux path, as shown in figures 2.5a and 2.5b, must therefore contain air resistance. In figure 2.5a, the length l_{air} thus refer to the total length of air that the flux must cross, which in this case is two times the length of the air gap.

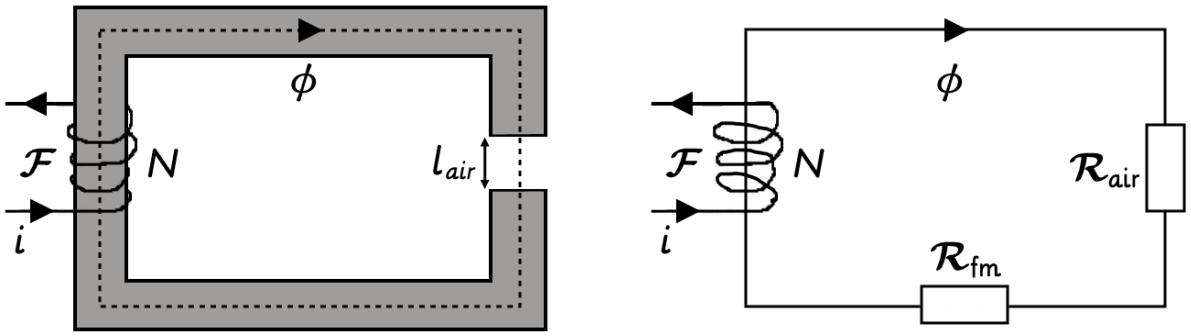

(a) Simple magnetic circuit with air gap.

(b) Magnetic circuit equivalent of the magnetic circuit in **(a)**. The ferromagnetic material and the air gap are represented as $\mathcal{R}_{fm}$ and $\mathcal{R}_{air}$

Figure 2.5: **(a)** Illustration and **(b)** equivalent circuit representation of simple magnetic circuit with air gap. $\mathcal{F}$ is a force, generated by current i through a coil with N turns, driving the magnetic flux ϕ.

As the relative permeability of ferromagnetic material is very different from air, the reluctance of the two materials must be modeled separately. The equivalent magnetic circuit then becomes as in figure 2.5b. A simple expression for the reluctance can be calculated with equation (2.4). A comparison of the two reluctances yields

$$\frac{\mathcal{R}_{fm}}{\mathcal{R}_{air}} = \frac{\frac{l_{fm}}{\mu_0 \mu_{fm} S_{fm}}}{\frac{l_{air}}{\mu_0 \mu_{air} S_{air}}} \approx \frac{l_{fm}}{l_{air} \mu_{fm}} \ll 1.$$

An effect of this relationship is that $\phi \approx \frac{\mathcal{F}}{\mathcal{R}_{air}}$. In analytical calculations the core reluctance can therefore often be neglected [8] as long as the machine is not very saturated.

As defined in Faraday's law of induction, stated in equation (2.5), emf is produced in a time-varying magnetic field. In a synchronous generator, the relative motion between rotor and the

armature stator windings is what produces the emf. In one armature coil, one period of alternating emf is induced when two poles (one pole pair) have rotated past the coil. As the rotor has made a full revolution, the number of emf periods induced in the coil is thus equal to p, the number of pole pairs. The relationship between rotor speed in electrical radians ω and in mechanical radians ω_m is thus $\omega = p \cdot \omega_m$. In the same way, the electrical angle θ relates to the mechanical angle θ_m as $\theta = p \cdot \theta_m$.

Due to the physical design of the pole shoe and the salient-pole winding, the magnetic flux density B is physically distributed (approximately) in a sinusoidal waveform in the air gap. Its period is equal to the distance of one pole pair, a distance called the pole pitch, and it has its peak value $\hat{B}$ at the top of the positive pole (the north pole). The sinusoidal magnetic flux density results in a sinusoidal waveform also in the induced emf. If the magnetic flux has a peak value $\hat{\phi}$, then Faraday's law gives that the RMS value of the induced voltage is $emf = \frac{\omega N \hat{\phi}}{\sqrt{2}}$.

As the peak magnetic flux is limited by saturation properties in the material and the physical dimensions, a high number of turns N may be required to reach a desired voltage output. In order to reach the sufficient number of turns, several coils located closely on the stator may be series connected. This is known as a distributed winding. In comparison, the field winding around the salient poles are not series connected, and are called concentrated windings. The distributed armature winding also has the function that the mmf space wave of each phase becomes sinusoidal in shape.

Because of the winding of the three-phased armature currents and the number of poles on the rotor, the two magnetic fields from the rotor and the stator rotate at the same speed n_s. They are therefore stationary relative to each other. This is the main criteria for the production of torque, because the two fields align. Otherwise, the varying differences between the fields would give a total average torque of zero and therefore no machine output.

2.2.2.1 The fringing effect

The relative permeability of silicon steel is many thousand times higher than the permeability of air. When flux lines pass through a material that is not magnetic, they begin to repel each other [36]. This brings about a bulging in the flux lines when they pass through an air gap, as visualized in figure 2.6a. The effect is called the fringing flux effect, or just the fringing effect. In figure 2.5a, the flux is assumed constant through the magnetic circuit, with a constant cross-section and thus a constant magnetic flux density. As can be seen from figure 2.6a, this is not actually the case in the air gap. In the area around the air gap, due to flux fringing, the cross-sectional area containing the flux grows and with that the magnetic flux density becomes smaller. Empirical results show that the enlarged cross-section can be computed by adding the length of the air gap to each cross-sectional dimension [8]. From this, one also understands that the amount of fringing flux increases with a larger air gap length [36].

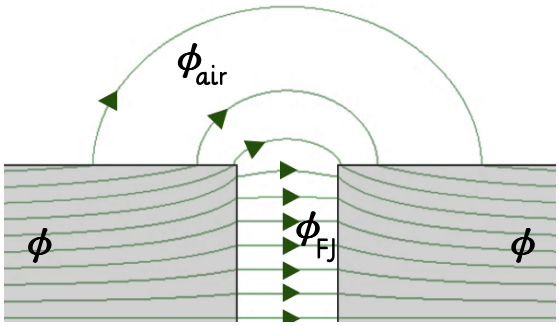

(a) Illustration of the fringing effect. At the boundary between two materials, for example in a field-joint (FJ), some of the magnetic flux goes through the surrounding air. Illustration from [2].

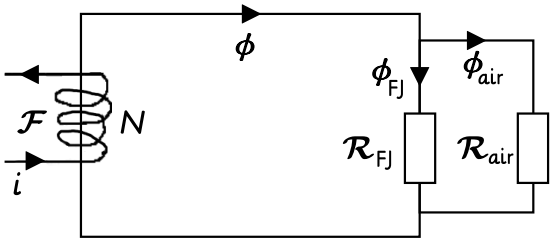

(b) Equivalent circuit drawing of **(a)**. The larger the gap, the larger $\mathcal{R}_{\mathrm{FJ}}$, and more of the flux enters the parallel path.

Figure 2.6: Illustrations of the flux fringing effect in a field-joint, or air gap, in **(a)** as a drawing, and in **(b)** as the equivalent circuit.

A circuit equivalent of the fringing effect is presented in figure 2.6b. The magnetic reluctance in the air gap and in the surrounding air is presented as two resistances connected in parallel. The main gap is named field-joint (FJ) in this illustration, as fringing is also seen in field-joints. When the width of the field-joint, or air gap, increases, so does the magnetic reluctance. Consequently, more flux goes in the surrounding air, through the parallel path in figure 2.6b.

2.2.3 Lamination of the machine core

Figure 2.4a illustrates a cross-sectional view of a salient-pole synchronous generator. However, a real synchronous generator would naturally be a 3D object, as illustrated in figure 2.7. In this figure, the rotor has been moved out of the stator for maintenance. This also allows for a better view of the rotor and stator.

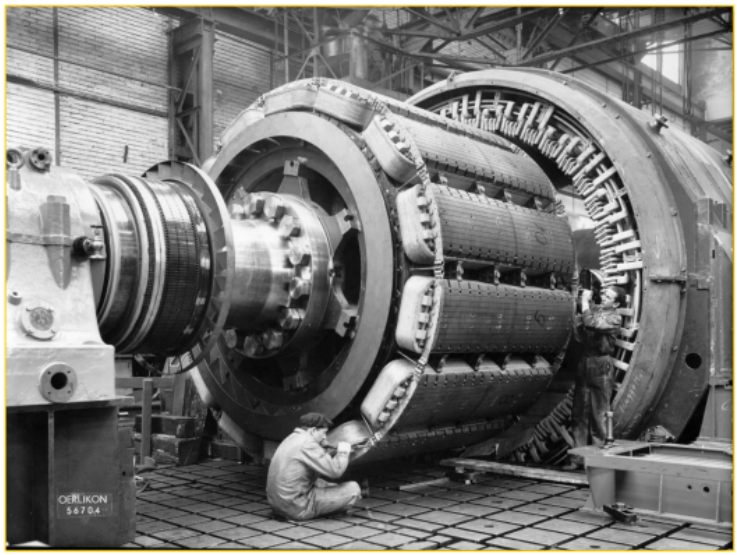

Figure 2.7: Photo of a horizontally installed salient-pole synchronous generator, with the rotor extracted from the stator for maintenance purposes.

The magnetic field between the rotor and the stator circulates following the salient poles, as illustrated in figure 2.4a. Observe how the field only acts in a 2D-plane, and not through the machine core, into the plane. From Faraday's law, for this explanation stated in the form given in equation (2.8), one can observe that a time-varying magnetic field give rise to electric fields. In magnetic materials, the electric fields induce currents, called called eddy currents [48].

$$\nabla \times \vec{E} = -\frac{d\phi}{dt} \tag{2.8}$$

The eddy currents oppose changes in flux density [48]. This generates losses in the form of heat, which can be deduced to the empirical formula given by equation (2.9). In this equation, ΔP_e is the power loss from the eddy currents, K_e is a constant, ρ is the resistivity of the material, c is the frequency, B is the magnetic flux density and d is the length of the machine core. As the losses are a function of the length squared, one understands that the eddy current losses become very large, and even unacceptable, for long machines.

$$\Delta P_e = K_e \frac{d^2}{\rho} c^2 B^2 \tag{2.9}$$

In order to limit the counteraction impact and thus the eddy current losses, the machine core is segmented into thin sheets know as laminates. Each laminate is insulated, typically with varnish or enamel, and they are normally 0.2-0.5 millimeters thick [22]. This reduces the variable d in equation (2.9) considerably, deacreasing the losses related to eddy currents. From equation (2.9), one can also observe how the resistivity of the material affects the losses, and the laminates should therefore be made of a material of suitable resistivity. This is typically some sort of silicon-steel alloy [3].

(a) Stator ring laminates, [29].

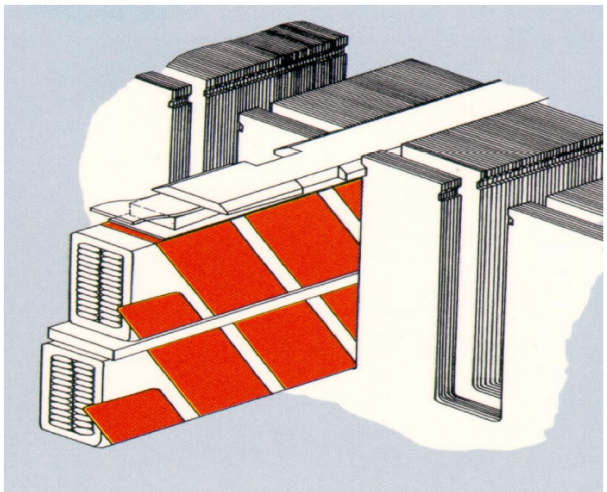

(b) A parallel winding installed in a laminated stator slot.

Figure 2.8: Illustrations of **(a)** ring-shaped stator laminates and **(b)** a parallel winding installed in a laminated stator slot.

Figure 2.8 illustrates the laminates in a segmented stator core. In figure 2.8a, the entire ring segment can be observed. The illustration is retrieved from [29]. There can be hundred of thousands laminates in a large generator core [3]. These ring segments are separately insulated and clamped tightly in the axial direction to form the stator core. It is important that the clamping pressure is applied evenly towards the core centre, to avoid damage and cracking of thin laminates [3]. In figure 2.8b, an enlarged illustration shows the teeth and slots of a laminated stator, with a double layered winding placed in on of the stator slot.

2.2.4 Field-joints in synchronous generators

As already introduced in the project motivation in section 1.1, stator cores in hydroelectric generators are often too large to be transported in one piece. The stator laminates are therefore fabricated as ring segments, which are assembled at the production site. The connection point results in a joint, called a field-joint. Typically, the stator is composed of two to six ring segments [3], [30], and thus have two to six field-joints.

The location of the field-joint depends on the manufacturer of the generator and on the practical history of the companies ordering it. For example, in Norway it was common to have the field-joints through a stator slot and the yoke. In Sweden, on the other hand, the field-joints are typically through a stator tooth and the yoke [20]. There are advantages and disadvantages to both alternatives, which means that there is not a key answer as to which alternative is right. Because this thesis considers hydroelectric generators in Norway, only generators with field-joints through the stator slots and yoke are considered.

After the stator core pieces are transported to the production site, typically inside a mountain, the stator is assembled into one piece. The joints between the stator segments are called field-joints. An insulation material, typically pressboard, is put inside the field-joints, to obstruct short-circuit currents flowing between the laminates. This is because the laminates are not insulated in the vertical lines along the end side of the the laminates. They are insulated between each layer. As the laminates are very thin, it is impossible to install the core parts in such a way that each laminate matches perfectly its corresponding part on the opposing core segment. To avoid currents flowing between the laminates a thin insulating material, often pressboard [22], is put here. The field-joints are then clamped together tightly, to attempt to hinder relative movement between the stator core segments.

(a) Field-joint in a stator core. The paper used as insulation between the stator segments can be observed.

(b) Field-joint in a stator core. The field-joint is the lighter line to the left of the numbers.

Figure 2.9: Field-joints (marked in red) in two different hydroelectric generators.

Figure 2.9 shows a field-joint in two different generators. The pictures are taken from the outside of the stator. As these generators are built in a vertical, "standing" position, what is seen is along the axial length of the stators. In figure 2.9a, the paper used as insulation between the two segments can be seen. If one looks closely, one can see that the paper is slightly frayed and curved due to some uneven stress and heat expansion. Another observation that can be made is the two large bolts which provide clamping pressure over the field-joints. These bolts are installed along the entire axial length of the stator. In figure 2.9b, the field-joint is the lighter line to the left of the numbers. Here, the paper has been cut to fit in the field-joint gap and is therefore not visible on the photo. This field-joint is accessed through a hatch in the stator frame.

2.3 Faults in synchronous generators

Faults in synchronous generators are typically categorized as either mechanical faults or electrical faults [5]. The two types of faults investigated in this thesis are field-joint fault and static eccentricity fault. Therefore, the closest attention is paid to these fault types, which are both mechanical faults. Finally, subsection 2.3.3, is dedicated to other types of faults which typically can occur in a hydroelectric generator. Mechanical faults that can occur are dynamic eccentricity, misalignment, broken damper bars and inter-laminar faults. Electrical faults include stator and rotor short-circuits.

2.3.1 Field-joint fault

The vibrational forces in a hydroelectric generator are of considerable magnitude. Completely hindering all relative movement between the stator core segments is therefore impossible. Various incidents, for instance the loosening of bolts or occurrence of faults such as field-winding short-

circuit fault or a damper winding fault, can lead to an increased vibration level. A certain degree of core slackness is expected to naturally occur over time [30], and it increases with aging of the generator. In due course, heightened vibration levels may deteriorate the pressboard, which insulates the stator core segments on either side of a field-joint. If the insulation disintegrates, the formerly separated segments may come into contact. This could result in short-circuiting of the core laminates, allowing currents to flow as in figure 2.10. A consequence of unregulated current flow is the increase in local temperatures and potentially even fire. In the worst case, the short-circuiting can lead to a meltdown of the core [3].

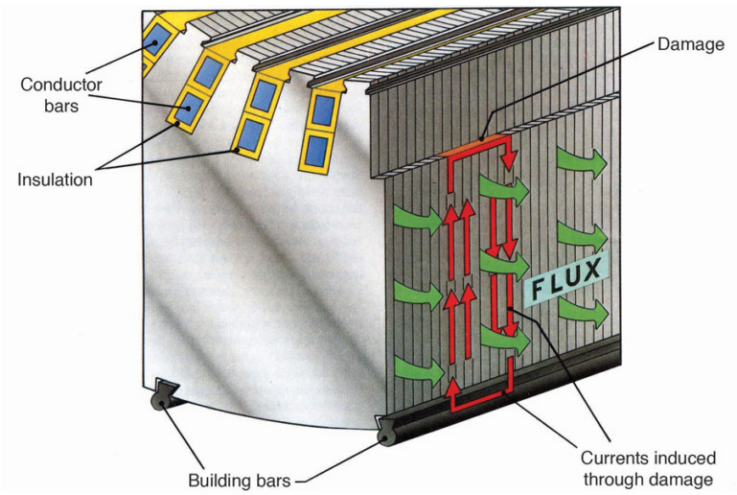

Figure 2.10: Failure of the stator core laminate insulation, which allow for short circuit currents to be induced by the magnetic flux flowing in the core.

The clamping pressure exerted on the field-joints must be sufficient and uniformly distributed across all directions of the stator segments. An insufficient pressure distribution may enable the laminates to vibrate due to the magnetic forces in the generator. This can subsequently lead to degradation of the field-joint insulation, as was already explained in the previous paragraph. Interlaminar-wise, the increased vibrations may cause fretting of the insulating varnish applied to the stacked laminates, thereby potentially short-circuiting the laminates. A temperature increase due to short-circuit currents induced from either damaged laminates or damaged field-joint insulation, could instigate burning and breaking of the laminates, and possibly also cause deterioration of the stator bars [3].

An additional complication inherent to stator core segmentation is uneven thermal expansion between the segments, a phenomenon also referred to as "clover leafing" [30]. The temperature distribution in the stator varies across different regions, potentially leading to different temperatures in the end segments compared to the middle segments. Since the volume of the stator steel expands with the increase of temperature, uneven expansion occurs in regions with different temperature profiles. This thermal expansion leads to a non-uniform stress, with subsequent deterioration, on the field-joint insulation. Additionally, uneven thermal expansion may cause a non-uniform air gap, which leads to unbalanced magnetic pull and an increased level of vibration

[4]. The higher vibrations may then cause an increase in relative movements between the stator segments and thus even more stress on the insulation paper.

2.3.2 Eccentricity fault

An eccentricity fault is a misalignment between the position of the rotor with respect to the stator. Ideally, the rotor would be placed perfectly concentric inside the stator. This creates an equal magnetic pull around the perimeter of the generator, as the air gap has the same length through around the entire machine. If the rotor is not placed exactly in the middle of the stator, the electric machine is said to have eccentricity. In practice all machines have some inherent degree of eccentricity, as it is not possible to keep the rotor perfectly inside the stator. Some degree of inherent eccentricity must therefore also be accounted for and accepted.

Eccentricity can exist in both the radial and axial direction, as depicted in figure 2.11. Axial eccentricity is sometimes just called a misalignment fault. Figure 2.11a shows a model with no eccentricity in neither radial nor axial direction. With only radial eccentricity, as in figure 2.11b, the eccentricity is assumed to be constant along the axial direction and variable in the radial direction. In figure 2.11c, the eccentricity is inconstant both in the radial and the axial directions. As the analyses conducted in this thesis is restricted to concern 2D cross-sectional models, in the remainder of the eccentricity study, only variation in the radial eccentricity will be considered, while the axial eccentricity will be considered constant.

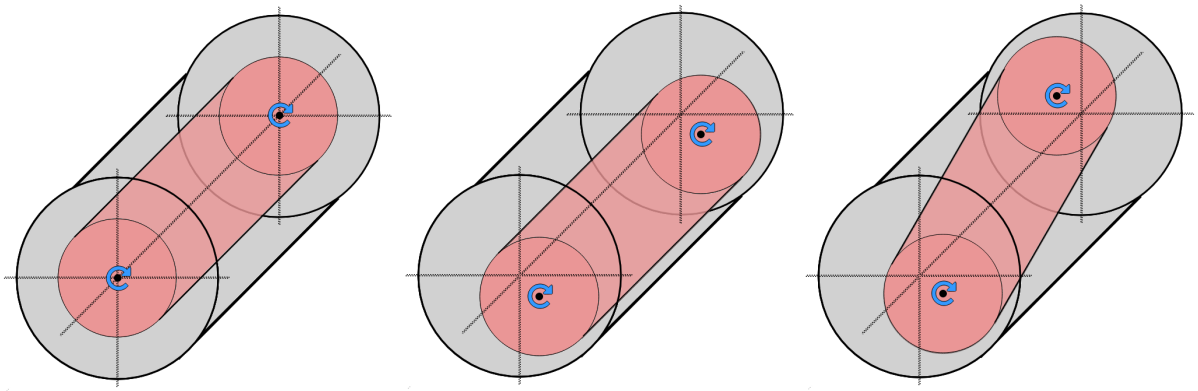

(a) Healthy (no eccentricity). **(b)** Radial eccentricity. **(c)** Axial eccentricity (misalignment).

Figure 2.11: Three-dimensional illustrations of three static eccentricity varieties.

The characteristics of an eccentricity is measured with two variables: the angle and the severity. When those are known, both the position and the degree of severity of the eccentricity are also known. The angle of the eccentricity is the angle at which the air gap is the smallest compared to a reference angle. For example, in figure 2.12b, the angle of the eccentricity is 0° with reference to a standard unit circle in a Cartesian coordinate system, while in figure 2.11b the angle is approximately 315°. Severity is measured in the percentage variation of the air gap at the angle of eccentricity compared to the healthy air gap. For example, a severity of 30 % means that the air gap is 30 % smaller at its smallest point compared to the healthy air gap length.

Even when considering only radial eccentricity, there exist different types of eccentricities. They are presented in figure 2.12. Figure 2.12a shows a healthy model without any eccentricity, where the location and rotational axis of the rotor is concentrically inside the stator. For the case of static eccentricity, in figure 2.12b, both the location of the rotor and of the rotor's rotational axis is moved to a point not concentrically inside the stator. This implies that the severity of the eccentricity is constant at every point around the circumference, and the angle to the point with the highest severity is constant. With dynamic eccentricity, as in figure 2.12c, the location of the rotor is moved, but its rotational axis is still centered concentrically inside the stator. This implies that the angle to the point of the highest severity is not constant, but rather a function of the rotor position. Lastly, and most commonly, the eccentricity can be a mix between static and dynamic, as in figure 2.12d. In this case, the rotor rotates around a point that is not concentrically inside neither the rotor nor the stator.

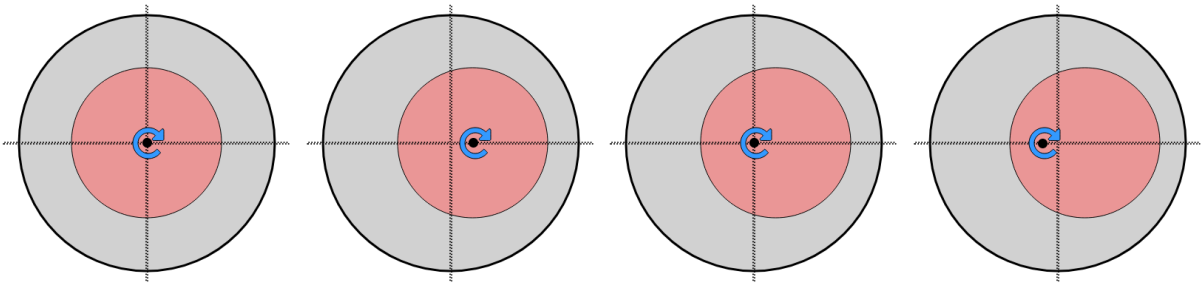

(a) Healthy (no eccentricity). **(b)** Static eccentricity. **(c)** Dynamic eccentricity. **(d)** Mixed eccentricity.

Figure 2.12: Two-dimensional illustrations of four variations of eccentricity.

There can be several reasons why eccentricity occurs. For example, static eccentricity could occur due to bad positioning of the rotor bearing and dynamic eccentricity could occur due to a bent shaft or wearing of the roll bearing [33]. Another reason, typical for hydroelectric generators located inside a mountain, is rock foundation that become unstable due to the large vibrations in the generator [13]. A survey [34] made on induction machines, found that the most typical fault in induction machines were bearing faults, with eccentricity faults as a consequence.

2.3.3 Other faults

As mentioned in the chapter introduction, this subsection is dedicated to give a brief summary of the mechanical and electrical faults, not already explained, which typically occur in hydroelectric generators.

The most severe types of faults to occur in a synchronous machine are electrical faults [4]. The two main types of electrical faults are stator winding and rotor winding short-circuits. Of these two, stator winding short-circuit is the most severe because it rapidly can lead to damage or melting of both the winding and the stator core. It can also lead to a dissolution of particles of the core, which can hit or interfere with other parts of the machine. Rotor winding short-circuits are weaker than stator winding ones, and therefore do usually not destroy the winding as quickly.

Compared to electrical faults, mechanical faults take a longer time to develop [4]. They can still have a severe outcome, as their repair may require replacement of machine parts not easily acquired. Among the mechanical faults, broken damper bars are among the most common. The damper bars on the poles have several roles: they dampen unwanted harmonics and mechanical oscillations, and they allow for a synchronous generator to be self-starting. Due to high starting currents, the damper bars are prone to faults during start-up of the machine [12].

2.3.4 Fault detection in electric machines

Numerous tests can be performed off-line or on-line to detect faults and gather a picture of the health of an electric machine. Maintenance can be corrective, if a fault has already occurred, preventative, which involves time-based testing and is usually recommended, or predictive, which often entails continuous monitoring [3]. Which tests to perform depend on which parts of the machine to analyze, budget, time availability and personnel availability. The age of the electric machine may also have an influence, as older machines tend to require maintenance more often [3]. During maintenance of a machine, a wide range of tests is usually performed, which combine to provide a picture of the total health. Machine operators must decide which tests they want to perform based on a budget, scheduled maintenance time and machine behaviour. Some tests may be performed every six months, other every two years, or based on machine operation hours [3]. This depends on the development time and severeness of the fault that is tested for.

Diagnostic assessments can be performed either on-line or off-line. On-line tests refer to tests that are performed while the machine is in operation. Off-line testing, on the other hand, refer to tests being performed while the machine is only partly in operation or not in operation at all. From an economic perspective, it is most feasible to avoid machine outages and therefore, on-line tests are generally preferred [3]. They also provide data more promptly. However, they may not always furnish a complete understanding, and in some instances they might require supplementation with more comprehensive off-line tests. On-line tests normally require the installation of a greater number of sensors, consequently increasing the capital costs [3].

Maintenance tests can be categorized based on the degree of intrusion they require, namely either invasive or non-invasive. Invasive tests require a full or partial dismantling of the machine, thereby designating them to the off-line category. For instance, the installation of a search coil sensor inside the air gap of an electric machine would be an invasive test as the air gap is usually not available without disassembling the machine core. A non-invasive test example is the attachment of an accelerometer to the bearing housing of the electric machine. This instrument would measure vibration patterns without requirement for internal machine access.

Maintenance tests for salient-pole generators involve a variety of procedures, including the inspection of armature current, shaft voltage, bearing vibrations and temperature readings, all which help detect potential issues early [4]. Further, magnetic flux readings in the air gap can indicate faults such as rotor winding shorted turns and rotor eccentricity. Regular physical inspections can

identify signs of physical damage, corrosion and aging in the stator, rotor and bearings. More advanced techniques such as partial discharge tests and insulation resistance and polarization index measurements can provide an in-depth analysis of the salient-pole machines' health, specifically the insulation system [3].

2.4 Essential theory and tools for electromagnetic stray field analysis

Up to now, this chapter has covered a wide range of concepts central to the theory of electric generator and electromagnetism. However, some crucial principles are still missing in the terms of model building and magnetic field analysis, to complete the explanation necessary to understand the next chapter. These principles are the focus of the subsequent sections.

2.4.1 The stray magnetic field

The stray magnetic field in an electric generator can be decomposed into a radial and an axial component [9], as shown in figure 2.13. The axial component is a consequence of end current effects, while the radial component is induced by the air gap magnetic field [10]. To investigate the main faults and machine health it is therefore sufficient to analyze only the radial component of the stray magnetic field.

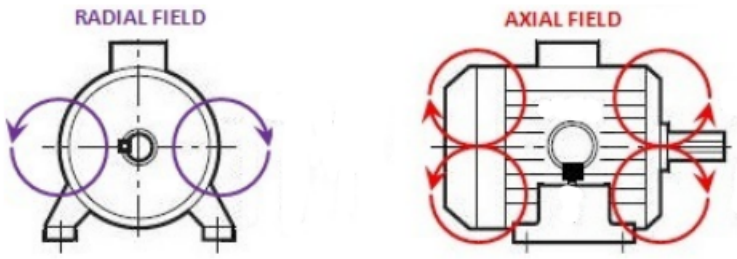

Figure 2.13: The radial and axial stray magnetic field-components in an electric generator. Illustration from [10].

It has in previous sections been argued that because the reluctance of air is so much larger than the reluctance of a ferromagnetic material, that is $\mathcal{R}_{air} \gg \mathcal{R}_{fm}$, all flux flows in the core of an electric machine and not in the air surrounding it. This is a valid simplification for some scenarios, but in the real world there is always some flux flowing outside of the machine's stator frame. This flux is from here on named the external magnetic field or the stray magnetic field. It is visualized in figure 2.14a. This field is many times weaker than the magnetic field in the core of the machine, due to attenuation in the stator yoke [10].

From the air gap magnetic field to the stray magnetic field there are three main causes for attenuation of the field. These three are the stator yoke, the external frame and the air outside the stator. Among them, given a reference point close to the stator frame, the attenuation due to the stator yoke is by far the strongest [9]. If the reference point moves further from the external

frame, attenuation due to air reluctance also increases. To give a number on the attenuation from the air gap magnetic field to the stray magnetic field, an attenuation factor K was calculated in the project task preceding this Master's thesis [2]. A reference point was assumed just outside the stator frame. The attenuation factor was calculated for the generator used as an example also through this thesis, described in section 3.2, and found to be approximately $K \approx 5 \cdot 10^{-5}$. That means that the stray field was expected to be smaller than the air gap magnetic field by a factor of 10^{-5} T, which was confirmed by the simulation results.

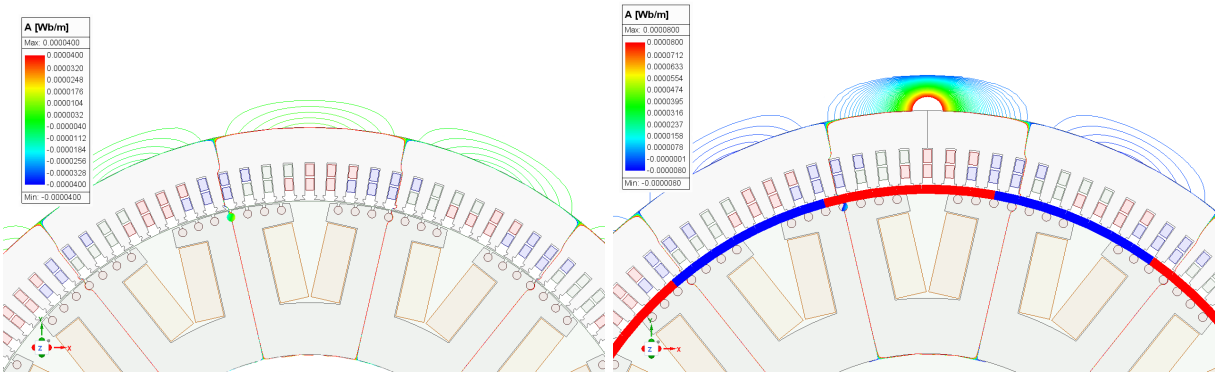

(a) Field lines from the stray magnetic field in a synchronous generator without field-joints.

(b) Field lines from the stray magnetic field in a synchronous generator with field-joints. The air gap colors can be disregarded.

Figure 2.14: Illustration of the stray magnetic field in a salient-pole synchronous generator **(a)** without field-joints and **(b)** with field-joints. It can be observed that the field-joint alters and amplifies the field.

In the presence of a field-joint, the stray flux increases due to the fringing effect. This is visualized in figure 2.14b, where one can clearly see how the magnetic field is a lot stronger in the area around the field-joint than around the neighbouring poles which do not have field-joints.

2.4.2 Maxwell's equations

The set of equations that describe electromagnetic field problems are generally called Maxwell's equations, named after the Scottish scientist James Clerk Maxwell (1831-1879). He was not the one to discover all these relations, but he has been given the credit for unifying them and publishing their related significance. The set consists of four coupled Partial Differential Equations (PDEs) which, together with the Lorentz' force, govern all classical electromagnetic events [37]. The equations describe how charges, currents or electric or magnetic fields, together with the change in these phenomena, affect the rest, and how they propagate and interact with objects. The four equations are called Gauss' law, Ampère's law, Gauss' law for magnetism and Faraday's law of induction. According to problem setup and usefulness, they can be formulated on integral and differential form. In the presentation of Maxwell's equations below, the integral forms are part a) of the equations, and the differential forms are part b).

Gauss' law is presented in equation (2.10). It describes how an electric displacement field $\vec{D}$ behaves in relation to electric charge density ρ_f. In summary, it says that the field components

exiting (or entering) a volume Γ with boundary surface $\partial\Gamma$, equals the number of free charges inside the volume. A practical interpretation of this equation is that electric charges act as sources or sinks to electric fields [37].

Integral form: $$\oiint_{\partial\Gamma} \vec{D} \cdot d\vec{S} = \iiint_{\Gamma} \rho_f dV \tag{2.10a}$$

Differential form: $$\nabla \cdot \vec{D} = \rho_f \tag{2.10b}$$

Gauss' law for magnetism is presented in equation (2.11). It describes how the sum of magnetic field components $\vec{B}$ exiting a closed boundary $\partial\Gamma$ is always 0. This can only be true if there is either no components crossing the boundary at all, or if the number of components exiting the boundary equals the number of components entering the boundary. In practice, Gauss' law for magnetism describes how magnetic fields circulate. This implies that there is no such thing as a magnetic monopole, a magnet must always have a positive and a negative end to have the magnetic field circulate.

Integral form: $$\oiint_{\partial\Gamma} \vec{B} \cdot d\vec{S} = 0 \tag{2.11a}$$

Differential form: $$\nabla \cdot \vec{B} = 0 \tag{2.11b}$$

Faraday's law of induction is presented in equation (2.12). It describes how a time-varying magnetic field $\vec{B}$ relates to an electric field $\vec{E}$. By recalling that the definition of voltage is the difference in electric field strength between two points, $V = \int \vec{E} \cdot d\vec{l}$, it is obvious that a time-varying magnetic field relates to voltage induction and vice versa.

Integral form: $$\oint_{\partial\Sigma} \vec{E} \cdot d\vec{l} = -\frac{d}{dt} \iint_{\Sigma} \vec{B} \cdot d\vec{S} \tag{2.12a}$$

Differential form: $$\nabla \times \vec{E} = -\frac{\partial \vec{B}}{\partial t} \tag{2.12b}$$

Ampère's circuital law is recited in equation (2.13). The second part of both equation (2.13a) and (2.13b) contain free current density $\vec{J}_f$ and the displacement field $\vec{D}$, and are a bit complicated, but they essentially mean current, of the type that flows in a conductor. Therefore, Ampère's law describes how current flowing in a conductor relates to a magnetic field circulating the conductor. The direction of the current compared to the field can be found by the right hand rule.

Integral form:
$$\oint_{\partial\Sigma} \vec{H} \cdot d\vec{l} = \iint_{\Sigma} \vec{J}_f \cdot d\vec{S} + \frac{d}{dt} \iint_{\Sigma} \vec{D} \cdot d\vec{S} \tag{2.13a}$$

Differential form:
$$\nabla \times \vec{H} = \vec{J}_f + \frac{\partial \vec{D}}{\partial t} \tag{2.13b}$$

Finally, the electromagnetic force $\vec{F}$ imposed on electric charges, prompting their movement in space, is called Lorentz force [37]. The expression for Lorentz' force on a current-leading conductor in a uniform magnetic field has already been introduced in equation (2.6), and are therefore not repeated here. As Lorentz force describes the effect of the electromagnetic fields on electric charges, Lorentz force law completes Maxwell's equations when it comes to describing electromagnetic relations. The emf induced in the stator windings of a synchronous generator, due to relative motion between rotor and stator winding, is imposed from Lorentz force [47].

2.4.3 The Finite Element Method (FEM)

Very few of the very simplest electromagnetic problems can be solved analytically. In this case, solving the problem means calculating the electric and magnetic fields, in the areas of interest, at all interesting time points. As explained in the previous section, the equations governing electromagnetic relations are complicated Partial Differential Equations (PDEs). Areas of interest can contain many different materials with non-linear electric, magnetic, thermal and mechanical properties. Geometries may also be complex in shape, which complicates the integral solving. For most cases these problems therefore cannot be solved with analytical methods alone, numerical methods and the use of software are also necessary.

The Finite Element Method (FEM) is a method for numerically solving PDEs in two or three dimensions. The area of interest is discretized into a finite number of smaller elements with simpler geometry, typically of a triangular shape [27]. The PDEs are replaced with algebraic equations with numerical solutions which approximates the true solutions to the PDEs. The algebraic equations are then solved on the simpler, smaller elements instead of on the entire geometry. An error tolerance permits how far the computed solution is allowed to be from the true solution. When the computed solution is estimated to be within the error tolerance, convergence is reached and the problem is deemed solved. In order to get an accurate solution, proper initial values, typically boundary conditions must be known. Figure 2.15b shows a solution for the magnetic field density in a synchronous generator, found with FEM.

Determining the level of discretization across all regions, and consequently the number of triangular elements within the mesh, is a significant factor in ensuring successful application of FEM. A high number of elements yields a FEM solution closer to the true solution, but as more equations are solved, this may also require more time. Fewer elements yield a faster but consequently more inaccurate solution [27]. In fact, high inaccuracy may prevent a solution from being attained at all, due to the it not being within the error tolerance. The mesh density must therefore be

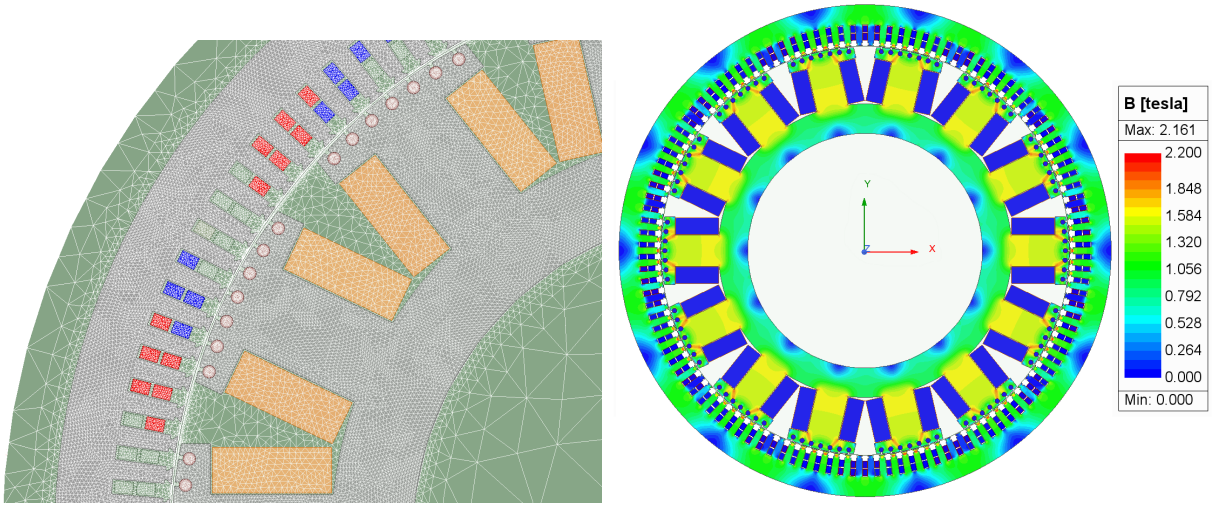

(a) Example of a triangular mesh with varying densities, on which the finite element method can be used to solve Maxwell's equations.

(b) The magnetic flux density distribution for a generator model, solution obtained with the finite element method.

Figure 2.15: Illustration of **(a)** the triangular mesh structure and **(b)** a solution to the magnetic field obtained with the finite element method.

efficiently arranged, taken into account factors such as region geometry and composition, and specific region of interest. For example, in a synchronous generator, the magnetic field in the air gap may be of interest, so the element density should be high here. The stator and rotor yoke, on the other hand, are often simpler and of less interest, and these regions can therefore have a lower element density to save computation time. Figure 2.15a illustrates the variation in the size of triangular FEM elements, for a salient-pole generator. In the air gap, the mesh is so dense that the air gap appears white.

2.4.4 The Fourier transform

The French mathematician Jean-Baptiste Fourier claimed that any signal could be express as a series of sine functions with different amplitudes and frequencies [42]. The Fourier Transform (FT) is therefore called the frequency domain-representation of a signal. Correspondingly, the original signal is called the time domain-representation [38]. The Fourier transform F for the specific frequency c of a time-dependent function $f(t)$ is given in equation (2.14).

$$F(c) = \int_{-\infty}^{\infty} f(t) \cdot e^{-j2\pi ct} dt \tag{2.14}$$

In engineering applications, the power frequency, which in most European networks is 50 Hz, is called the fundamental frequency. The frequency constitutes most of the signal. Other power components are called subharmonics if they have a lower frequency, or simply harmonics if they have a higher frequency [46].

Corresponding to the Fourier transform, a transform that converts a Fourier representation $F(c)$ into its time-domain equivalent $f(t)$ is called the inverse Fourier transform. The inverse Fourier

transform is presented in equation (2.15).

$$f(t) = \int_{-\infty}^{\infty} F(c) \cdot e^{j2\pi ct} dc \tag{2.15}$$

By decomposing an electric signal into a series of its frequencies, the signal can be analyzed in new ways. Fourier analysis plays an important role in a wide variety of applications within electric power engineering [42], such as circuit analysis, digital signal processing, filter design and fault diagnostics in electric machines. For example, the presence, increase or decrease of a specific harmonic could imply a specific type of machine fault [4].

2.4.4.1 The discrete Fourier transform

The Fourier Transform (FT), in the form stated in equation (2.14), converts a time-continuous signal to its frequency-domain representation. Signals that are processed on a computer are digital signals, which are of discrete-time type and not time-continuous [42]. The Fourier transform must therefore be altered to account for finite and discrete signals that can be processed on a computer. This representation of the Fourier transform is called the Discrete Fourier Transform (DFT). Given a discrete sequence $\{x_n\} = x_0, x_1, ..., x_N$ of $(N + 1)$ evenly spaced values, the Fourier representation X_k of that sequence is given by equation (2.16).

$$X_k = \sum_{n=0}^{N-1} x_n \cdot e^{-\frac{j2\pi kn}{N}}, \qquad k = 0, 1, ..., N-1 \tag{2.16}$$

The DFT maintains the same fundamental properties as the FT [15], including linearity, periodicity, conjugate symmetry, and others. The algorithm used for its implementation can substantially influence the computational efficiency. If implemented directly from the definition stated in equation (2.16), the DFT complexity is $O(N^2)$. With certain computational strategies, this complexity can be reduced to $O(N \log(N))$, leading to what is commonly named the Fast Fourier Transform (FFT). For large data sets, the discrepancy in complexity is significant enough to necessitate the use of the FFT, as an algorithm of complexity $O(N^2)$ would require excessive time duration.

2.4.5 Magnetic flux distribution in a salient-pole generator with field-joints

As already introduced in section 2.1.1, the main path of the magnetic flux in an electric generator with salient poles is divided between the poles and the stator. Half of the flux flowing in one salient-pole flows to the left and to the right in the stator, as can be seen on figure 2.16. This implies that there are as many magnetic flux circuits as there are poles, for example fourteen in figure 2.16.

The salient-pole generator in figure 2.16 does not have any field-joints. The field-joints influence the magnetic flux-distribution in the generator [2], as was discovered in the preproject. If both field-joints are healthy and thus have an equal width, the magnetic flux distributes evenly in all the poles, as in figure 2.17a. This figure resembles strongly figure 2.16, which does not have any flux lines at all. If, however, the field-joints have an unequal width, the magnetic flux distributes

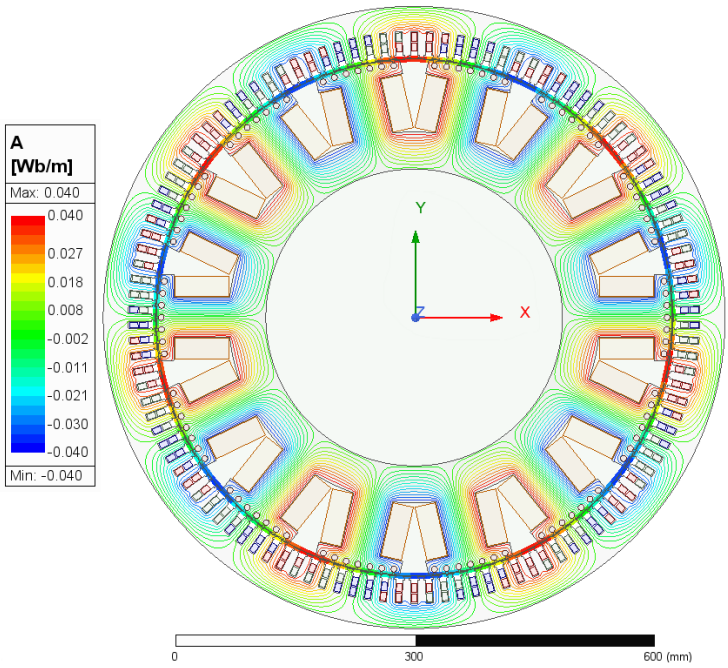

Figure 2.16: Magnetic flux lines in a salient-pole generator without field-joints.

unevenly between the poles, as illustrated in figure 2.17b. In this figure, one field-joint is 0.1 mm wide and the other is 1 mm wide, which means that it is ten times wider than the first. This difference is much larger than what is possible, but the model is included for emphasis: the larger the difference in the field-joint size, the more uneven the distribution of the magnetic flux.

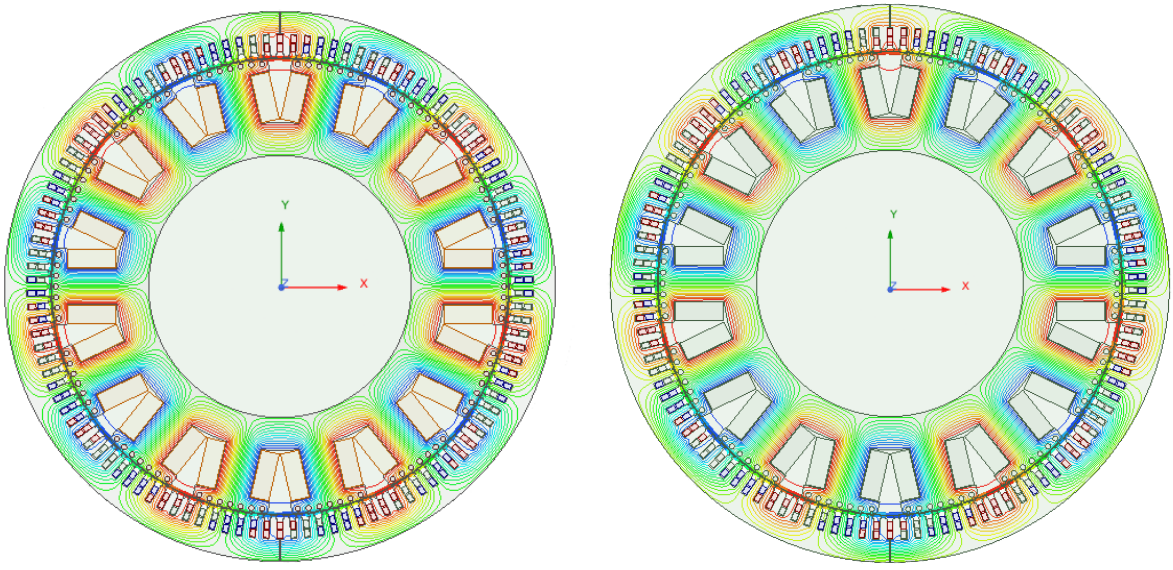

(a) Magnetic flux lines in a generator with healthy field-joints.

(b) Magnetic flux lines in a generator with faulty field-joints.

Figure 2.17: Magnetic flux field lines in two generators with field-joints. The flux distributes evenly between the poles in **(a)** because the field-joints are healthy, and unevenly in **(b)** because the field-joints have an unequal width.

2.5 Fault detection through analysis of the stray magnetic field

The stray magnetic field has already been introduced and defined in section 2.4.1. This section is dedicated to how to find faults through analysis of the stray magnetic field. The direction of the radial stray magnetic field can be seen on figure 2.13. This is the part that stems from the air gap magnetic field, and which therefore contains the relevant information about the machine health. In order to gather this information, sensors of type search coil or Hall effect sensors must be installed. The air gap can be difficult to access and a full or partial dismantling of the machine core may be necessary to be able to install sensors inside the air gap. This renders on-line machine testing impossible and necessitates long inoperative periods. To work around the disadvantages of invasiveness, time-consumption and subsequent costs, the sensors can instead be installed outside of the machine's exterior frame. An example can be seen on figure 2.18b, where a homemade search coil was installed on the stator backside of a synchronous generator [4].

(a) A simple search coil: a copper wire wound around an air core. Illustration from [43].

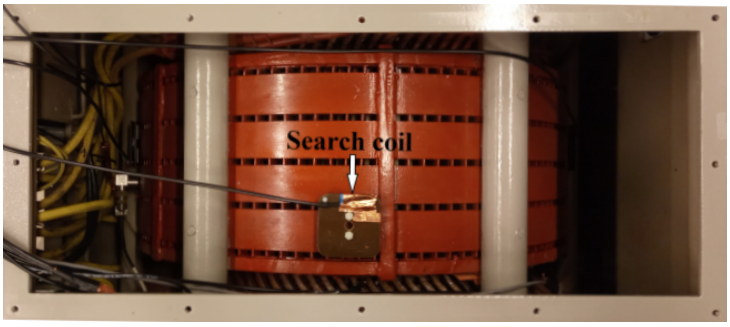

(b) Search coil for measuring stray flux, installed on the outside of the exterior frame of a salient-pole synchronous generator. Illustration from [4].

Figure 2.18: Illustration of **(a)** a simple search coil and **(b)** a search coil installed on the outside of the frame of a synchronous generator.

A search coil is a passive sensor which in the simplest way can be made from a copper wire wound around an air core [43]. An illustration of a search coil is presented in figure 2.18a. Its functioning theory is based on Faraday's law of induction, which has already been explained in several sections in this thesis. When a magnetic flux passes perpendicularly through the opening of the wound coil, an emf is induced in the coil. The size of the emf depends on the magnetic flux' variation with time, as of Faraday's law. The search coil can be connected to an oscilloscope or a different type of measurement apparatus. A higher number of turns in the search coil improves the coil's sensitivity [43]. For example, the search coil from [4] in figure 2.18b was wound with 3000 turns.

When the voltage data has been acquired from the oscilloscope through the stray flux sensor, some data analysis and signal processing has to take place in order to give a diagnosis on the machine health. The signal processing can be divided into three categories: time-domain analysis, frequency-domain analysis and time-frequency-domain analysis [4]. The methods attempted in this thesis work are more thoroughly explained in chapter 4: Pattern recognition methods in this

thesis. In the project task, [2], it was found that a field-joint fault does not alter the frequency content of the measured stray flux voltage. The same is known to be true for static eccentricity fault [14]. Therefore, the methods attempted focus on the changes that occur in the time-domain rather than the frequency domain.

The type of fault made visible from the voltage recorded by the stray flux sensors depends on the position of the sensors. It was found from simulation results in the preproject [2] that faulty field-joins were best detected by installing sensors on the side of each field-joint. The amplitude of the voltage was found to be equal on each side of the same field-joint. If two field-joints had the same widths, the voltage amplitudes recorded at their position were also equal. If the widths differed, so did the amplitudes. It was therefore concluded that different voltages could indicate faulty field-joints. Other types of comparisons between the registered sensor voltages were attempted, without leading to a result. It was found that a field-joint fault does not alter the frequency content of the voltage signal.

At least four sensors are required in order to detect a static eccentricity fault. They must be installed approximately 90° apart, and away from beams, field-joints and other potential disturbances. The difference in the RMS voltages in the sensors located 180° apart discloses whether a static eccentricity-fault is present.

A higher number of sensors yield a better picture of the machine health, as more of the stray magnetic field is measured. The stray magnetic field can be measured around the circumference of the stator frame, and along the axial direction. A typical measuring appliance has eight channels and thus eight sensors can be installed at the same time. Some measuring appliances may also have sixteen channels. Measuring equipment is expensive, and not all companies can or wish to buy new types to perform a stray flux test.

2.6 Statistical tools for data analysis

Several statistical tools are employed to analyze the results obtained in this thesis. In this section, the tools are explained, their advantages and disadvantages and the method of calculation.

2.6.1 Standard deviation

The standard deviation of a data set is a measure of how much each data input in the set deviates from the mean value. For a discrete set of N data inputs x, The standard deviation SD is computed as in equation (2.17). Due to the square root, the standard deviation has the same unit as the data values. The value EX is the expected value, calculated here as the average value, as in equation (2.18).

$$SD = \sqrt{\frac{1}{N}\sum_{n=1}^{N}(x_n - EX)^2} \tag{2.17}$$

$$EX = \frac{1}{N}\sum_{n=1}^{N} x_i \tag{2.18}$$

The standard deviation can give an impression of how clustered or dispersed the collected data is. A high standard deviation usually means the data is more dispersed than a low standard deviation. However, bias or a low sample size can also affect the calculated standard deviation [45].

2.6.2 Method of least squares

The method of least squares is a method within regression analysis to approximate the best fit curve in a data set. The curve can be used to approximate solutions not part of the measured data set. It can be a linear curve, or of a higher degree. The coefficients $[\hat{\beta}]$ of the best fit curve are chosen to minimize the error sum of squares SSE, calculated as in equation (2.19). Here, $\hat{y}$ is the best fit curve, for a linear model given as $\hat{y}_i = \hat{\beta}_0 + \hat{\beta}_1 x_i$.

$$SSE = \sum_{n=1}^{N}(y_n - \hat{y}_n)^2 \tag{2.19}$$

The method of least squares is a simple and robust method. A disadvantage is that the computed model can be sensitive to outliers, as an outlier can represent a large addition to the sum SSE, which the method minimizes.

2.6.3 Normalization: Min-max feature scaling

In a data set with data from different scales, a form of normalization may render it possible to compare the data points in the set. The data points are then brought to a common scale. One normalization method is the min-max method, or minimum-maximum feature scaling. Each data point x is then normalized according to equation (2.20), where x_{min} and x_{max} are the minimum and maximum values in the data set.

$$x' = \frac{x - x_{min}}{x_{max} - x_{min}} \tag{2.20}$$

With min-max normalization, all data points are normalized to a value between 0 and 1. The smallest data point gets value 0 and the largest gets value 1. It is a simple method which conserve relative differences in the data. This signifies that the method can be sensitive to outliers, as one major outlier could displace all other values either close to 1 or 0. If more data is gained, a new minimum or maximum value could occur, which means that all data must be normalized again.

Chapter 3

Modelling and simulations

This chapter presents a comprehensive description of the computer models used to represent the two generators which are analyzed. It provides information about the model software, Ansys Electronics, as well as specifics of each generator. This knowledge is put together to explain the construction of the models, with their main limitations. The fault application method is accounted for. An exhaustive description of all models constructed for the purpose of this thesis is provided, along with tabulated summaries for succinct reference.

3.1 Software and procedure

The simulation models were made with the software Ansys Electronics Desktop 2023 R1, which is a platform collection of electronic system design tools. More specifically, the models were made with the simulation solver Ansys Maxwell. This solver uses finite element analysis to solve electromagnetic field problems for objects with complex geometries and properties. It has solvers for static, transient and time-varying fields and the frequency domain. It is especially accommodated to simulate low-frequency electromagnetic devices such as electric machines, transformers and actuators [28].

The main simplification applied to the models was to make them two-dimensional instead of three-dimensional. As explained in the theory chapter in section 2.4.1, the stray magnetic field is composed from the radial magnetic field components. By assuming invariable conditions in the axial direction, which is reasonable for the scopes of this thesis, it is reasonable to only compute the 2D fields. Therefore, the axial air ducts were not included in the models and neither was the lamination stacking factor. The simplification saved a lot of computation time.

Detailed descriptions on how the laboratory generator was modelled can be found in [18], [19], and the reader is referenced there for further information on the basic modelling process. The industrial generator model was made in the same way as the laboratory generator, with different specifications and geometries. The way the laboratory generator differs from the healthy cases in [18], [19], is the addition of stray flux sensors, field-joints and static eccentricity. A thorough explanation of how the sensors were modelled can be found in the preproject, [2].

3.1.1 Modelling the sensors

Each sensor was modelled as two copper circles. In total, 10 sensors were positioned around the stator circumference, as illustrated in figure 3.1, in the same positions as in the preproject [2]. The sensors were assumed 2.5 mm from the stator. Sensor 1 is positioned at 0° and sensor 6 at 180°. There is a 45° difference between sensors 1, 2 and 4, and likewise between sensors 6, 7 and 9. There is a displacement of 5 mechanical degrees° between sensors 3, 4 and 5 and between sensors 8, 9 and 10.

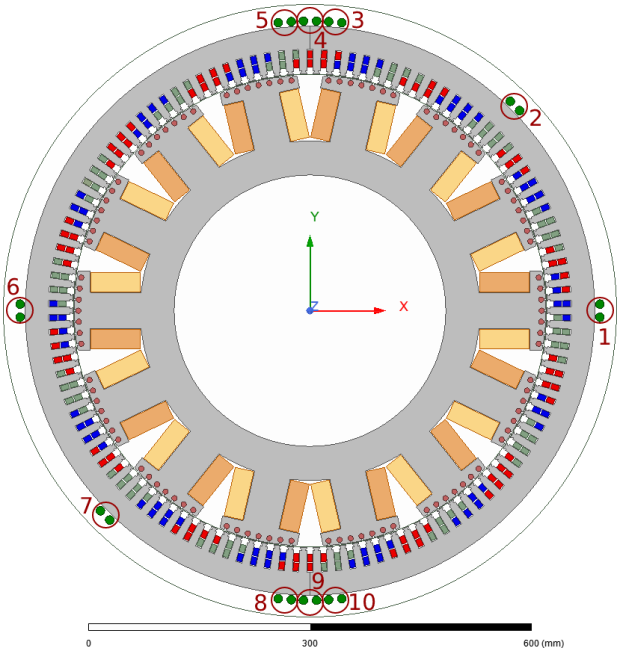

Figure 3.1: Illustration of the positioning and naming of the 10 sensors positioned around the laboratory generator circumference. Illustration from [2].

3.1.2 Modelling the field-joints

The field-joints were modelled as shown in figure 3.2. They were modelled in the same way as in the preproject [2], simply by constructing air gaps in the correct locations. No insulation materials were added in these simulations.

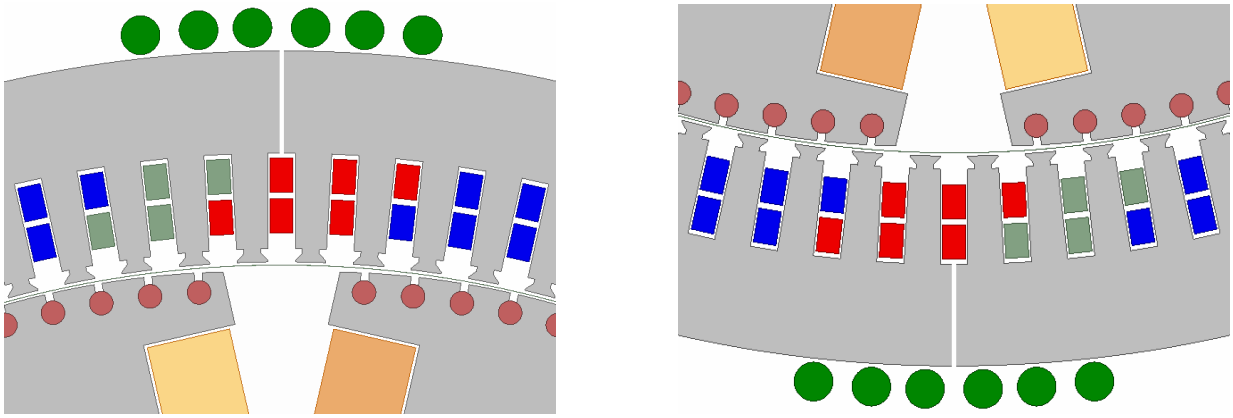

(a) Field-joint at the top of the stator.

(b) Field-joint at the bottom of the stator.

Figure 3.2: Two stator field-joints, enlarged for better visual effect. The field-joints are located in the middle of a stator slot. Illustration from [2].

3.1.3 Modelling static eccentricity

Static eccentricity was modelled by using the function "Move" on the stator objects in Ansys Electronics. The stator objects include the stator core, the stator winding objects and the sensor objects. If the rotor objects had been moved instead of the stator objects, dynamic eccentricity would have been modelled instead [18]. The objects can be moved in a x- and y-direction. To apply static eccentricity in other directions, the x- and y-movement was calculated with trigonometric identities and the Pythagorean theorem, and rounded to a 6-digit precision.

3.2 The laboratory generator

The laboratory generator is a 100 kVa 14 pole synchronous generator with salient poles, located at NTNU in Trondheim. Its nameplate data is presented in table 3.1. The nominal length of the air gap is 1.75 mm. The laboratory generator is specially designed to be able to emulate different faults typically related to synchronous generators. It can therefore be altered to produce static eccentricity fault, dynamic eccentricity fault, inter-turn short-circuits and damper bar failure.

Table 3.1: Nameplate data for the laboratory generator.

Description	Value	Unit	Symbol
Nominal power	100	kVa	P_n
Nominal line voltage	400	V	V_L
Frequency	50	Hz	c
Synchronous speed	428	rpm	n_s
Nominal no-load current	53.2	A	I_0
Nominal load current	103	A	I_n

The geometric scopes of the laboratory generator are listed in table 3.2.

Table 3.2: Additional data for the laboratory generator.

Description	Value	Unit	Symbol
External rotor radius	323.25	mm	$R_{r,ext}$
Internal stator radius	325	mm	$R_{s,int}$
External stator radius	390	mm	$R_{s,ext}$
Pole pairs	7	#	p
Turns per pole	35	#	
Stator slots	114	#	

As can be seen from table 3.2, the laboratory generator has 14 poles and 114 stator slots. As a three-phase machine, the number of slots per pole and phase is 2.71. The laboratory generator therefore has a fractional slot winding [16]. The greatest common factor between the number of slots and number of poles is 2. The laboratory generator should therefore have two magnetic symmetries, and the magnetic flux density distribution should repeat itself twice around the circumference of the generator [44]. However, finite element analysis demonstrated that the number of magnetic symmetries is in fact 7, corresponding to [16] and the number of pole pairs.

3.2.1 The laboratory generator models

Several projects have previously described in detail the construction of the model for the laboratory generator. To repeat these explanations have been determined unnecessary, as the same models were used to create the models in this Master's project. If the reader is curious, they are therefore referenced to these theses for a thorough explanation of the model construction [18], [19].

3.2.1.1 Models with field-joint fault

During the project task in [2], models of the laboratory generator with field-joints were simulated. Because the models made for this Master's thesis are strongly related and a development of that project, the project task models are presented in this section. The results are summarized in subsection 4.1 of chapter 5: Pattern recognition results on simulated models. Five models with different variations of field-joints, in addition to one model without any field-joints, were simulated in [2]. All models with field-joints had a total number of two field-joints, one at the top and one at the bottom of the generator. Their position is visualized in figure 2.3. A healthy field-joint in the laboratory generator was estimated to have a width of 1 mm. A faulty field-joint could be either tighter or looser by 0.1 mm. In addition, two models with larger field-joints were made, to verify that the field-joints had any effect on the stray field-flux at all. The field-joint models are summarized in table 3.3.

Table 3.3: Overview of the laboratory generator models with field-joints simulated in [2].

Name	**Description**	**Width top** [mm]	**Width bottom** [mm]
No field-joints	No field-joints	-	-
Symmetric	Two healthy field-joints	0.2	0.2
Asymmetric tight	One healthy and one smaller field-joint	0.2	0.1
Asymmetric loose	One healthy and one larger field-joint	0.2	0.3
Symmetric large	Two large field-joints	1	1
Asymmetric large	One large and one healthy field-joint	1	0.1

3.2.1.2 Models with static eccentricity

There were made 11 different laboratory generator models with different degrees of static eccentricity. These are presented in table 3.4. Because a main advantage to fault detection through the stray magnetic field is early detection of the fault, most models have a low degree of eccentricity. If the eccentricity severity is more than 50 %, the vibrations related to the eccentricity would be so large that stray flux measurements would be unnecessary [23]. Therefore, one model has a severity of 50 %, and no models have a higher severity than that. It can be noted that the model named "No SE" without any eccentricity is the same as the model named "No field-joints" in table 3.3.

The naming of the different models needs some explanation. The first two letters "SE" refers to Static Eccentricity. Then follows a number, which is the severity of the static eccentricity in percent. Next follows one or two more letters, which represent a direction of the static eccentricity. The letters can be "E", "N", "W" and "S" and they represent the four cardinal directions: east, north, west and south. On a protractor, north would represent 90°, west would represent 180°and so on. A combination of two letters would represent a mix of two directions, e.g. "SW" would represent South-West. If the direction of SE is exactly on a cardinal direction or exactly between two cardinal directions, no more numbers follow. If the direction of the SE is not exactly on or between one or two cardinal directions, the name ends with the degrees given as "00deg". Note that "SE" as the first two letters of the name means Static Eccentricity, while if it is not the first two letters it is a direction, meaning South-East. Then, for example model SE40NE would have a severity of 40 % in the direction north-east, which is 45°.

Table 3.4: Overview of the laboratory generator models with Static Eccentricity (SE).

Name	**Severity** [%]	**Angle** [degrees°]
No SE	0	-
SE10E	10	0
SE20NE	20	45
SE40NE	40	45
SE20N	20	90
SE20NW	20	135
SE20W	20	180
SE30W	30	180
SE40W	40	180
SE15SW245deg	15	245
SE50SE290deg	50	290

3.2.1.3 Models with combined static eccentricity and field-joint fault

There were made 6 different laboratory generator models with both field-joints and a static eccentricity fault. These are presented in table 3.5.

Table 3.5: Overview of the laboratory generator models with Static Eccentricity (SE) and field-joints. "Width top" refers to the field-joint width at the top of the generator, and "Width bottom" to the width of the bottom field-joint.

Name	**Severity** [%]	**Angle** [degrees°]	**Width top** [mm]	**Width bottom** [mm]
SE20N ASYM TIGHT	20	90	0.1	0.2
SE20W SYM	20	180	0.2	0.2
SE20W ASYM TIGHT	20	180	0.2	0.1
SE20W ASYM LOOSE	20	180	0.2	0.3
SE40SE355deg SYM	40	355	0.2	0.2
SE40SE355deg ASYM LOOSE	40	355	0.2	0.3

3.3 The industrial generator

The industrial generator model is based on a generator located at a power plant in Norway. Due to security protocols, the power plant must be anonymous. The name of the generator can thus not be disclosed and it is therefore named the industrial generator in this thesis. The nameplate data for the generator on which the industrial generator model is built is presented in table 3.6. Some supplementary data on geometry and structure is presented in table 3.7.

Table 3.6: Nameplate data for the industrial generator.

Description	Value	Unit	Symbol
Nominal power			P_n
Nominal line voltage			V_L
Frequency	50	Hz	c
Synchronous speed	375	rpm	n_s
Nominal no-load current	500	A	I_0
Nominal load current	103	A	I_n

Table 3.7: Additional data for the industrial generator.

Description	Value	Unit	Symbol
Internal rotor radius	1205	mm	$R_{r,ext}$
External rotor radius	1756	mm	$R_{s,int}$
Internal stator radius	1800	mm	$R_{s,ext}$
Pole pairs	8	#	p
Turns per pole	51	#	
Stator slots	192	#	
Parallel paths	2	#	
Turns per slot per path	3	#	

The industrial generator has 16 poles and 192 stator slots. The number of slots per pole and phase is therefore given as 4, which means that the generator has an integer phase winding [16]. The number of poles and phases are factors of the number of slots, which renders it possible to have eight magnetic symmetries. The magnetic flux density distribution in the air gap, and thus in the stray magnetic field, should therefore repeat itself eight times around the circumference of the industrial generator.

3.3.1 The industrial generator models

The model of the industrial generator, as depicted in figure 3.3, was constructed utilizing analogous strategies and software as for the laboratory generator model. As with the laboratory generator model, the healthy industrial generator model was made for a previous project and directly employed in this Master's work. It had been utilized a sufficient amount of times that any inaccuracies of notable size are presumed to have already been identified.

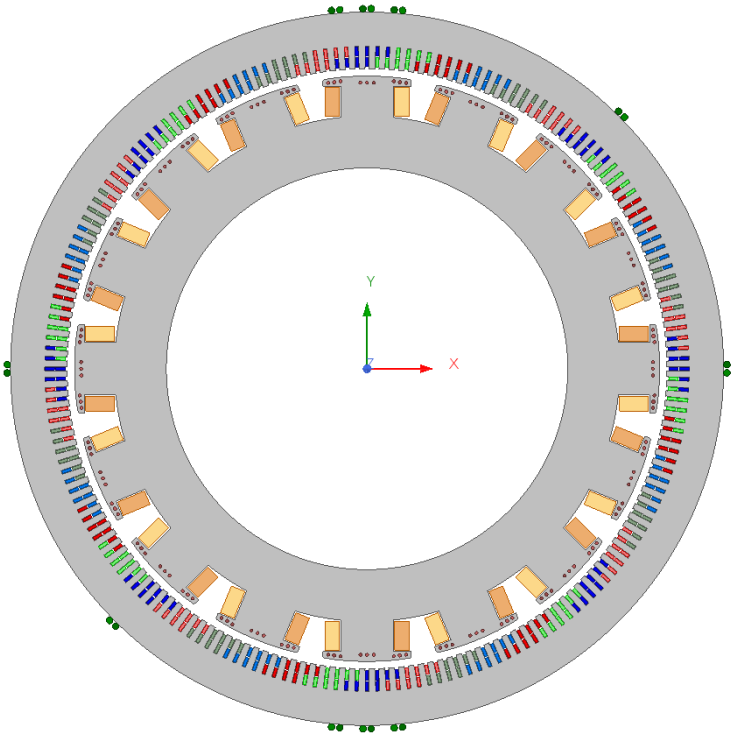

Figure 3.3: Illustration of the industrial generator model. Ten stray flux sensors are modelled around the circumference of the stator backside, in the same positions as for the laboratory generator in figure 3.1.

There were made six different models of the industrial generator. One healthy model without any static eccentricity, and five faulty models with varying static eccentricity. None of the models have field-joints. The models are presented in table 3.8. The naming of the models follows the standard presented in subsection 3.2.1.2, with the prefix "IG" to separate these models from the laboratory generator models.

Table 3.8: Overview of the Industrial Generator (IG) models with Static Eccentricity (SE).

Name	**Severity** [%]	**Angle** [degrees°]
IG Healthy	0	-
IG SE40NE	40	45
IG SE20W	20	180
IG SE30W	30	180
IG SE40W	40	180
IG SE15SW245deg	15	245

Chapter 4

Pattern recognition methods

This chapter outlines the five methodologies developed for the identification of field-joint faults and static eccentricity faults in a synchronous generator. The first method is unmodified from the preproject. Additionally, two empirical testing procedures are introduced, and two analytical approaches are proposed to quantify the severity and position of a static eccentricity fault. The development of these methods largely stems from an empirical process, characterized by iteration and refinement. The methods are based on the assumption that four stray flux sensors are available.

4.1 Method I: Voltage comparison for field-joint fault identification

This is a method proposed to identify field-joint fault. It is carried over from the preproject [2].

During the Master preproject task, simulations of models with various types of field-joints and field-joint faults were carried out. It was discovered that the best way to identify a field-joint fault, was to measure the induced stray flux voltage on each side of each field-joint and compare the amplitudes. The voltages on each side of a field-joint should be equal in both shape and amplitude. Equal voltages at two different field-joints indicate that the field-joints are of equal widths, and thus healthy. If the voltages differ, on the other hand, the field-joints have different widths and are faulty. The largest amplitude is measured at the largest field-joint, due to the increased fringing flux. Likewise, the smallest amplitude is measured at the smallest field-joint.

Five models with different variations of field-joints, and one model without any field-joints, were simulated in the project task, [2]. One of the models was a healthy case, with what was considered healthy field-joints. Three models had one healthy field-joint and one field-joint of a different size, which was considered faulty. One model had two equal, but unrealistically large, field-joints, as a type of method test case. Common for all models was that the field-joint was considered to have constant width in the axial direction. This implied that only 2D models needed be considered. No 3D models or eventual impacts of 3D space were considered.

4.2 Method II: General voltage comparisons

This method is proposed to investigate the behaviour of static eccentricity and of static eccentricity combined with field-joint fault, in the stray magnetic field.

Information is stored in the behaviour and appearance of the voltages induced in the stray flux sensors. In the preproject, simulations demonstrated that a difference between cases with healthy and faulty field-joints was a change in voltage amplitude and shape [2], and the RMS values. A similar approach of comparing voltages and voltage attributes is also employed in the work for the Master's thesis. Comparisons can be made both between voltages in different sensors of the same generator or generator model, and between sensors located at the same position for different generators or generator models. Visual inspection of the plotted voltages could then reveal potential patterns.

4.3 Method III: Space vectors

This is a second method proposed to investigate the behaviour of static eccentricity and of static eccentricity combined with field-joint fault, in the stray magnetic field.

A potential interesting discovery was whether the recorded stray flux voltages would display any pattern or trend when converted to space vectors. In this context, a space vector is the conversion of time-dependent stray flux sensor voltages to a 2D-space canvas. The x- and y-coordinates of one space vector are the voltage values from two different sensors, recorded at the same time instant. The objective of this method was to discover whether the space vector revealed a pattern when it was plotted for all time instances t.

Different space vectors were constructed, in order to investigate possible relations between the sensor measurements. Four stray flux sensors were employed to construct the vectors, located 90° apart around the stator external frame. The sensor voltage measurements are hereby named v_1, v_2, v_3 and v_4. The subscript numbers of each Space Vector (SV) explains which sensors it is constructed from: The first subscript number refers to the sensor utilized in the x-coordinate, and the second subscript number refers to the sensor in the y-coordinate. The different space vectors that were investigated are listed as equation (4.1).

$$SV_{1,2} = [v_1(t), v_2(t)] \tag{4.1a}$$

$$SV_{3,4} = [v_3(t), v_4(t)] \tag{4.1b}$$

$$SV_{1,3} = [v_1(t), v_3(t)] \tag{4.1c}$$

$$SV_{2,4} = [v_2(t), v_4(t)] \tag{4.1d}$$

$$SV_{13,24} = SV_{12} + SV_{34} = [v_1(t) + v_3(t), v_2(t) + v_4(t)] \tag{4.1e}$$

$$SV_{12,34} = SV_{13} + SV_{24} = [v_1(t) + v_2(t), v_3(t) + v_4(t)] \tag{4.1f}$$

4.4 Method IV: Three approaches to compute static eccentricity severity

The objective of this method, extending to all three approaches, is to compute the severity of a static eccentricity fault.

A simple and straight-forward method was employed in the attempt to determine the severity of a Static Eccentricity (SE) fault. The method involves the subtraction of the sensor voltages measured 180° apart, which then were normalized to a common scale. Because of accuracy uncertainty, two measures of scale were tested. This resulted in two approaches which are quite similar but vary in the type of normalization value utilized. The two approaches are presented in the two subsequent subsections. Following these two approaches is one more approach which is a development of Approach 1 and Approach 2. It is named Approach 3 and presented in the last subsection.

4.4.1 Approach 1

In order to determine the SE severity fault, voltage measurements from four stray flux sensors must be available. The sensors should be located around the stator external frame 90 mech° apart, or at least with 180° mechanical between two and two sensors. The RMS values of the voltages must be computed. The RMS voltages from the four sensors are hereby named V_1, V_2, V_3 and V_4. It is assumed that the sensor location for V_1 and V_3 is 180 mech° apart, and likewise that the sensor location for V_2 and V_4 is 180 mech° apart.

In Approach 1, the normalization value is the total average of all four RMS values, computed as in equation (4.2).

$$\bar{V} = \frac{V_1 + V_2 + V_3 + V_4}{4} \tag{4.2}$$

The idea behind both Approach 1 and Approach 2 is that the static eccentricity fault affects the stray flux induced voltages and thus their RMS values. A sensor close to the smaller part of the air gap is induced with a higher RMS voltage due to the decreased magnetic reluctance. A sensor close to the larger part, on the other hand, is induced with a smaller RMS voltage due to increased magnetic reluctance. The smaller or larger the air gap, and thus the lower or higher severity, the larger variation in RMS voltage is measured. The severity is computed separately on the x-axis and y-axis as presented in equation (4.3).

$$V_x = 100\% \cdot \frac{V_1 - V_3}{\bar{V}} \tag{4.3a}$$

$$V_y = 100\% \cdot \frac{V_2 - V_4}{\bar{V}} \tag{4.3b}$$

Finally the total severity SEV is calculated as the sum of the absolute values of V_x and V_y, as in equation (4.4).

$$SEV = abs\{V_x\} + abs\{V_y\} \tag{4.4}$$

4.4.2 Approach 2

The approach to determine the SE severity utilized in Approach 2 is very similar to that utilized in Approach 2. As already stated, the only difference is the normalization value used to bring V_x and V_y to a common scale. In Approach 2, one normalization value is computed for V_x and one for V_y. The values are the averages for each sensor direction, respectively. This means that the normalization values are computed according to equation (4.5), and the severities in the x- and y-direction are then computed according to equation (4.6).

$$\bar{V_x} = \frac{V_1 + V_3}{2} \tag{4.5a}$$

$$\bar{V_y} = \frac{V_2 + V_4}{2} \tag{4.5b}$$

$$V_x = 100\% \cdot \frac{V_1 - V_3}{\bar{V_x}} \tag{4.6a}$$

$$V_y = 100\% \cdot \frac{V_2 - V_4}{\bar{V_y}} \tag{4.6b}$$

The total severity SEV is finally computed in the same way as in Approach 2, with equation (4.4).

4.4.3 Approach 3

Approach 3 is a development of both Approach 2 and Approach 2. All methods are algorithms for determining the severity of a static eccentricity. The variation to this last method from the first two is very subtle. The only difference is that in the last step, instead of computing the severity SEV as in equation (4.4), it is computed as the square root of the sum of V_x squared and V_y squared, as in equation (4.7). Other than the change in this last step, Approach 3 follows the same procedure as Approach 2 and Approach 2.

$$SEV = \sqrt{V_x^2 + V_y^2} \tag{4.7}$$

How V_x and V_y are calculated depends on whether Approach 2 or Approach 2 are used as basis for the process. It therefore exists in two variations.

4.5 Method V: Time-Series Data Mining

This technique is proposed with the objective of computing the angular position of a static eccentricity fault.

Time-Series Data Mining (TSDM) is a method used to reveal patterns in time series data [39]. The term "data mining" refers to a cluster of methods used to identify trends in large sets of data [41]. In TSDM, data mining techniques are accommodated to time series data. The method was employed with good results in [39], [40], and has been adapted for the purpose of stray flux analysis for this thesis.

This paragraph explains some of the terms used in the next paragraphs during the explanation of the TSDM method. The terms may be well-known to readers familiar with dynamical systems theory, but as they are crucial in order to understand the method, a review (or introduction) follows. Firstly, a first difference-series is a series of subtractions of y-data corresponding to linear x-data. First differences is used for pattern recognition to determine order of dependence. For example, if the first difference is constant for all instances, the dependence is linear. Secondly, a phase-space, or state-space, is a multidimensional space where all possible conditions, or states, of a system are represented. Thirdly, vector embedding is a technique often used in natural language processing in order to measure semantic similarity in data sets. The vector can e.g. be time-series sensor data.

The first step in order to employ TSDM on the stray flux data is to create a series of first differences from the data: $\Delta L = L(n) - L(n-1)$, where $n = 1, 2, 3, ..., N$ is the time index. Then, a 2D phase space is created with time-series embedding from ΔL. Two series, ΔL_x and ΔL_y, are created from the time-series data; one series for the abscissa and one for the ordinate of a coordinate system. The series ΔL_x is a delayed version of ΔL_y, that is $\Delta L_x(n) = \Delta L_y(n - l)$, where l is the lag.

The constructed phase-space is a topological interpretation of the states of a system. In order to differentiate between different phase-spaces, and thus differentiate healthy systems from faulty system, the Radius of Gyration (RoG) of phase-space points is used. The radius of gyration is a computed physical distance to a point with the same moment of inertia as the total mass would have if it was concentrated there. The mass distribution is the phase-space point distribution, where each point is assigned a unit mass. The formula to calculate the radius of gyration r is given in equation (4.8), where l is the lag and N is the number of points in the first-difference vector. Further, the vector $m^2(n)$ is computed as in equation (4.9). It is given as the distance from the nth phase space point to the center of mass τ. To create a more pragmatic picture, m is the hypotenuse in a right triangle where the two catheti are the distances from the first difference at time instant n to the center of mass in their respective dimensions.

$$r = \sqrt{\frac{\sum_{n=1+l}^{N} m^2(n)}{N - l}} \tag{4.8}$$

$$m^2(n) = (\Delta L(n) - \tau_0)^2 + (\Delta L(n-l) - \tau_l)^2 \tag{4.9}$$

The center of mass is computed for two dimensions: a dimension with zero time lag and a dimension with time lag l. The formulas for how they were computed are listed respectively in equation (4.10a) and (4.10b).

$$\tau_0 = \frac{\sum_{n=1}^{N-l} \Delta L(n)}{N-l} \tag{4.10a}$$

$$\tau_l = \frac{\sum_{n=1+l}^{N} \Delta L(n)}{N-l} \tag{4.10b}$$

The end outcome from performing the TSDM and then computing the radius of gyration, results in one number for each data set, i.e. the radius of gyration. In the case of stray flux sensor data, the approach is used on each set of sensor data, for each model simulated (or, in the case of real measurements, on each sensor measurement taken). The radii of gyration are then compared, both to the computed radii from the other sensors in the same simulation, or to radii computed from the same sensor in different simulations.

4.5.1 Compute the angle of a static eccentricity fault

A method for estimating the angular position of static eccentricity in an electric generator by means of time-series data mining and radius of gyration, is explained in this section. During static eccentricity, the air gap is smaller on one side of the stator than the other, and the smallest point is exactly 180° from the largest. A visualization is provided in figure 2.12b. The varying air gap length increases the magnetic reluctance on the large air gap side and decreases it on the small air gap side. This results in a stronger magnetic flux on the small air gap side than on the large side. Higher voltages are therefore induced in the stray flux sensors mounted on the small air gap side compared to the large side. From equation (4.9), one can observe that if two series $m_1^2(n)$ and $m_2^2(n)$ are computed from two first difference-series $\Delta L_1(n)$ and $\Delta L_2(n)$, then $m_2(n) > m_1(n)$ if $\Delta L_2(n) > \Delta L_1(n)$ and n is unchanged for the two series. Consequently, the radius of gyration is larger close to the static eccentricity angle compared to far from it.

A minimum of four stray flux sensors are required to compute the static eccentricity angle. The four sensors should be installed with 90° mechanical between them if possible, or at least with 180° mechanical between two and two sensors. Two nearby sensors installed (approximately) 90° apart now represent one quadrant of the stray flux. Based on the reasoning in the previous paragraph, the angular position of the static eccentricity is in the quadrant belonging the two sensors with the largest computed RoG. The four quadrants can be named $QI, QII, QIII$ and QIV, as shown in figure 4.1. In a healthy generator, without static eccentricity, no quadrant is identified, since the computed RoGs are approximately equal for all sensors.

A more specific static eccentricity angle can be computed when the quadrant is identified. The four sensors are hereby named S_1, S_2, S_3 and S_4, and their positions are as in figure 4.1. If, for

example, the two largest computed radii of gyration are computed for the sensors S_1 and S_2, the static eccentricity angle is located in QI. The angle is determined by computing a normalized share of a 90° angle for both the largest and second largest radius of gyration, and then choosing the correct option of these two as the angle. The shares are named α and β, and the equations to compute them are presented in equations (4.11a) and (4.11b). Here, r_a is the largest radius of gyration, r_b is the second largest radius of gyration and $\bar{r}$ is the average radius of gyration, computed from all four gyration radii. From the equations, one understand that $\alpha + \beta = 90°$, and $\alpha \geq \beta$ because $r_a \geq r_b$. However, to which sensors r_a and r_b correspond must still be identified.

$$\alpha = 90° \cdot \frac{r_a - \bar{r}}{(r_a - \bar{r}) + (r_b - \bar{r})} \tag{4.11a}$$

$$\beta = 90° \cdot \frac{r_b - \bar{r}}{(r_b - \bar{r}) + (r_a - \bar{r})} \tag{4.11b}$$

Whether α or β is the correct angle for the static eccentricity position, depends on the sensor position for r_a and r_b. In figure 4.1a, r_a corresponds to sensor S_1 and r_b to sensor S_2. This is because the static eccentricity angle is closest to S_1, and thus the largest radius of gyration is computed at this sensor. The correct angle is therefore β, the smaller of the two computed angles. If the static eccentricity angle was instead closest to sensor S_2, as in figure 4.1b, then r_a would be computed at sensor S_2, and α is the correct choice for the computed static eccentricity angle.

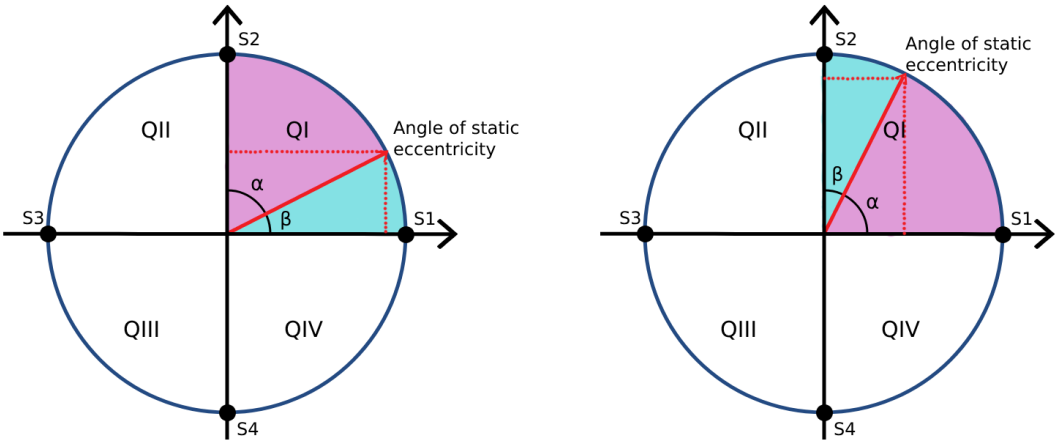

(a) If the SE position is closest to sensor S_1, then the angle share β is the SE angle.

(b) If the SE position is closest to sensor S_2, then α is the correct angle share.

Figure 4.1: A visualization of the idea behind the method to compute the Static Eccentricity (SE) angle. The two largest Radius of Gyration (RoG) are computed for the sensors at the quadrant of the SE, here S_1 and S_2. α and β, where $\alpha \geq \beta$, is the share of a 90° angle each RoG represents.

Together, α and β constitute a 90° angle, as shown in figure 4.1. If the angle of the static eccentricity belongs to a different quadrant than QI, the correct angle share is simply added to the beginning angle of the correct quadrant. With beginning angle is meant the first degree inside the quadrant. For example, the beginning angle of QII is 90° and of QIV is 270°. Then, if quadrant QIV is identified as the SE quadrant, and an angle share of 27° is computed, the final computed angular position of the static eccentricity is $270° + 27° = 297°$.

Chapter 5

Pattern recognition results on simulated models

This chapter provides the main findings derived from the application of the pattern recognition methods described in chapter 4: Pattern recognition methods, applied to simulation models. The simulation models were introduced in chapter 3: Modelling and simulations. The chapter sections follow the same order as in chapter 4. The first section repeats the results discovered in the preproject task. The second and third sections present the plotted results from two empirical methods, in the search for patterns in the stray flux sensor voltages. Section 5.4 presents the computed static eccentricity severities while section 5.5 presents the computed static eccentricity angles.

5.1 Results Method I: Voltage comparison for field-joint fault identification

The results presented in this section are all repeated from the project task in [2]. There are two reasons why they are also presented here in this Master's thesis. The first is that the work conducted for the thesis is an extension of the work conducted in the preproject. The second is that experimental field tests were carried out as part of this thesis work, with the intention of verifying the preproject results. The results are presented only for the laboratory generator, as the industrial generator was not investigated during this time. The results are presented for the models listed in table 3.3. They are presented for the sensor numbers 3 & 5 and 8 & 10, following the sensor naming in figure 3.1. These are the sensors located on each side of each field-joint.

It can be observed on figures 5.1 and 5.2, the models without field-joints and with healthy, symmetric field-joints, how the voltage amplitudes are equal. It can also be observed on figures 5.3 and 5.4, the models with faulty field-joints, how the amplitudes are larger on sensors at the field-joint with the larger width.

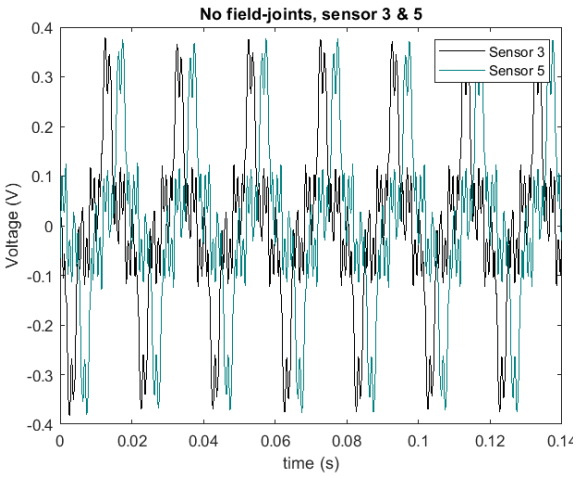

(a) Induced voltage in sensor 3 & 5.

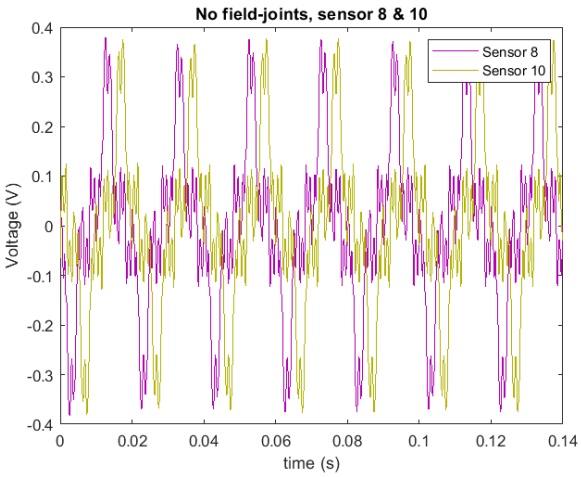

(b) Induced voltage in sensor 8 & 10.

Figure 5.1: Induced sensor voltages for the laboratory generator model without field-joints. Results from the preproject [2].

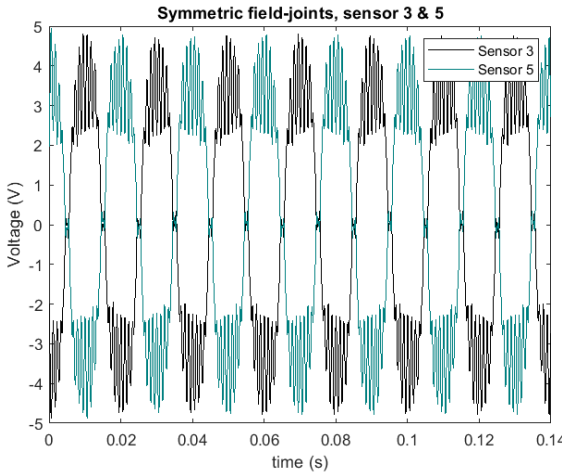

(a) Induced voltage in sensor 3 & 5.

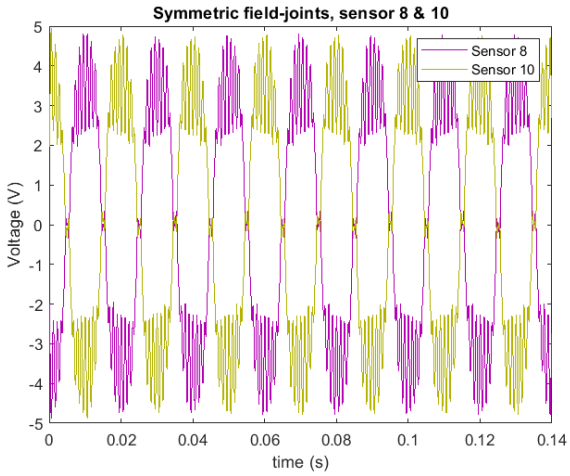

(b) Induced voltage in sensor 8 & 10.

Figure 5.2: Induced sensor voltages for the laboratory generator model with two symmetric, healthy field-joints, both of width 0.2 mm. Results from the preproject [2].

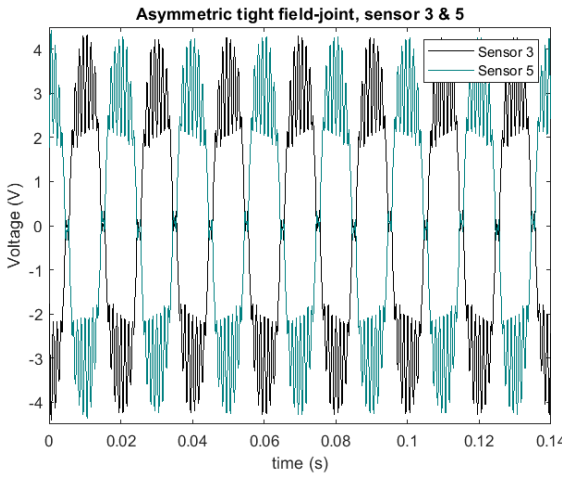

(a) Induced voltage in sensor 3 & 5.

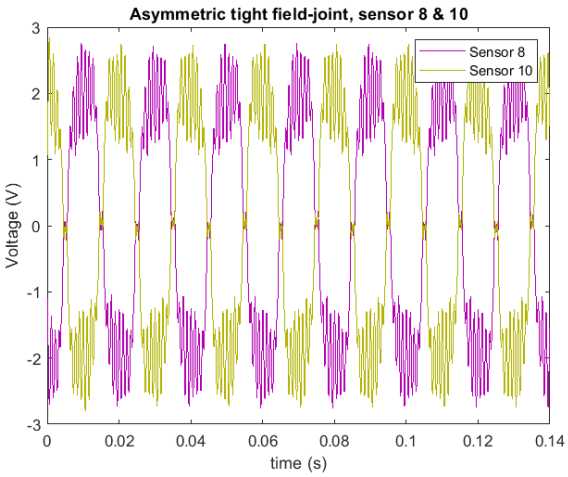

(b) Induced voltage in sensor 8 & 10.

Figure 5.3: Induced sensor voltages for the laboratory generator model with one healthy field-joint of 0.2 mm, located at sensors 3 & 5, and one faulty field-joint of 0.1 mm, located at sensors 8 & 10. Results from the preproject [2].

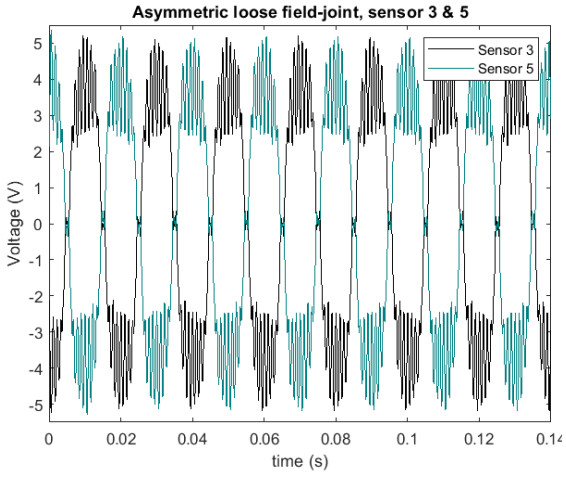

(a) Induced voltage in sensor 3 & 5.

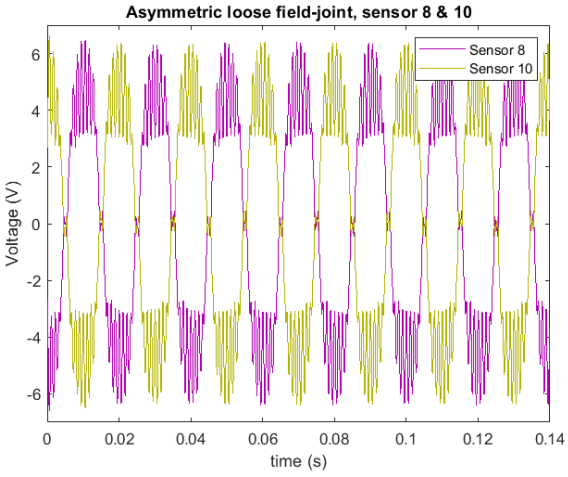

(b) Induced voltage in sensor 8 & 10.

Figure 5.4: Induced sensor voltages for the laboratory generator model with one healthy field-joint of 0.2 mm located at sensors 3 & 5, and one faulty field-joint of 0.3 mm, located at sensors 8 & 10. Results from the preproject [2].

Table 5.1 summarizes the RMS values of the sensor voltages plotted in figures 5.1 through 5.4. It can be observed that the RMS values are approximately equal for the sensors on each side of one field-joint. It can also be observed that the RMS values are approximately equal for the models with no field-joints or symmetric field-joints, and that they differ in the models with asymmetric field-joints.

Table 5.1: Simulated RMS voltages for the stray flux sensors on each side the Field-Joints (FJ). The model naming is explained in table 3.3.

Model name	**Sensor 3** [V]	**Sensor 5** [V]	**Sensor 8** [V]	**Sensor 10** [V]
No FJ	0.169	0.169	0.169	0.169
Symmetric FJ	2.937	2.939	2.939	2.937
Asym tight FJ	2.628	2.629	1.728	1.728
Asym loose FJ	3.190	3.191	3.902	3.901

5.2 Results Method II: General voltage comparisons

In this section the results from pattern recognition Method II are presented. Method II is a general method where the stray flux sensor voltages are compared in order to find patterns which can be used to determine static eccentricity and field-joint fault. In this result chapter, only the voltage plots are presented, from an assortment of models with only static eccentricity fault and a combination of both static eccentricity and field-joint fault. The first subsection contains the laboratory generator models, while the second subsection contains the industrial generator models. The position of the sensors according to their name is presented in figure 3.1. The plots with the same color represent sensors at the same position on the stator circumference.

5.2.1 Laboratory generator models

In this subsection, the results are presented for the laboratory generator models. The stray flux sensor voltages are presented two and two together, in total eight sensors distributed on four plots. The positioning of the sensors is presented in figure 3.1. The first result, in figure 5.5, contains the result from the laboratory generator model without field-joints and without static eccentricity. This figure is generated from the preproject. It is included to simplify the comparison with new models.

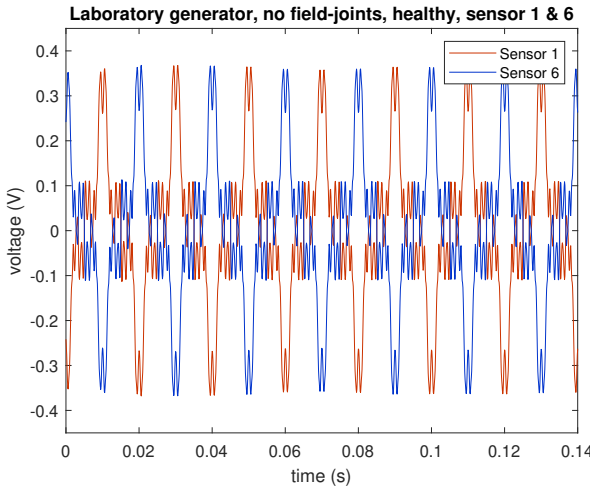

(a) Laboratory generator, no field-joints, no static eccentricity, sensor 1 & 6.

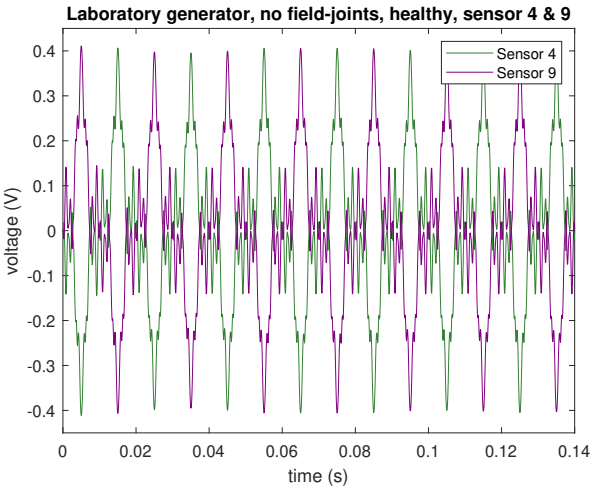

(b) Laboratory generator, no field-joints, no static eccentricity, sensor 4 & 9.

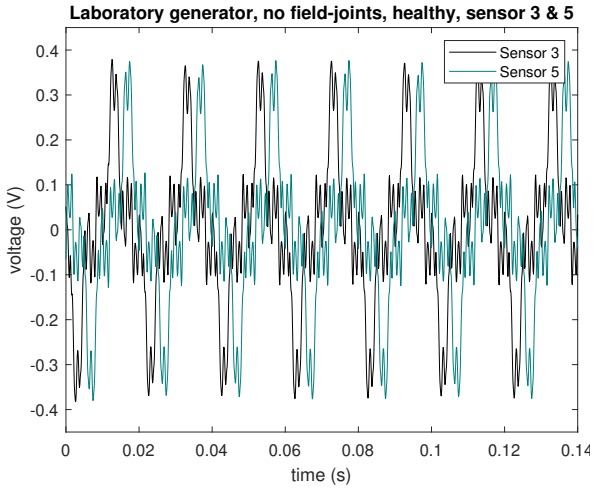

(c) Laboratory generator, no field-joints, no static eccentricity, sensor 3 & 5.

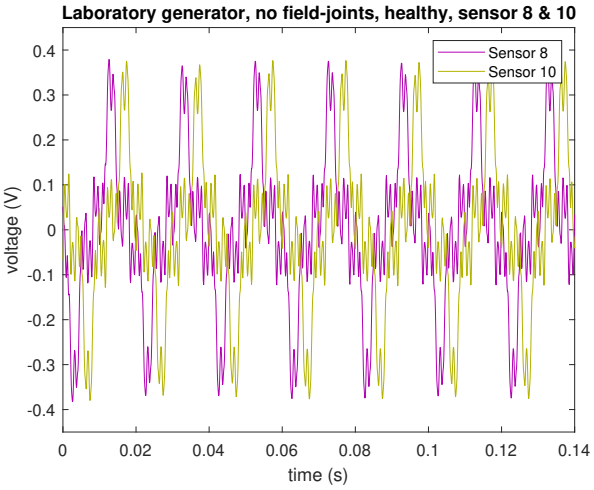

(d) Laboratory generator, no field-joints, no static eccentricity, sensor 8 & 10.

Figure 5.5: Stray flux sensor voltages for one mechanical rotation of the laboratory generator model with no field-joints and no static eccentricity.

Figure 5.6 and figure 5.7 present the laboratory generator models without field-joints and with respectively 20 % and 40 % static eccentricity at 45°.

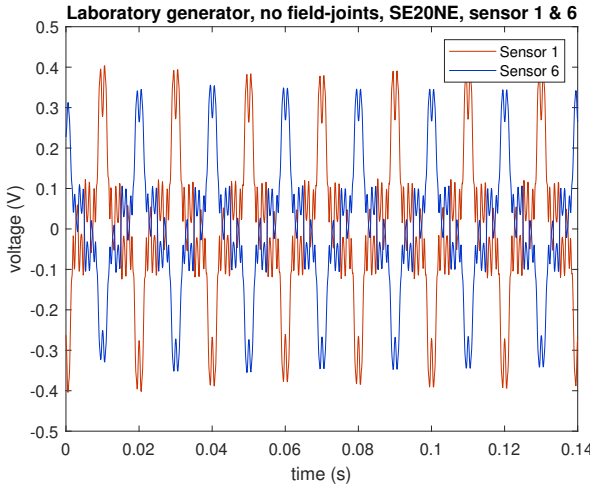

(a) Laboratory generator, no field-joints, 20 % static eccentricity at 45°, sensor 1 & 6.

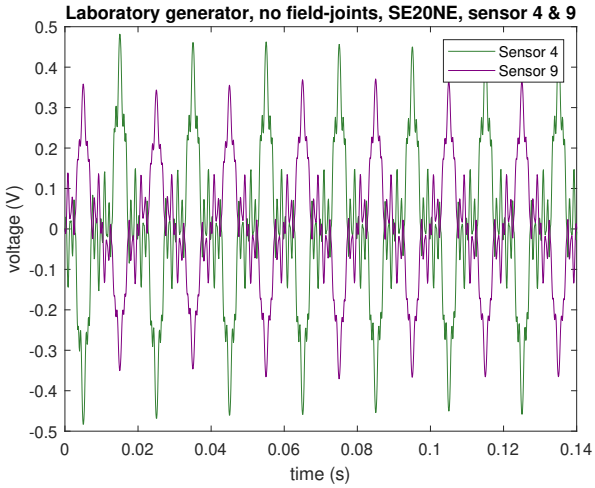

(b) Laboratory generator, no field-joints, 20 % static eccentricity at 45°, sensor 4 & 9.

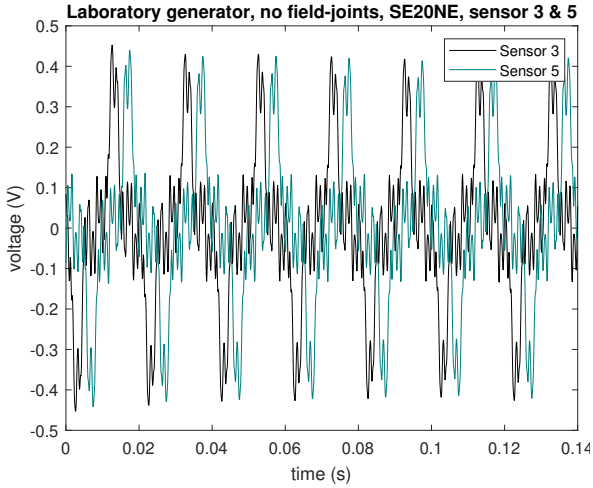

(c) Laboratory generator, no field-joints, 20 % static eccentricity at 45°, sensor 3 & 5.

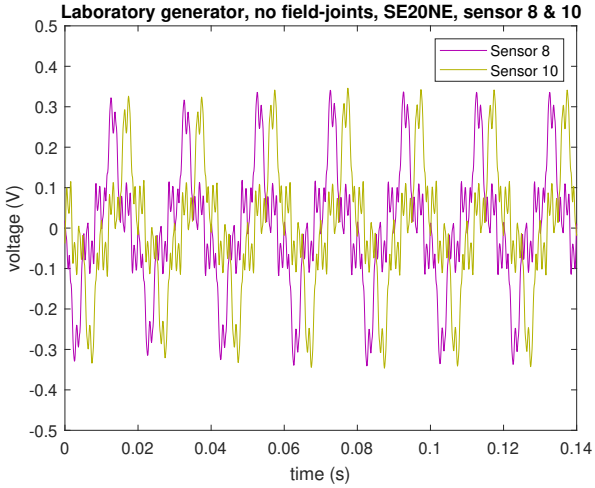

(d) Laboratory generator, no field-joints, 20 % static eccentricity at 45°, sensor 8 & 10.

Figure 5.6: Stray flux sensor voltages for one mechanical rotation of the laboratory generator model with no field-joints and 20 % static eccentricity at 45°.

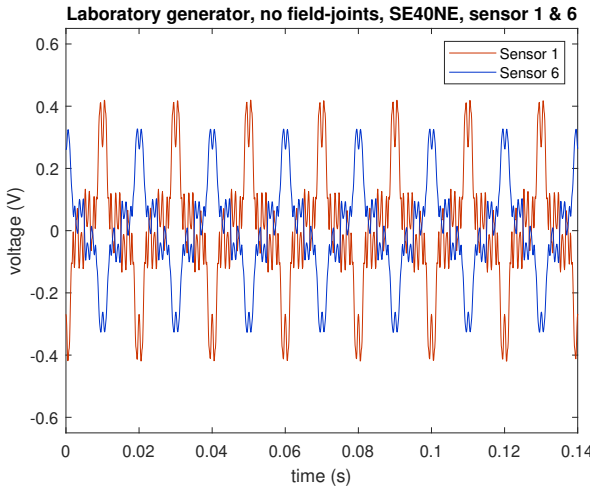

(a) Laboratory generator, no field-joints, 40 % static eccentricity at 45°, sensor 1 & 6.

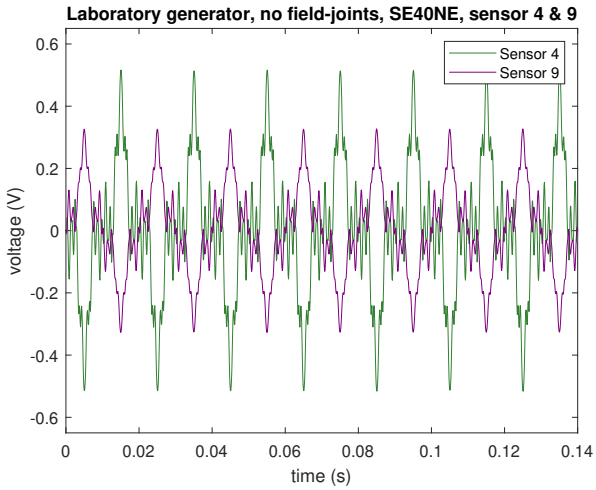

(b) Laboratory generator, no field-joints, 40 % static eccentricity at 45°, sensor 4 & 9.

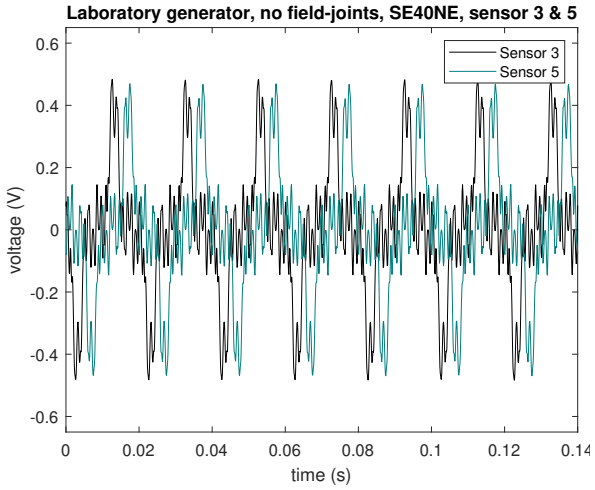

(c) Laboratory generator, no field-joints, 40 % static eccentricity at 45°, sensor 3 & 5.

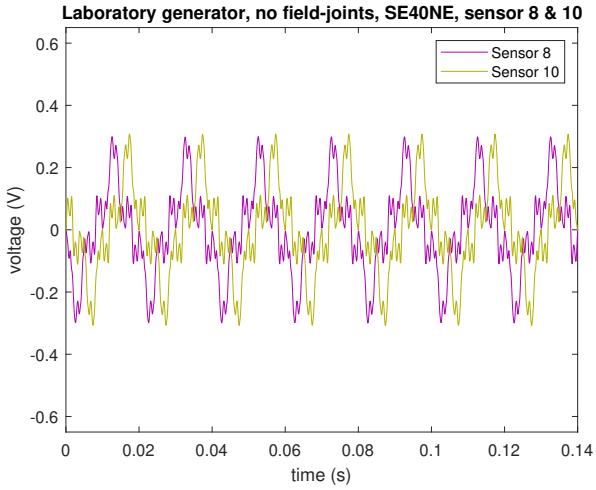

(d) Laboratory generator, no field-joints, 40 % static eccentricity at 45°, sensor 8 & 10.

Figure 5.7: Stray flux sensor voltages for one mechanical rotation of the laboratory generator model with no field-joints and 40 % static eccentricity at 45°.

The following three figures represent three results with 20 % static eccentricity at 180° and varying field-joint situations. The first, figure 5.8, has no field-joints. The second, figure 5.9, has symmetric field-joints. The third, figure 5.10, has one healthy field-joint at the top and one tighter field-joints at the bottom, so-called asymmetric tight field-joints.

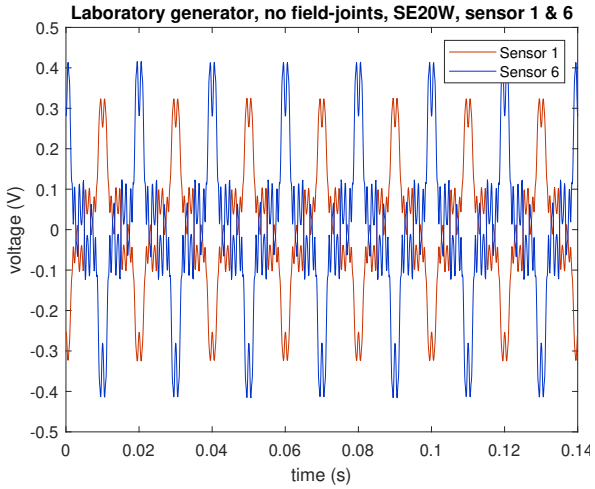

(a) Laboratory generator, no field-joints, 20 % static eccentricity at 180°, sensor 1 & 6.

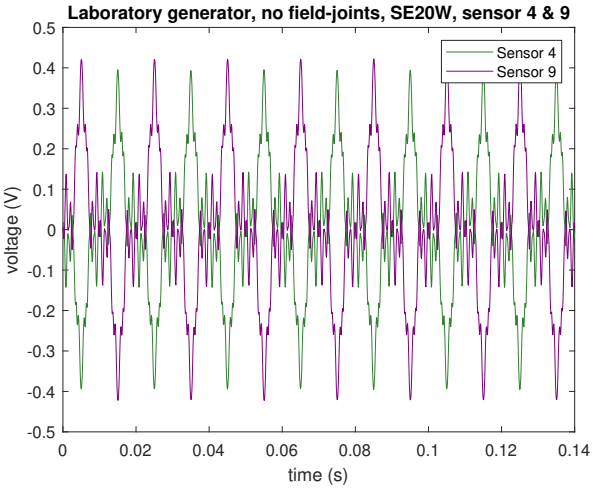

(b) Laboratory generator, no field-joints, 20 % static eccentricity at 180°, sensor 4 & 9.

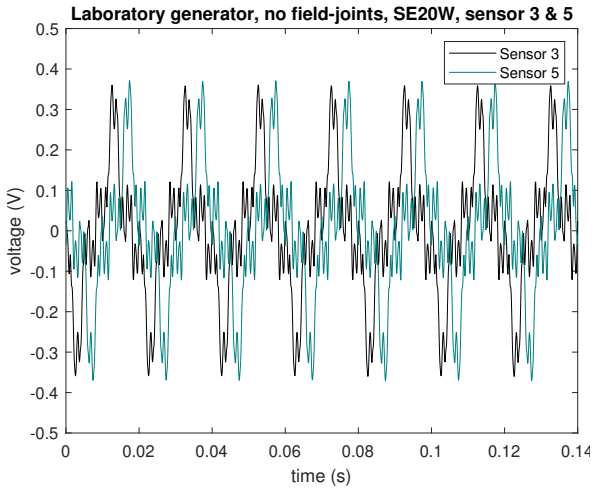

(c) Laboratory generator, no field-joints, 20 % static eccentricity at 180°, sensor 3 & 5.

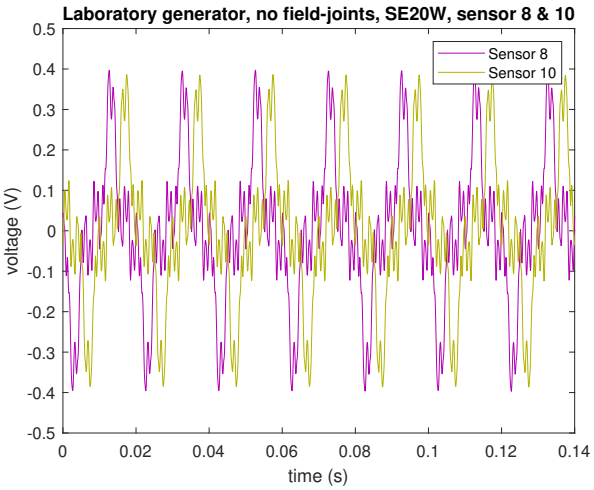

(d) Laboratory generator, no field-joints, 20 % static eccentricity at 180°, sensor 8 & 10.

Figure 5.8: Stray flux sensor voltages for one mechanical rotation of the laboratory generator model with no field-joints and 20 % static eccentricity at 180°.

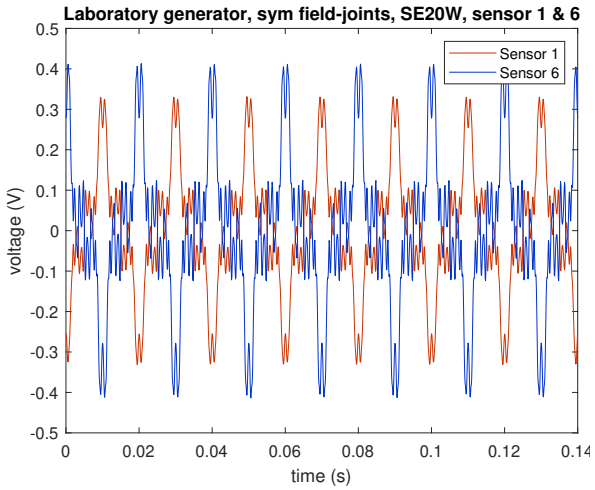

(a) Laboratory generator, symmetric field-joints, 20 % static eccentricity at 180°, sensor 1 & 6.

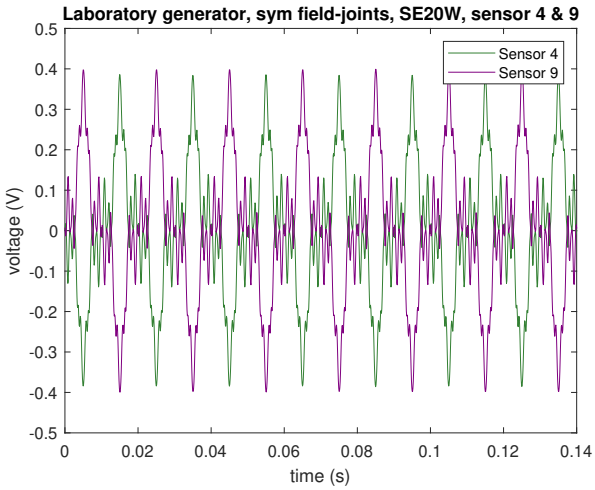

(b) Laboratory generator, symmetric field-joints, 20 % static eccentricity at 180°, sensor 4 & 9.

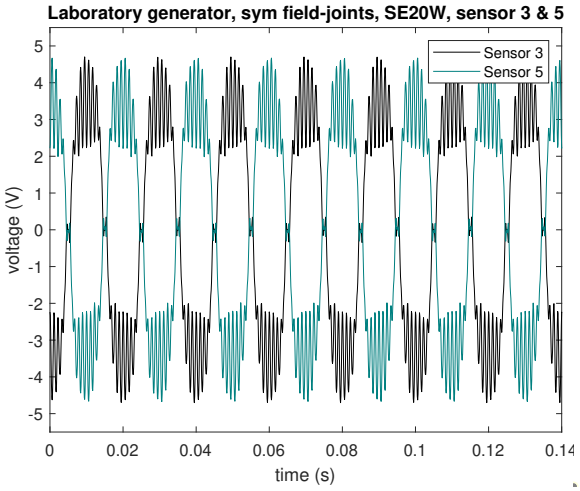

(c) Laboratory generator, symmetric field-joints, 20 % static eccentricity at 180°, sensor 3 & 5.

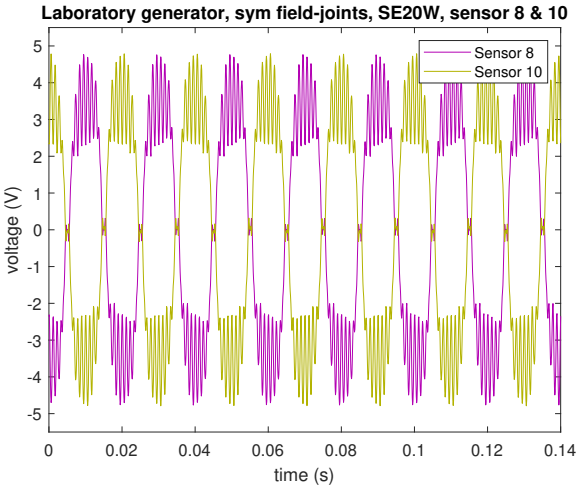

(d) Laboratory generator, symmetric field-joints, 20 % static eccentricity at 180°, sensor 8 & 10.

Figure 5.9: Stray flux sensor voltages for one mechanical rotation of the laboratory generator model with symmetric field-joints and 20 % static eccentricity at 180°.

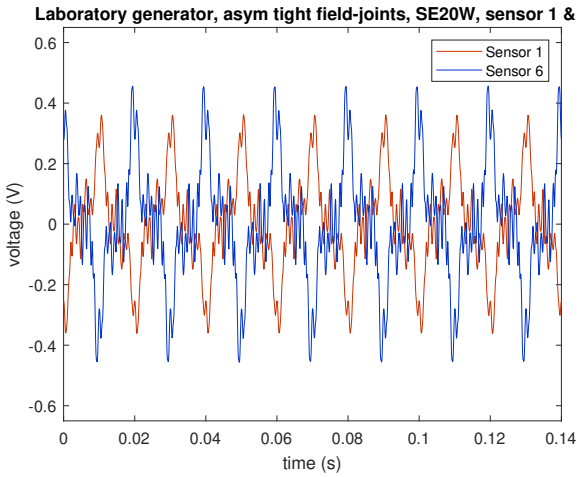

(a) Laboratory generator, asymmetric tight field-joints, 20 % static eccentricity at 180°, sensor 1 & 6.

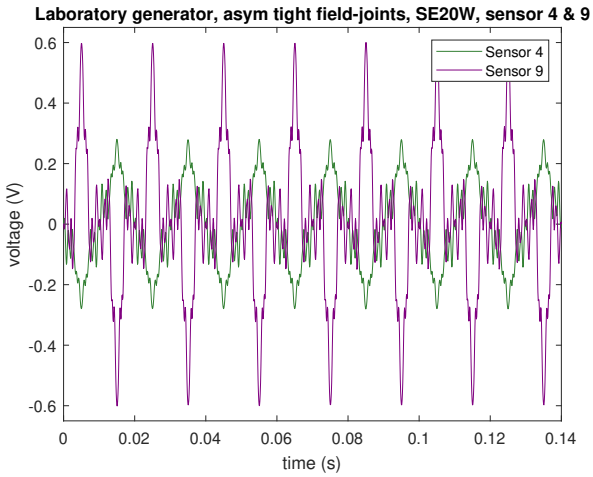

(b) Laboratory generator, asymmetric tight field-joints, 20 % static eccentricity at 180°, sensor 4 & 9.

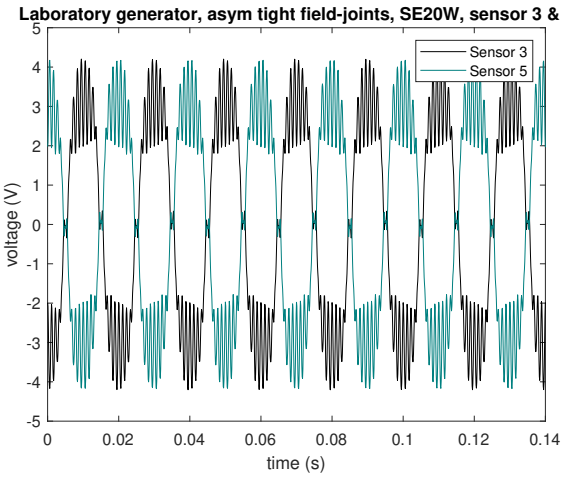

(c) Laboratory generator, asymmetric tight field-joints, 20 % static eccentricity at 180°, sensor 3 & 5.

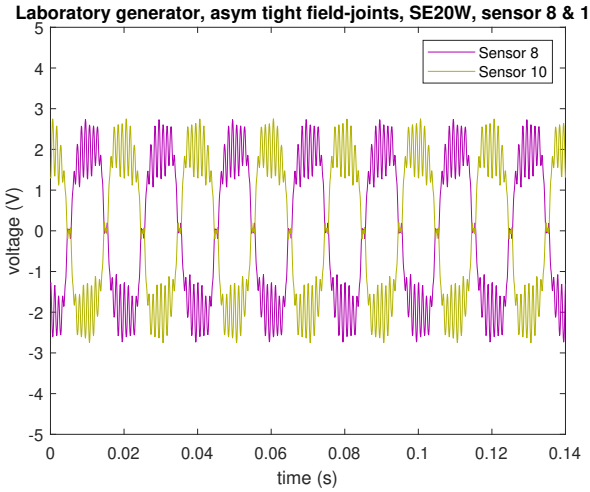

(d) Laboratory generator, asymmetric tight field-joints, 20 % static eccentricity at 180°, sensor 4 & 9.

Figure 5.10: Stray flux sensor voltages for one mechanical rotation of the laboratory generator model with asymmetric tight field-joints and 20 % static eccentricity at 180°.

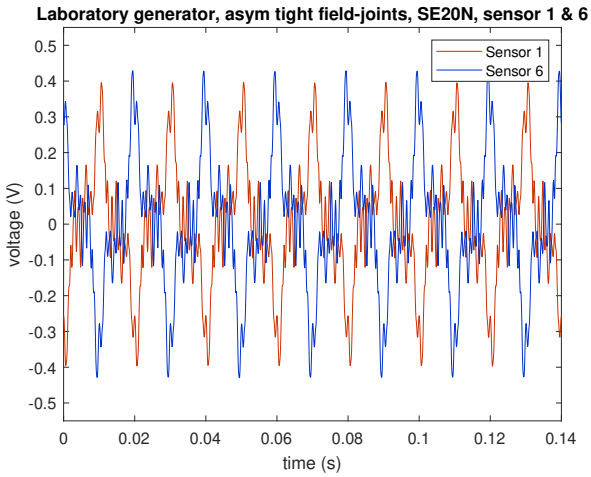

(a) Laboratory generator, asymmetric tight field-joints, 20 % static eccentricity at 90°, sensor 1 & 6.

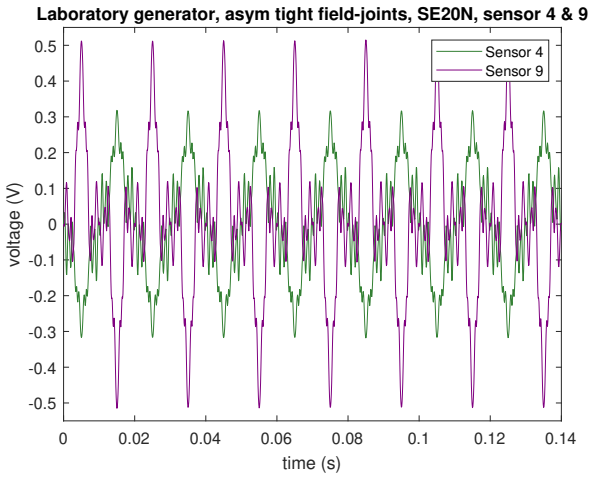

(b) Laboratory generator, asymmetric tight field-joints, 20 % static eccentricity at 90°, sensor 4 & 9.

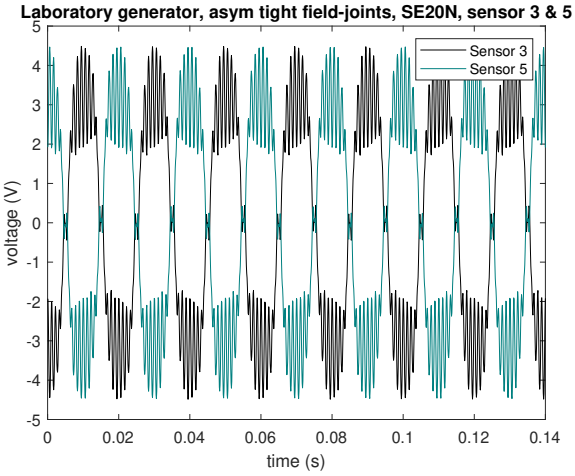

(c) Laboratory generator, asymmetric tight field-joints, 20 % static eccentricity at 90°, sensor 3 & 5.

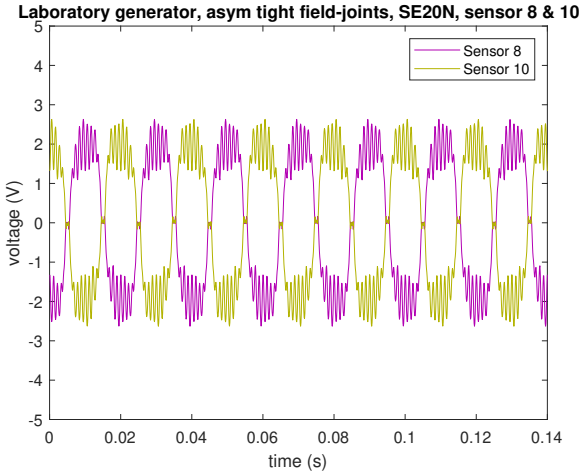

(d) Laboratory generator, asymmetric tight field-joints, 20 % static eccentricity at 90°, sensor 8 & 10.

Figure 5.11: Stray flux sensor voltages for one mechanical rotation of the laboratory generator model with asymmetric tight field-joints and 20 % static eccentricity at 90°.

5.2.2 The industrial generator models

In this subsection, the stray flux sensor voltage plots from the industrial generator simulations are presented. The naming, coloring and sensor positioning follow the same standard as for the laboratory generator. Because none of the industrial generator models has field-joints, the voltages from sensor 3 & 5 and 8 & 10 are not included. The voltages for sensor 1 & 6 and 4 & 9 are still presented in pairs, as with the laboratory generator. With the industrial generator however, due to the number of poles, number of slots and the winding, the voltage plots are in phase. The plots from sensor 6 and sensor 9 are therefore phase shifted with 180° electrical, in order to display all voltages in a better manner.

The first result, in figure 5.12, presents a healthy case with no static eccentricity.

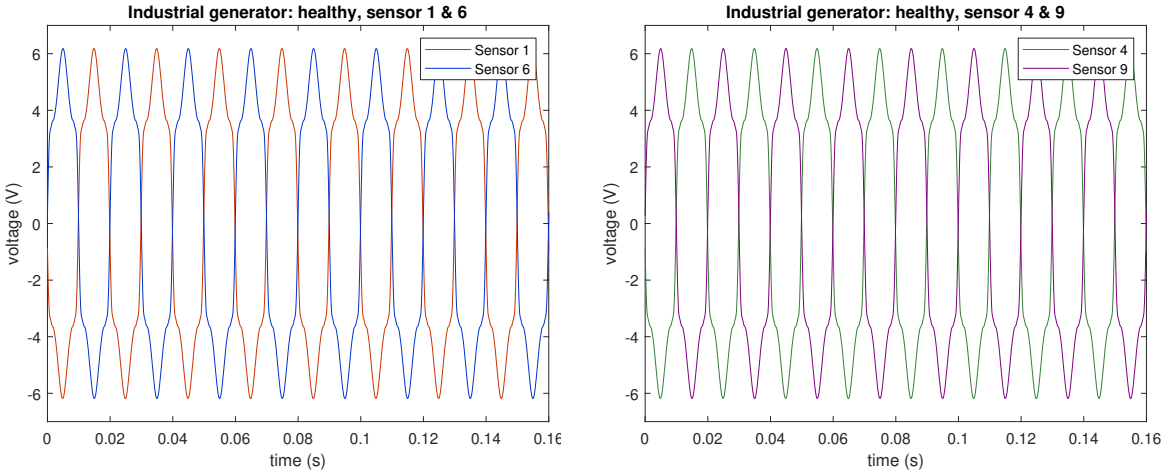

(a) Industrial generator model, no field-joints, no static eccentricity, sensor 1 & 6.

(b) Industrial generator model, no field-joints, no static eccentricity, sensor 4 & 9.

Figure 5.12: Stray flux sensor voltages for one mechanical rotation of the industrial generator model without static eccentricity.

The following two figures present the stray flux sensor voltage plots for the models with 20 % and 40 % static eccentricity at 180°. They are respectively figure 5.13 and figure 5.14.

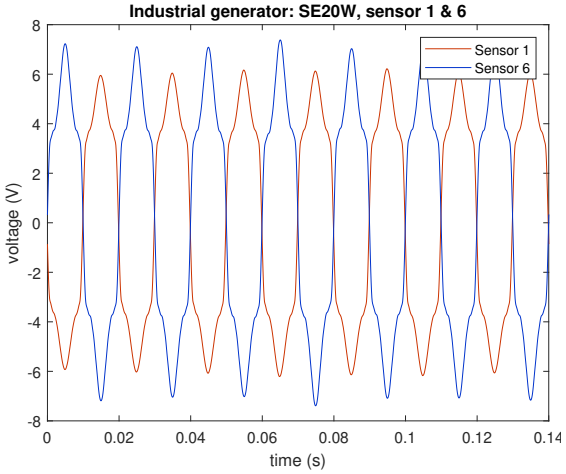

(a) Industrial generator model, no field-joints, 20 % static eccentricity at 180°, sensor 1 & 6.

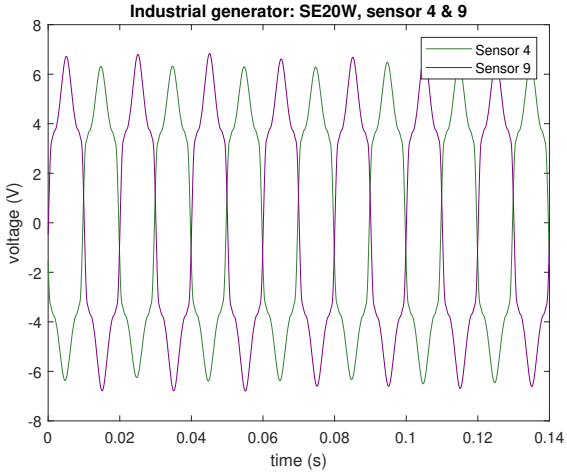

(b) Industrial generator model, no field-joints, 20 % static eccentricity at 180°, sensor 4 & 9.

Figure 5.13: Stray flux sensor voltages for one mechanical rotation of the industrial generator model exhibiting 20 % static eccentricity at 180°.

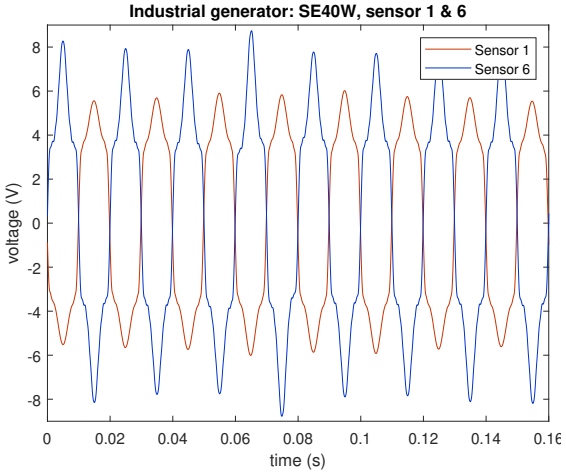

(a) Industrial generator model, no field-joints, 40 % static eccentricity at 180°, sensor 1 & 6.

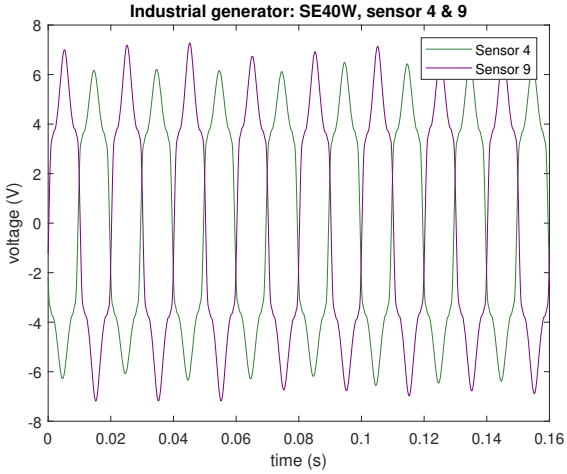

(b) Industrial generator model, no field-joints, 40 % static eccentricity at 180°, sensor 4 & 9.

Figure 5.14: Stray flux sensor voltages for one mechanical rotation of the industrial generator model exhibiting 40 % static eccentricity at 180°.

The next result, presented in figure 5.15, is of the industrial generator model exhibiting 40 % static eccentricity at 45°.

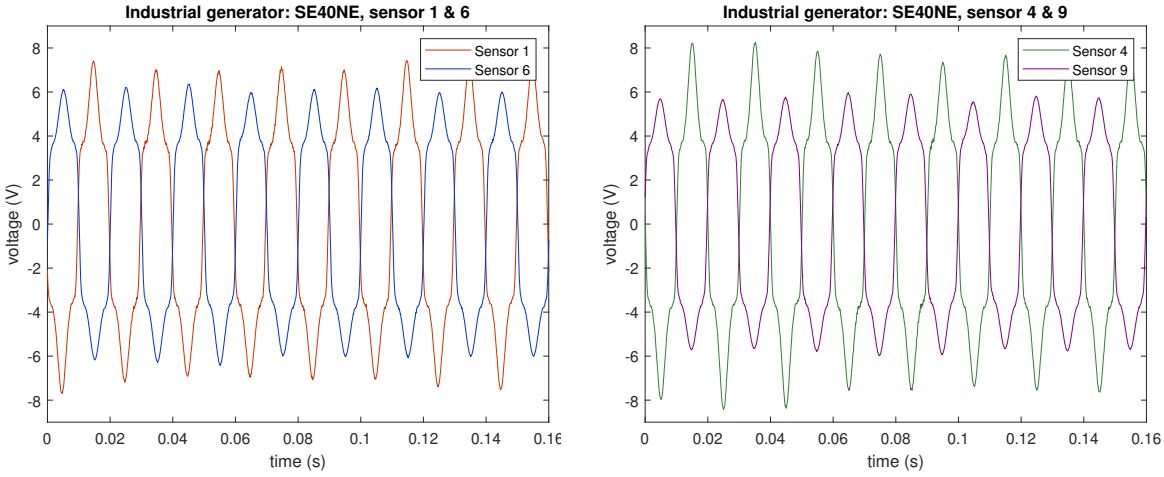

(a) Industrial generator model, no field-joints, 40 % static eccentricity at 45°, sensor 1 & 6.

(b) Industrial generator model, no field-joints, 40 % static eccentricity at 45°, sensor 4 & 9.

Figure 5.15: Stray flux sensor voltages for one mechanical rotation of the industrial generator model exhibiting 40 % static eccentricity at 45°.

Figure 5.16 presents the simulated stray flux sensor voltages for the industrial generator model exhibiting 15 % static eccentricity at 245°.

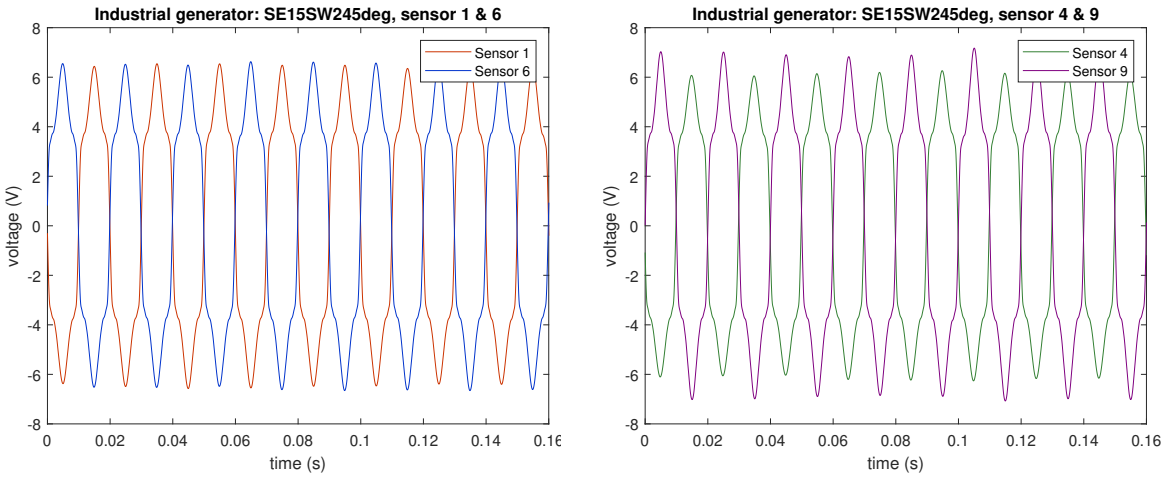

(a) Industrial generator model, no field-joints, 15 % static eccentricity at 245°, sensor 1 & 6.

(b) Industrial generator model, no field-joints, 15 % static eccentricity at 245°, sensor 4 & 9.

Figure 5.16: Stray flux sensor voltages for one mechanical rotation of the industrial generator model exhibiting 15 % static eccentricity at 245°.

5.3 Results Method III: Space vectors

In this section, the plotted results of the pattern recognition Method III, explained in section 4.3, are presented. The results are presented as figures 5.17 through 5.22. The intention of Method III is to use space vectors to reveal a pattern in the simulated sensor voltages. Four sensors have been used to create six space vectors of different sensor compositions. These compositions are presented in equation 4.1. The four sensors are positioned with 90° between them. They are here in the results numbered as 1, 2, 3 and 4. These numbers correspond to sensor 1, 4, 6 and 9 in figure 3.1 which displays the sensor naming on the laboratory generator.

Only simulations of laboratory generator models were utilized in Method III. For each of the six space vectors, four laboratory generator models were chosen to represent the results. First, as subfigure **(a)** in each result in figures 5.17 through 5.22, the space vector for the model without field-joints and without static eccentricity is presented. Subsequently, as figure **(b)**, **(c)** and **(d)**, three more models represent each space vector. As many of the results were quite similar, which models were chosen depend on the most interesting results. They therefore vary in the result figures.

Figure 5.17 displays the results for space vector $SV_{1,2}$ for four laboratory generator models. The first model, in **(a)** has no field-joints and no static eccentricity, named No SE in table 3.4. The second, in **(b)**, is SE20W ASYM TIGHT, explained in table 3.5. Figure **(c)** and **(d)** are SE20NE and SE40NE in table 3.4.

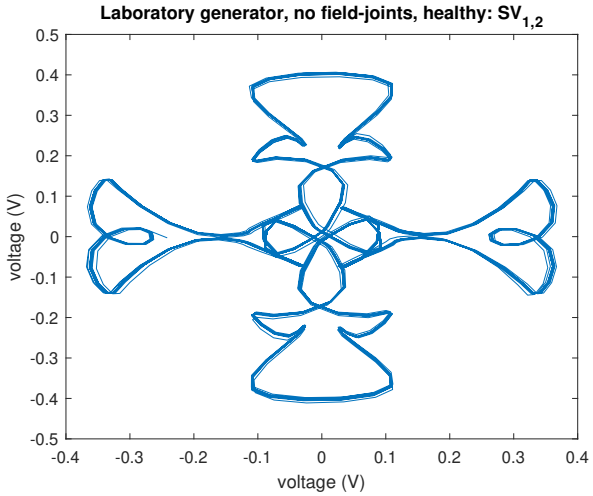

(a) Space vector $SV_{1,2}$, no field-joints, no static eccentricity.

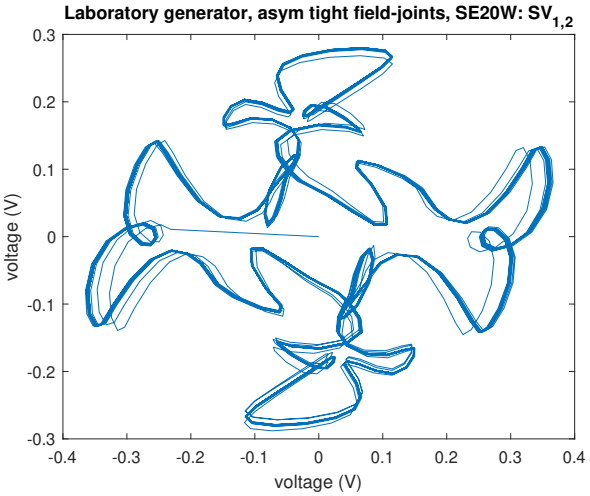

(b) Space vector $SV_{1,2}$, asymmetric tight field-joints, 20 % static eccentricity at 180°.

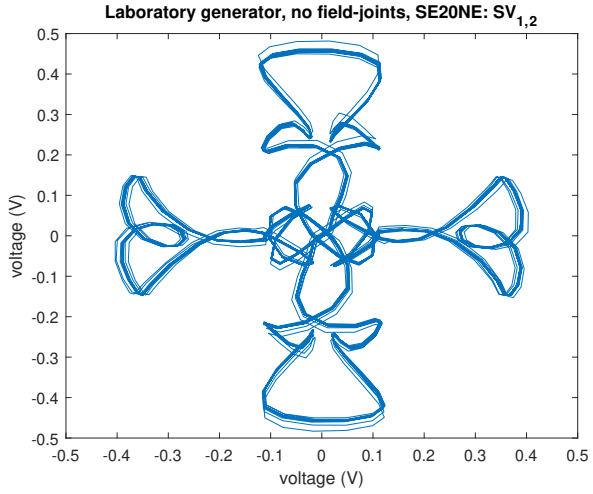

(c) Space vector $SV_{1,2}$, no field-joints, 20 % static eccentricity at 45°.

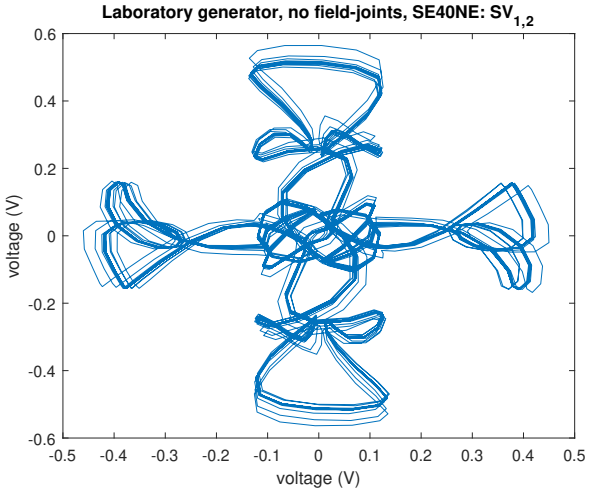

(d) Space vector $SV_{1,2}$, no field-joints, 40 % static eccentricity at 45°.

Figure 5.17: Plot of space vector $SV_{1,2}$ for four laboratory generator models.

In figure 5.18, the results can be observed for space vector $SV_{3,4}$ for four laboratory generator models. The first subfigure, **(a)**, is named No SE in explanation table 3.4, and has no field-joints and no static eccentricity. The second, **(b)**, is SE20W ASYM TIGHT in table 3.5. Figure **(c)** is SE20W in table 3.4, and **(d)** is SE20W SYM, also in table 3.5.

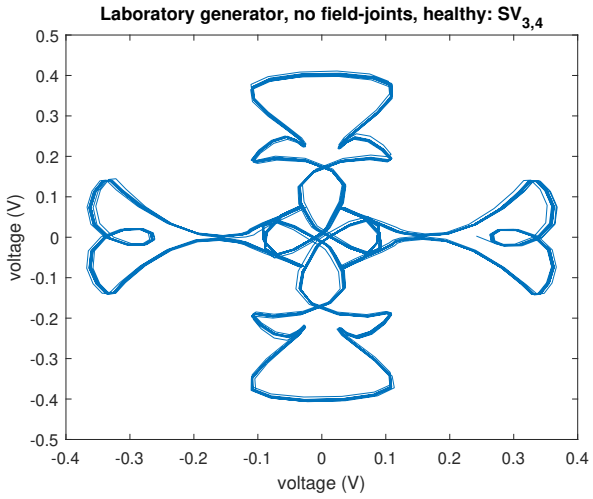

(a) Space vector $SV_{3,4}$, no field-joints, no static eccentricity.

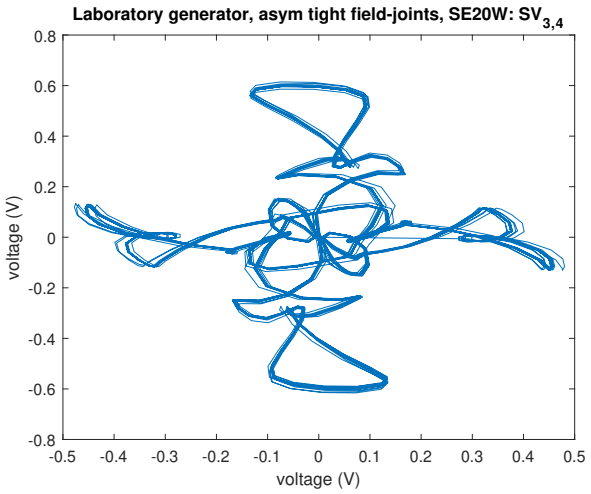

(b) Space vector $SV_{3,4}$, asymmetric tight field-joints, 20 % static eccentricity at 180°.

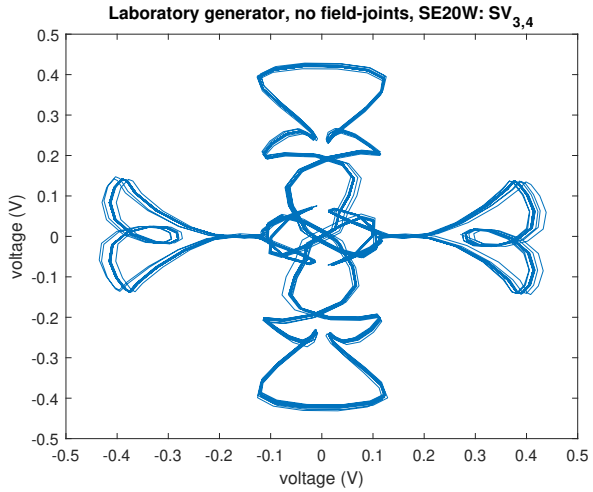

(c) Space vector $SV_{3,4}$, no field-joints, 20 % static eccentricity at 180°.

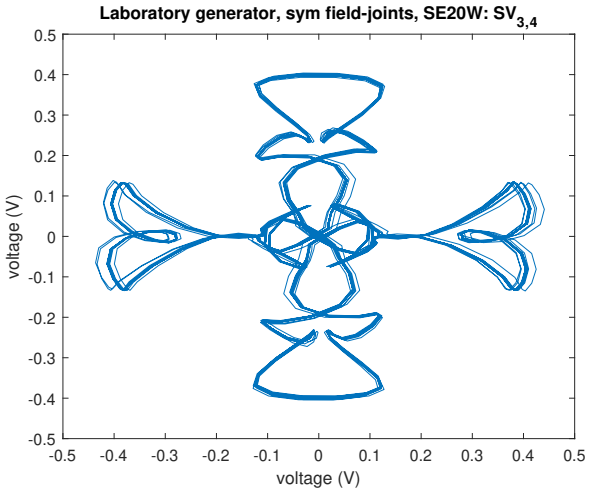

(d) Space vector $SV_{3,4}$, symmetric field-joints, 20 % static eccentricity at 180°.

Figure 5.18: Plot of space vector $SV_{3,4}$ for four laboratory generator models.

Figure 5.19 shows the results for space vector $SV_{1,3}$ for the following four laboratory generator models: Figure **(a)** presents No SE in explanation table 3.4. Figure **(b)** is SE20W ASYM TIGHT in table 3.5. Figures **(c)** and **(d)** are respectively SE20W and SE30W in table 3.4.

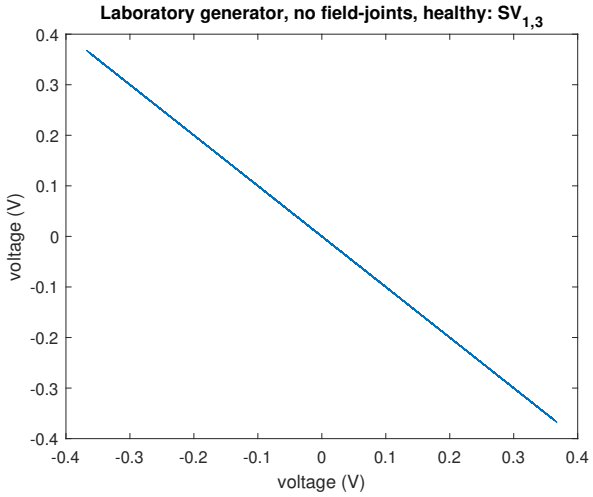

(a) Space vector $SV_{1,3}$, no field-joints, no static eccentricity.

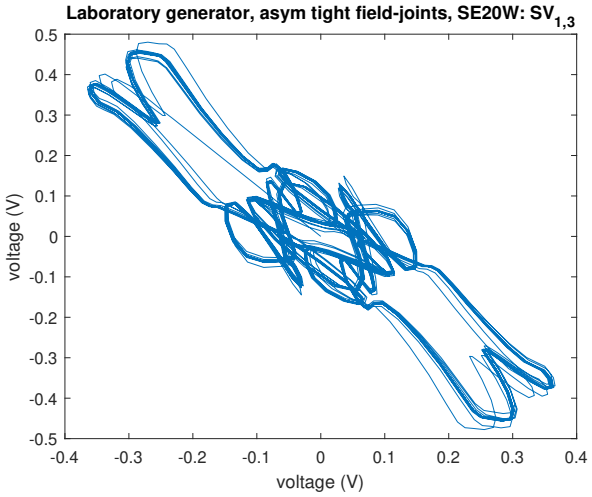

(b) Space vector $SV_{1,3}$, asymmetric tight field-joints, 20 % static eccentricity at 180°.

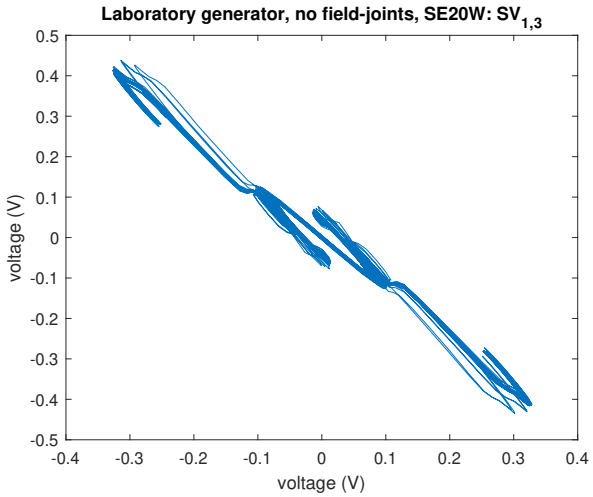

(c) Space vector $SV_{1,3}$, no field-joints, 20 % static eccentricity at 180°.

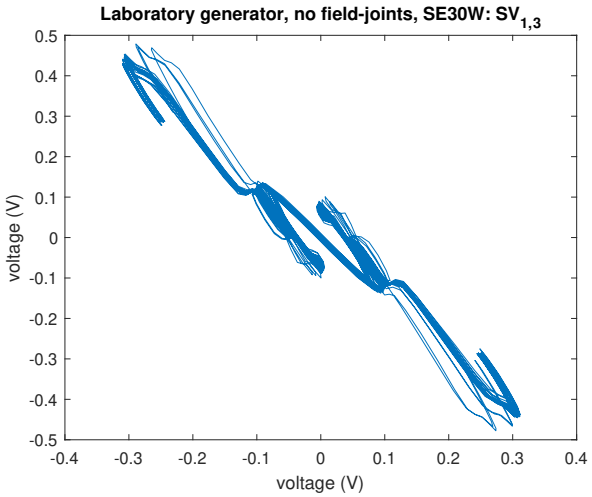

(d) Space vector $SV_{1,3}$, no field-joints, 30 % static eccentricity at 180°.

Figure 5.19: Plot of space vector $SV_{1,3}$ for four laboratory generator models.

In figure 5.20, the results are presented for space vector $SV_{2,4}$ for four laboratory generator models. Subfigure **(a)**, with no field-joints and no static eccentricity, is named No SE in table 3.4. Then, **(b)** is SE20W ASYM TIGHT in table 3.5. Finally, **(c)** and **(d)** are respectively SE20NE and SE40NE in table 3.4.

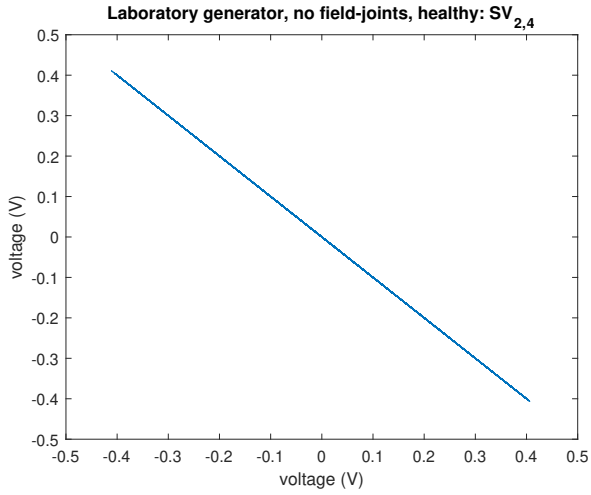

(a) Space vector $SV_{2,4}$, no field-joints, no static eccentricity.

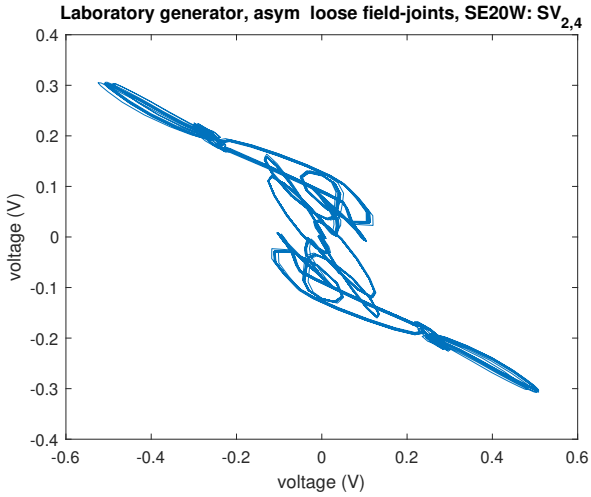

(b) Space vector $SV_{2,4}$, asymmetric loose field-joints, 20 % static eccentricity at 180°.

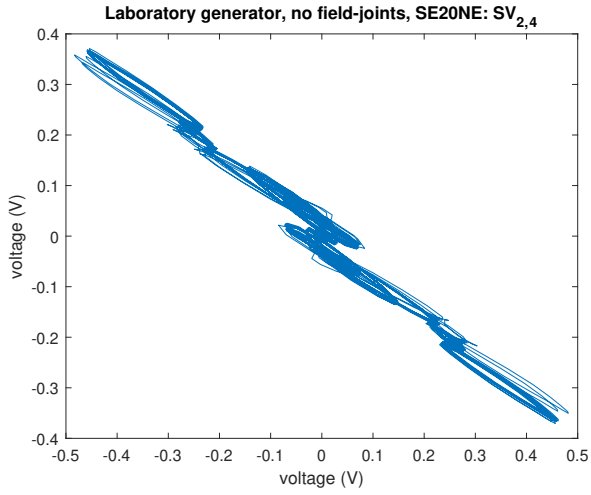

(c) Space vector $SV_{2,4}$, no field-joints, 20 % static eccentricity at 45°.

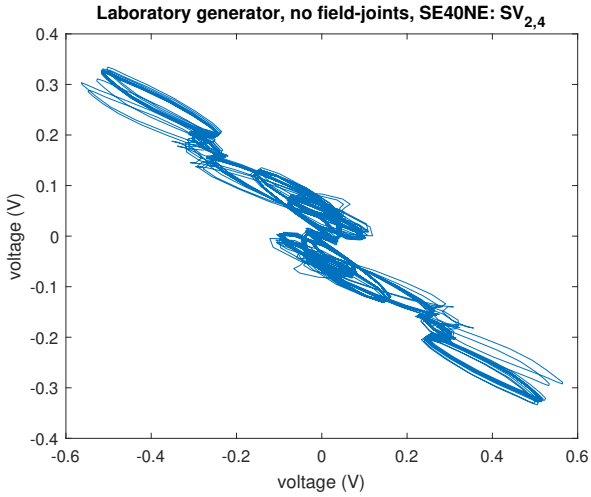

(d) Space vector $SV_{2,4}$, no field-joints, 40 % static eccentricity at 45°.

Figure 5.20: Plot of space vector $SV_{2,4}$ for four laboratory generator models.

Figure 5.21 presents the result plots for space vector $SV_{12,34}$ for four laboratory generator models. Subfigure **(a)** is still No SE in table 3.4, as with in all the other space vector figures. Subfigure **(b)** is SE20W ASYM LOOSE in table 3.5. Subfigures **(c)** and **(d)** are SE20W and SE50SE290deg in table 3.4.

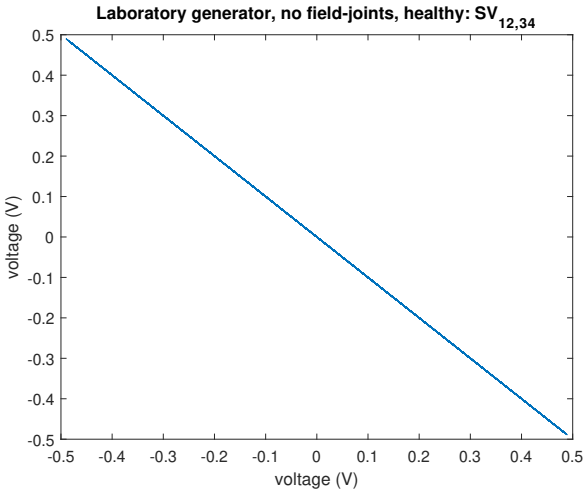

(a) Space vector $SV_{12,34}$, no field-joints, no static eccentricity.

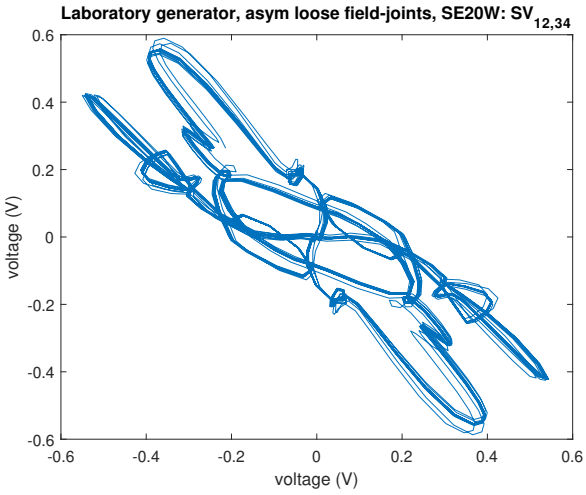

(b) Space vector $SV_{12,34}$, asymmetric loose field-joints, 20 % static eccentricity at 180°.

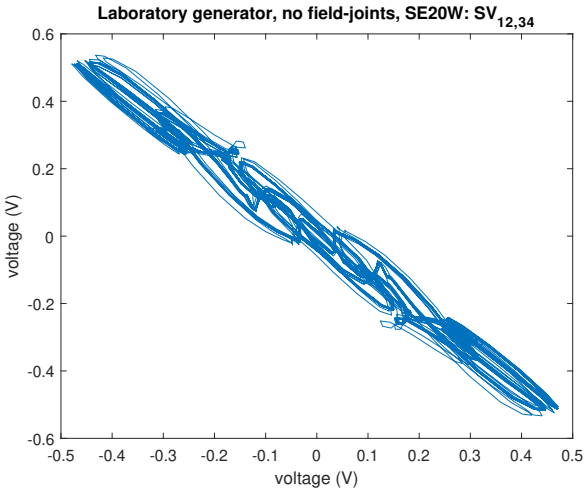

(c) Space vector $SV_{12,34}$, no field-joints, 20 % static eccentricity at 180°.

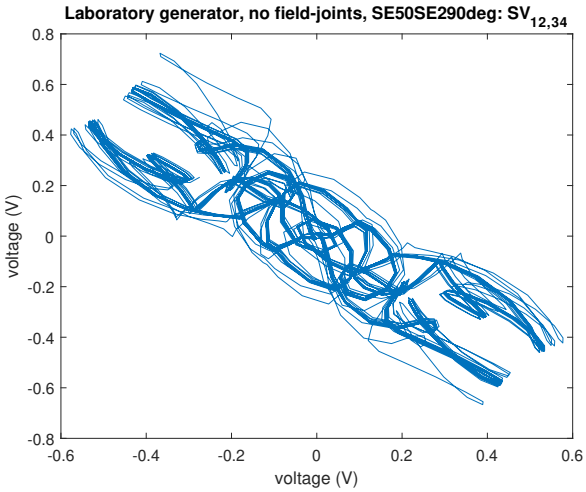

(d) Space vector $SV_{12,34}$, no field-joints, 50 % static eccentricity at 290°.

Figure 5.21: Plot of space vector $SV_{12,34}$ for four laboratory generator models.

In figure 5.22, the results can be observed for space vector $SV_{13,24}$ for four laboratory generator models. The first subfigure, **(a)**, is named No SE in explanation table 3.4, and has no field-joints and no static eccentricity. The second, **(b)**, is SE20W ASYM LOOSE in table 3.5. Subfigures **(c)** and **(d)** are SE20NE and SE40NE in table 3.4. It can be observed in figure **(a)**, that the healthy case is practically zero.

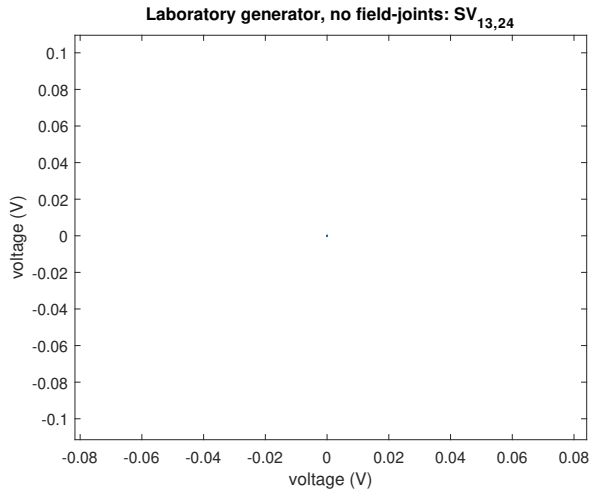

(a) Space vector $SV_{13,24}$, no field-joints, no static eccentricity.

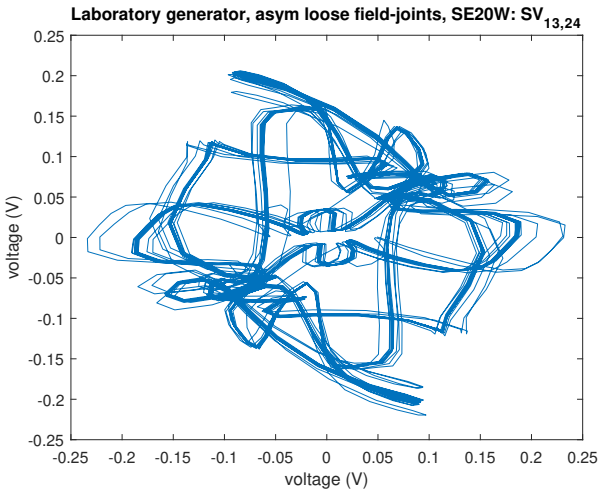

(b) Space vector $SV_{13,24}$, asymmetric loose field-joints, 20 % static eccentricity at 180°.

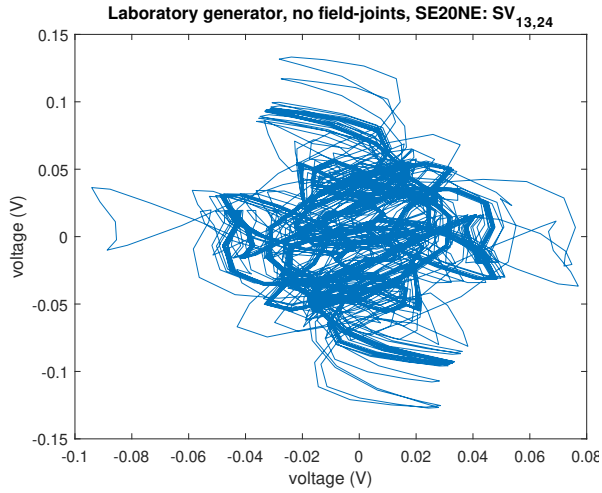

(c) Space vector $SV_{13,24}$, no field-joints, 20 % static eccentricity at 45°.

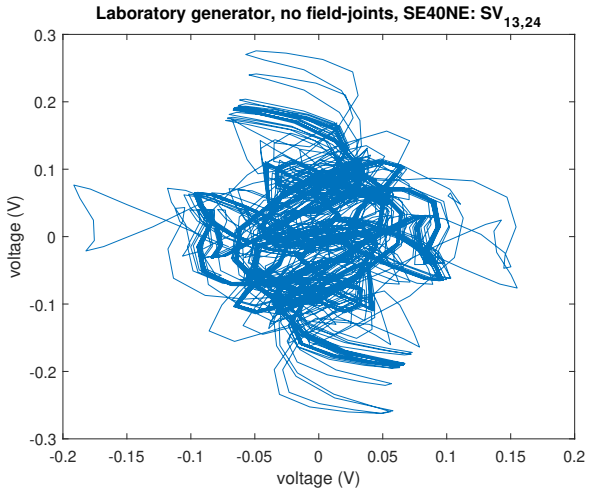

(d) Space vector $SV_{13,24}$, no field-joints, 40 % static eccentricity at 45°.

Figure 5.22: Plot of space vector $SV_{13,24}$ for four laboratory generator models.

5.4 Results Method IV: Computation of static eccentricity severity

In this section, the results from pattern recognition Method IV are presented. This method consisted of three different approaches to compute the severity of a static eccentricity. All three approaches utilize the RMS values of the stray flux sensor voltages. The voltages are presented for the laboratory generator models models exhibiting solely static eccentricity-fault in table 5.2, for the laboratory generator models with field-joints and static eccentricity in table 5.3, and for the industrial generator models in table 5.4.

Table 5.2: Simulated RMS voltages induced in the stray flux sensors for the laboratory generator models exhibiting only Static Eccentricity (SE).

Laboratory generator models with SE fault: RMS voltages					
Model name	**Sensor 1** RMS [V]	**Sensor 2** RMS [V]	**Sensor 3** RMS [V]	**Sensor 4** RMS [V]	**Average** RMS [V]
No SE	0.169	0.168	0.169	0.168	0.169
SE10E	0.180	0.173	0.163	0.167	0.171
SE20NE	0.179	0.188	0.164	0.155	0.171
SE40NE	0.188	0.208	0.158	0.142	0.174
SE20N	0.165	0.189	0.177	0.155	0.171
SE20NW	0.156	0.178	0.189	0.163	0.171
SE10W	0.163	0.167	0.180	0.173	0.171
SE20W	0.155	0.164	0.189	0.176	0.171
SE30W	0.149	0.161	0.200	0.180	0.173
SE15SW245deg	0.170	0.158	0.172	0.184	0.171
SE50SE290deg	0.204	0.143	0.145	0.214	0.176

Table 5.3: Simulated RMS voltages induced in the stray flux sensors for the laboratory generator models with a combined Static Eccentricity and Field-Joint (SEFJ) fault.

Laboratory generator models with SEFJ fault: RMS voltages					
Model name	**Sensor 1** RMS [V]	**Sensor 2** RMS [V]	**Sensor 3** RMS [V]	**Sensor 4** RMS [V]	**Average** RMS [V]
SE20N ASYM TIGHT	0.172	0.153	0.185	0.204	0.178
SE20W SYM	0.157	0.164	0.187	0.171	0.170
SE20W ASYM TIGHT	0.161	0.139	0.194	0.233	0.182
SE20W ASYM LOOSE	0.161	0.202	0.194	0.148	0.176
SE40SE355deg SYM	0.210	0.173	0.143	0.165	0.173
SE40SE355deg ASYM LOOSE	0.214	0.212	0.146	0.142	0.178

Table 5.4: Simulated RMS voltages induced in the stray flux sensors for the Industrial Generator (IG) models.

Industrial generator models: RMS voltages					
Model name	**Sensor 1** RMS [V]	**Sensor 2** RMS [V]	**Sensor 3** RMS [V]	**Sensor 4** RMS [V]	**Average** RMS [V]
IG Healthy	4.344	4.344	4.344	4.344	4.345
IG SE40NE	4.773	5.077	4.407	4.220	4.610
IG SE20W	4.351	4.459	4.757	4.610	4.466
IG SE30W	4.289	4.445	4.927	4.680	4.501
IG SE40W	4.245	4.440	5.137	4.767	4.554
IG SE15SW245deg	4.511	4.376	4.533	4.694	4.444

5.4.1 Results from Approach 1

In this subsection, the static eccentricity severities computed by means of Approach 1, explained in section 4.4.1, is presented. The SE severity for the laboratory generator models with only static eccentricity fault is presented in table 5.5. For the laboratory generator models with combined static eccentricity and field-joint fault it is presented in table 5.6. For the industrial generator models, only exhibiting static eccentricity, the results are presented in table 5.7.

Table 5.5: Computed Static Eccentricity (SE) severity for the laboratory generator models with only SE fault, by means of Approach 1.

Computation of SE severity: Approach 1				
Model name	V_x [%]	V_y [%]	**Severity** [%]	**Error** [%]
No SE	-0.005	0.008	0.013	0.013
SE10E	9.795	3.643	13.438	3.438
SE20NE	8.709	18.859	27.568	7.568
SE40NE	17.291	37.861	55.153	15.153
SE20N	-7.186	19.541	26.727	6.727
SE20NW	-19.009	8.624	27.633	7.633
SE10W	-9.735	-3.647	13.382	3.382
SE20W	-19.675	-7.208	26.884	6.884
SE30W	-29.673	-10.766	40.439	10.439
SE15SW245deg	-1.289	-15.506	16.795	1.795
SE50SE290deg	33.273	-40.238	73.511	23.511

Table 5.6: Computed Static Eccentricity (SE) severity for the laboratory generator models with combined SE and field-joint fault, by means of Approach 1.

Computation of SE severity: Approach 1				
Model name	V_x [%]	V_y [%]	**Severity** [%]	**Error** [%]
SE20N ASYM TIGHT	-7.494	-28.699	36.193	16.193
SE20W SYM	-18.169	-4.459	22.627	2.627
SE20W ASYM TIGHT	-18.186	-51.667	69.853	49.853
SE20W ASYM LOOSE	-18.432	30.644	49.076	29.076
SE40SE355deg SYM	38.780	4.365	43.145	3.145
SE40SE355deg ASYM LOOSE	38.145	39.353	77.498	37.498

Table 5.7: Computed Static Eccentricity (SE) severity for the Industrial Generator (IG) models, by means of Approach 1.

Computation of SE severity: Approach 1				
Model name	V_x [%]	V_y [%]	**Severity** [%]	**Error** [%]
IG Healthy	-0.003	0.000	0.003	0.003
IG SE40NE	7.921	18.536	26.458	-13.542
IG SE20W	-8.926	-3.319	12.245	-7.755
IG SE30W	-13.904	-5.132	19.036	-10.964
IG SE40W	-19.207	-7.049	26.256	-13.744
IG SE15SW245deg	-0.491	-7.026	7.516	-7.484

5.4.2 Results from Approach 2

This subsection presents the SE severity computed by means of Approach 2, which was explained in section 4.4.2. The severity for the laboratory generator models with only SE fault is presented in table 5.8, and for the models with combined SE and field-joint fault in table 5.9. The results for the industrial generator models are presented in table 5.10.

Table 5.8: Computed Static Eccentricity (SE) severity of the for the laboratory generator models with only SE fault, by means of Approach 2.

Computation of SE severity: Approach 2				
Model name	V_x [%]	V_y [%]	**Severity** [%]	**Error** [%]
No SE	-0.005	0.008	0.013	0.013
SE10E	9.765	3.654	13.419	3.419
SE20NE	8.708	18.861	27.569	7.569
SE40NE	17.412	37.601	55.013	15.013
SE20N	-7.202	19.497	26.699	6.699
SE20NW	-18.925	8.663	27.587	7.587
SE10W	-9.704	-3.658	13.363	3.363
SE20W	-19.544	-7.257	26.801	6.801
SE30W	-29.303	-10.904	40.207	10.207
SE15SW245deg	-1.290	-15.499	16.788	1.788
SE50SE290deg	33.649	-39.793	73.442	23.442

Table 5.9: Computed Static Eccentricity (SE) severity for the laboratory generator models with combined SE and field-joint fault, by means of Approach 2.

Computation of SE severity: Approach 2				
Model name	V_x [%]	V_y [%]	**Severity** [%]	**Error** [%]
SE20N ASYM TIGHT	-7.493	-28.702	36.195	16.195
SE20W SYM	-17.925	-4.520	22.445	2.445
SE20W ASYM TIGHT	-18.585	-50.583	69.167	49.167
SE20W ASYM LOOSE	-18.329	30.818	49.146	29.146
SE40SE355deg SYM	37.885	4.471	42.356	2.356
SE40SE355deg ASYM LOOSE	37.883	39.627	77.510	37.510

Table 5.10: Computed Static Eccentricity (SE) severity for the Industrial Generator (IG) models, by means of Approach 2.

Computation of SE severity: Approach 2				
Model name	V_x [%]	V_y [%]	**Severity** [%]	**Error** [%]
IG Healthy	-0.003	0.000	0.003	0.003
IG SE40NE	7.972	18.420	26.392	-13.608
IG SE20W	-8.907	-3.326	12.233	-7.767
IG SE30W	-13.835	-5.157	18.993	-11.007
IG SE40W	-19.027	-7.116	26.143	-13.857
IG SE15SW245deg	-0.491	-7.015	7.507	-7.493

5.4.3 Results from Approach 3

The following tables presents the SE severity computed by means of Approach 3, stated in section 4.4.3. Approach 3 could be a development of both Approach 1 and Approach 2. The results presented here build on Approach 1. The computed SE severites for the laboratory generator models with only a static eccentricity fault are presented in table 5.11. For the laboratory generator models with combined SE and field-joint fault, they are presented in table 5.12. The industrial generator model results are presented in table 5.13.

Table 5.11: Computed Static Eccentricity (SE) severity for the laboratory generator models with only SE fault, by means of Approach 3.

Computation of SE severity: Approach 3				
Model name	V_x [%]	V_y [%]	**Severity** [%]	**Error** [%]
No SE	-0.005	0.008	0.009	0.009
SE10E	9.795	3.643	10.450	0.450
SE20NE	8.709	18.859	20.773	0.773
SE40NE	17.291	37.861	41.623	1.623
SE20N	-7.186	19.541	20.820	0.820
SE20NW	-19.009	8.624	20.873	0.873
SE10W	-9.735	-3.647	10.395	0.395
SE20W	-19.675	-7.208	20.954	0.954
SE30W	-29.673	-10.766	31.566	1.566
SE15SW245deg	-1.289	-15.506	15.559	0.559
SE50SE290deg	33.273	-40.238	52.213	2.213

Table 5.12: Computed Static Eccentricity (SE) severity for the laboratory generator models with combined SE and field-joint fault, by means of Approach 3.

Computation of SE severity: Approach 3				
Model name	V_x [%]	V_y [%]	**Severity** [%]	**Error** [%]
SE20N ASYM TIGHT	-7.494	-28.699	29.661	9.661
SE20W SYM	-18.169	-4.459	18.708	-1.292
SE20W ASYM TIGHT	-18.186	-51.667	54.774	34.774
SE20W ASYM LOOSE	-18.432	30.644	35.760	15.760
SE40SE355deg SYM	38.780	4.365	39.025	-0.975
SE40SE355deg ASYM LOOSE	38.145	39.353	54.806	14.806

Table 5.13: Computed Static Eccentricity (SE) severity for the Industrial Generator (IG) models, by means of Approach 3.

Computation of SE severity: Approach 3				
Model name	V_x [%]	V_y [%]	**Severity** [%]	**Error** [%]
IG Healthy	-0.003	0.000	0.003	0.003
IG SE40NE	7.921	18.536	20.158	-19.842
IG SE20W	-8.926	-3.319	9.523	-10.477
IG SE30W	-13.904	-5.132	14.821	-15.179
IG SE40W	-19.207	-7.049	20.459	-19.541
IG SE15SW245deg	-0.491	-7.026	7.043	-7.957

5.5 Results method V: Computation of static eccentricity angle

This section presents the results from the computation of Static Eccentricity (SE) angles. They were computed with Time-Series Data Mining (TSDM), as explained in section 4.5. Results are presented firstly for the laboratory generator models, followed by the industrial generator models.

5.5.1 Laboratory generator models

The following four tables present the computed static eccentricity angle for the laboratory generator models. The computed Radius of Gyration (RoG) for the models exhibiting solely static eccentricity are presented in table 5.14. The computed angle and subsequent error is presented in table 5.15.

Table 5.14: Computed Radius of Gyration (RoG) for the laboratory generator models exhibiting only Static Eccentricity (SE) fault.

Laboratory generator models with SE fault: Computed RoG					
Model name	**RoG 1**	**RoG 2**	**RoG 3**	**RoG 4**	**RoG average**
No SE	0.0346	0.0341	0.0346	0.0340	0.0343
SE10E	0.0392	0.0347	0.0309	0.0339	0.0347
SE20NE	0.0406	0.0415	0.0300	0.0286	0.0352
SE40NE	0.0478	0.0510	0.0263	0.0241	0.0373
SE20N	0.0339	0.0439	0.0355	0.0272	0.0352
SE20NW	0.0291	0.0401	0.0420	0.0296	0.0352
SE10W	0.0310	0.0338	0.0392	0.0347	0.0347
SE20W	0.0277	0.0333	0.0443	0.0350	0.0351
SE30W	0.0250	0.0330	0.0506	0.0355	0.0360
SE15SW245deg	0.0328	0.0291	0.0369	0.0408	0.0349
SE50SE290deg	0.0456	0.0212	0.0271	0.0620	0.0390

Table 5.15: Calculated static eccentricity angles in the laboratory generator models exhibiting only Static Eccentricity (SE) fault, based on the radii of gyration presented in table 5.14.

Laboratory generator models with SE fault: Computed SE angle						
Model name	**diff 1** [-]	**diff 2** [-]	**share 1** [°mech]	**Share 2** [°mech]	**Angle** [°mech]	**Error** [°mech]
No SE	0.0003	0.0003	45.181	44.819	45.181	-
SE10E	0.0045	0.0000	89.211	0.789	0.789	0.789
SE20NE	0.0063	0.0054	48.504	41.496	48.504	3.504
SE40NE	0.0137	0.0105	51.035	38.965	51.035	6.035
SE20N	0.0088	0.0004	86.319	3.681	93.681	3.681
SE20NW	0.0068	0.0049	52.357	37.643	142.357	7.357
SE10W	0.0045	0.0000	89.277	0.723	180.723	0.723
SE20W	0.0092	-0.0001	91.018	-1.018	178.982	-1.018
SE30W	0.0146	-0.0005	93.302	-3.302	176.698	-3.302
SE15SW245deg	0.0059	0.0020	67.389	22.611	247.389	2.389
SE50SE290deg	0.0231	0.0066	69.882	20.118	290.118	0.118

The next two tables present the computed static eccentricity angle for the laboratory generator

simulation models exhibiting Static Eccentricity and Field-Joints (SEFJ). The computed RoGs for these models are presented in table 5.16. The computed SE angle with the errors are presented in table 5.17.

Table 5.16: Computed Radius of Gyration (RoG) for the laboratory generator models with combined Static Eccentricity and Field-Joint (SEFJ) fault.

Laboratory generator models with SEFJ fault: Computed RoG					
Model name	**RoG 1**	**RoG 2**	**RoG 3**	**RoG 4**	**RoG average**
SE20N ASYM TIGHT	0.0375	0.0337	0.0395	0.0391	0.0375
SE20W SYM	0.0283	0.0328	0.0437	0.0332	0.0345
SE20W ASYM TIGHT	0.0307	0.0264	0.0474	0.0495	0.0385
SE20W ASYM LOOSE	0.0302	0.0430	0.0468	0.0279	0.0370
SE40SE355deg SYM	0.0568	0.0317	0.0235	0.0353	0.0368
SE40SE355deg ASYM LOOSE	0.0593	0.0414	0.0251	0.0292	0.0387

Table 5.17: Computed static eccentricity angles for the laboratory generator models exhibiting Static Eccentricity and Field-Joint (SEFJ) fault, based on the radii of gyration presented in table 5.16.

Laboratory generator models with SEFJ fault: Computed SE angle						
Model name	**diff 1** [-]	**diff 2** [-]	**share 1** [°mech]	**Share 2** [°mech]	**Angle** [°mech]	**Error** [°mech]
SE20N ASYM TIGHT	0.0020	0.0017	48.952	41.048	221.048	131.048
SE20W SYM	0.0093	-0.0013	104.634	-14.634	165.366	-14.634
SE20W ASYM TIGHT	0.0110	0.0089	49.750	40.250	229.750	49.750
SE20W ASYM LOOSE	0.0099	0.0060	55.901	34.099	145.901	-34.099
SE40SE355deg SYM	0.0200	-0.0015	97.422	-7.422	367.422	12.422
SE40SE355deg ASYM LOOSE	0.0205	0.0027	79.691	10.309	10.309	15.309

5.5.2 Industrial generator models

In this subsection, results are presented from the computation of static eccentricity angular position in the industrial generator-models. The computed radii of gyration are presented in table 5.18, and the calculated angle based on these radii in table 5.19. There were made in total six different models of the industrial generator: one healthy model and five models with varying degrees and angles of static eccentricity. The naming of the models follows the standard presented in section 3.2.1.2 The first two letters represent "Static Eccentricity", followed by the severity percentage and then the angle as either two letters or two letters and the angle in degrees.

Table 5.18: Computed Radius of Gyration (RoG) for the Industrial Generator (IG) models.

Industrial generator models: Computed RoG					
Model name	**RoG 1**	**RoG 2**	**RoG 3**	**RoG 4**	**RoG average**
IG Healthy	0.2633	0.2633	0.2633	0.2633	0.2633
IG SE40NE	0.2905	0.3137	0.2683	0.2542	0.2817
IG SE20W	0.2592	0.2642	0.2836	0.2749	0.2705
IG SE30W	0.2570	0.2634	0.2965	0.2803	0.2743
IG SE40W	0.2548	0.2632	0.3147	0.2873	0.2800
IG SE15SW245deg	0.2686	0.2601	0.2688	0.2792	0.2692

Table 5.19: Computed static eccentricity angle for the industrial generator models, based on the radii of gyration presented in table 5.18.

Industrial generator models: Computed SE angle						
Model name	**diff 1** [-]	**diff 2** [-]	**share 1** [°mech]	**Share 2** [°mech]	**Angle** [°mech]	**Error** [°mech]
IG Healthy	0.0000	0.0000	45.3282	44.6718	44.6718	-
IG SE40NE	0.0320	0.0088	70.5503	19.4497	19.4497	25.5503
IG SE20W	0.0131	0.0044	67.4164	22.5836	202.5836	22.5836
IG SE30W	0.0222	0.0060	70.7703	19.2297	199.2297	19.2297
IG SE40W	0.0347	0.0073	74.2832	15.7168	195.7168	15.7168
IG SE15SW245deg	0.0100	-0.0004	93.6292	-3.6292	273.6292	28.6292

Chapter 6

Stray flux test on field-joints in a synchronous generator

In the course of both the preproject, as cited in [2], and this Master's thesis, a multitude of simulations have been executed on generator models with different types of field-joints and associated faults. However, until now, no real tests have been conducted on field-joints to validate the simulation-based results. In light of this, a field test was carried out on the field-joints of a salient-pole hydroelectric generator. This chapter presents a description of the test setup along with an analysis of the test result data.

6.1 Field test setup

A stray flux field test was performed on a 70 MVA hydroelectric generator with salient poles. The generator has two field-joints, located on opposite sides of the stator, 180° mech apart. Vibration tests, along with an external report, had previously indicated that the field-joints are faulty and ready for replacement. This was the first time a stray flux test would be performed on field-joints, in a stray flux project at NTNU. The test setup approach was therefore partly empirical, partly a new attempt.

The magnetic sensors used for the test are custom made stray magnetic field sensors [6]. An illustration of a sensor is provided in figure 6.1a. The sensors have a volume of approximately $100 \times 100 \times 10$ mm^3, and are made from 3000 turns of wound copper wire. They were fastened on the field-joints with double sided burr fastener tape. The tape side was attached to the stator backside, and the sensors could then easily be removed or fastened with the burr function. The measured sensor data was recorded with an oscilloscope, as presented in figure 6.1b.

The field test-generator has a vertical stator with two field-joints, located on opposite sides of the stator. The stator is protected by a shell, and physical contact is therefore only possible through hatches, as the ones pictured in figure 6.2a. The hatches in this picture lead to one of the field-joints. The other field-joint was accessed through identical hatches. Here, eight hatches

(a) The magnetic sensor used to measure the stray flux on the stator backside.

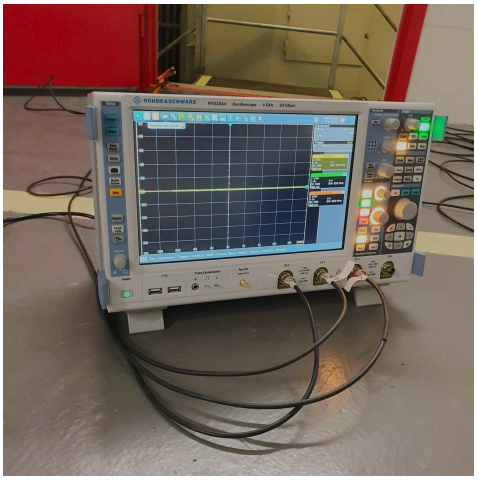

(b) The Rohde & Schwartz oscilloscope used to measure the voltages induced in the magnetic sensors.

Figure 6.1: One of the magnetic sensors and the oscilloscope utilized for the field test.

are visible, in four vertical rows. The six lowest of these hatches were opened to provide access to the field-joint.

Three sensors were installed on each field-joint, six sensors in total. The three sensors on each field-joint were installed at three different vertical levels, one sensor at each of the three lowest hatches in figure 6.2a. It was attempted to mount the sensor directly in the middle of the field-joint. In figure 6.2b, a picture of a sensor installed on a field-joint, ready for the field test, can be observed. The laminate groups between each horizontal air duct was numbered from 1 at the bottom to 36 at the top, as can partly be observed in figure 6.2b. These numbers were used for reference, to install the sensors on the opposite field-joint at identical height. The sensors were installed at numbers 7, 18 and 31.

The generator was running before the test started, and it therefore had to be stopped before any other activities could take place. The stator was then grounded according to Statkraft guidelines in order to secure safe physical contact, and surface of the stator backside was cleaned near the field-joints. The six sensors were installed according to the procedure explained in the previous paragraphs. The oscilloscope utilized has four channels, and so one field-joint was measured at a time.

The field test was performed in two parts, with two different load conditions: no load and partial load. Each recording of the oscilloscope lasted for 40 seconds at a sampling frequency of 10 kHz. The procedure was therefore to first magnetize the generator with only the magnetization current. Then the no load measurements were made, on one field-joint at a time. The generator was then loaded with a small load, and the measurements were retaken in the same way for each field-joint.

After the field test was performed, the generator was disconnected from the load, stopped and grounded again to allow for safe dismounting of the sensors.

(a) Hatches through which field-joints were accessed. Sensors were installed at three vertical hatch levels.

(b) Magnetic sensor installed on a field-joint.

Figure 6.2: Pictures of **(a)** the stator shell with the hatches through which the field-joints were accessed, and **(b)** a search coil sensor installed on a field-joint.

6.2 Field test results

In this section, the voltages measured in the field test are presented. Three electrical periods are presented for each measurement. The field-joints are hereby named Field-joint 1 and Field-joint 2. Figure 6.3 presents the no load test results. The results from the partial load-test are presented in figure 6.4. In all figures the voltage plots are named either "top", "middle" or "bottom", as a reference to the vertical location on the field-joint of the sensor recording the voltage.

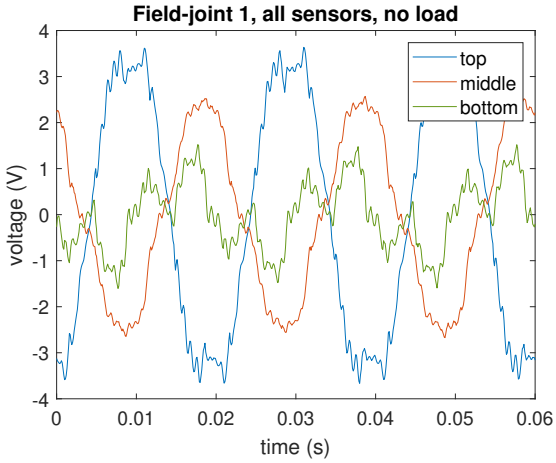

(a) Measured stray flux sensor voltages in the field test generator on no load, for Field-joint 1.

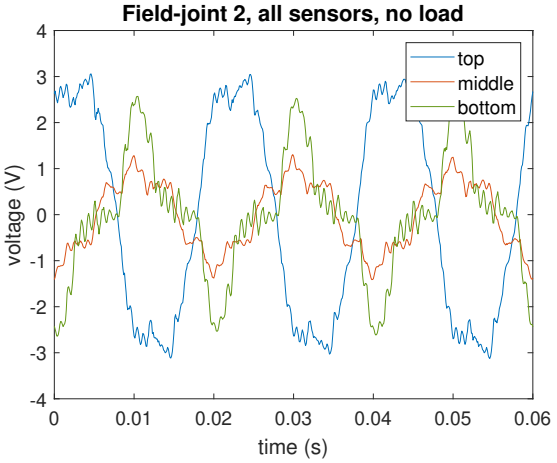

(b) Measured stray flux sensor voltages in the field test generator on no load, for Field-joint 2.

Figure 6.3: Three electrical periods of the measured stray flux sensor voltages for the left and right field-joint, with the field test generator running on no load. The three sensors on each side of the machine were installed at the top, middle and at the bottom of each field-joint.

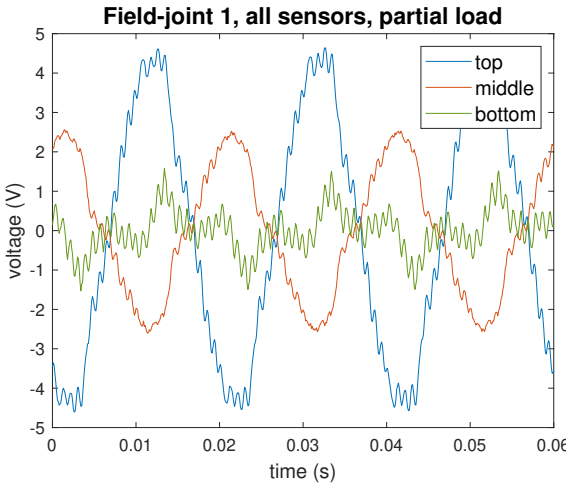

(a) Measured stray flux sensor voltages in the field test generator on partial load, for Field-joint 1..

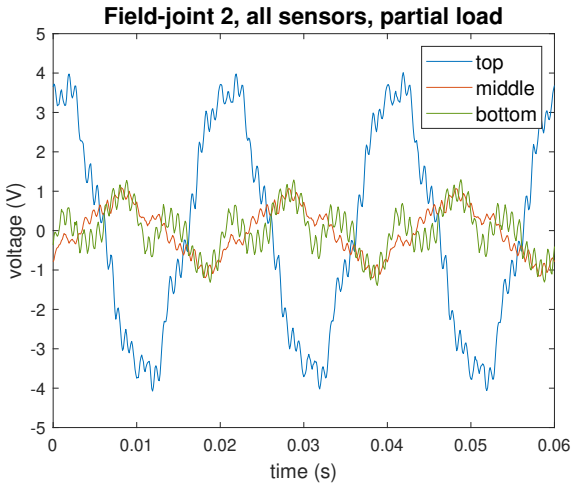

(b) Measured stray flux sensor voltages in the field test generator on partial load, for Field-joint 2.

Figure 6.4: Three electrical periods of the measured stray flux sensor voltages at the two field-joint, with the field test generator running on partial load. The three sensors on each side of the machine were installed at the top, middle and at the bottom of each field-joint.

In table 6.1, the RMS voltages for the stray flux measurements performed during the field test are presented. It can be observed that the induced voltages vary depending on the position of the sensor, the field-joint and also the load case.

Table 6.1: RMS voltages recorded by the six magnetic sensors, installed at the top, middle or bottom of each field-joint, under both load cases during the field test.

Field test results: recorded RMS voltages				
Name	**Load case**	**Top** [V]	**Middle** [V]	**Bottom** [V]
Field-joint 1	No load	2.577	1.733	0.719
Field-joint 2	No load	2.221	0.735	1.268
Field-joint 1	Partial load	3.047	1.639	0.542
Field-joint 2	Partial load	2.560	0.587	0.567

Chapter 7

Stray flux test on static eccentricity in two generators

This chapter contains analysis on previously collected stray flux data, conducted to evaluate the efficacy of the methods developed for diagnosing static eccentricity faults. The data was obtained from two salient-pole generators, one with and one without field-joints. Due to confidentiality and safety regulations, specific information regarding the two generators, including their name, location and data, cannot be revealed. Henceforth, the generators will be referred to as Generator 1 and Generator 2.

The stray flux data was gathered for several load cases for both generators. The sensor calibration was tested post-measurements, and found to be within acceptable limits. The methodology utilized to compute the severity of the static eccentricity is Approach 3 Method III, presented in 4.4.3. The method used to compute the angle is Method V, presented in 4.5. The analyzed results are presented for Generator 1 in section 7.1 and for Generator 2 in section 7.2.

7.1 Results for Generator 1

The first generator is called Generator 1. There were reported anomalies associated with Generator 1. It must be disclosed that this generator has field-joints, but they were not considered during the field test, as no research on field-joints had yet initiated when the test took place. The stray flux sensors were not located close to the field-joints during the field test. The stray flux data from Generator 1 was collected for two load cases: no load-case and a half load-case. The data was sampled at 10 kHz.

Table 7.1 presents the RMS voltages measured by four stray flux sensors. This data is used to compute the static eccentricity severity in the two load cases, by means of Approach 3 in Method IV, which was introduced in section 4.3. The severities for both load cases are presented in table 7.2. They appear to be significantly high, which may raise questions regarding their accuracy. The computed radii of gyration for the two load cases are presented in table 7.3, while table 7.4 presents the static eccentricity's angular position.

Table 7.1: RMS voltages measured in the four stray flux sensors on Generator 1.

Generator 1: Recorded RMS voltages					
Load status	**RMS 1** [V]	**RMS 2** [V]	**RMS 3** [V]	**RMS 4** [V]	**RMS average** [V]
No load	0.386	0.613	0.929	0.781	0.677
Half load	0.452	0.679	0.989	0.838	0.740

Table 7.2: Calculated Static Eccentricity (SE) severity in Generator 1, based on the measured voltages presented in table 7.1.

Generator 1: Computed SE severity			
Load status	**x-direction** [-]	**y-direction** [-]	**Severity** [%]
No load	-0.802	-0.248	83.9763
Half load	-0.726	-0.215	75.7436
Average	-0.764	-0.232	79.8584

Table 7.3: Radius of Gyration (RoG) values computed for Generator 1.

Generator 1: Computed RoG					
Load status	**RoG 1**	**RoG 2**	**RoG 3**	**RoG 4**	**RoG average**
No load	0.0716	0.102	0.184	0.175	0.133
Half load	0.066	0.090	0.183	0.164	0.126

Table 7.4: Calculated Static Eccentricity (SE) angle in Generator 1, based on the radii of gyration presented in table 7.3.

Generator 1: Computed SE angle					
Load status	**diff 1** [-]	**diff 2** [-]	**share 1** [degrees°]	**Share 2** [degrees°]	**Angle** [degrees°]
No load	0.0507	0.0417	49.373	40.627	220.627
Half load	0.0574	0.0385	53.867	36.130	216.130
Average	0.0541	0.0401	51.621	38.379	218.379

7.2 Results for Generator 2

The second generator is called Generator 2. This generator does not have field-joints. The stray flux data was collected for four load cases: no load, half load and two full-load cases. As for Generator 1, the data was sampled at 10 kHz.

The measured RMS voltages from four sensors are presented in table 7.5. They were applied to compute the static eccentricity severity presented in table 7.6. The measured voltages were also used to compute the radius of gyration for all load cases, presented in table 7.7. Finally, table 7.8 presents the computed angles corresponding to the static eccentricity calculations.

Table 7.5: RMS voltages measured in the four stray flux sensors on Generator 2.

Generator 2: Recorded RMS voltages					
Load status	**RMS 1** [V]	**RMS 2** [V]	**RMS 3** [V]	**RMS 4** [V]	**RMS average** [V]
No load	1.408	1.773	2.020	1.443	1.661
Half load	1.487	1.901	2.157	1.546	1.773
Full load 1	1.322	1.789	1.901	1.432	1.611
Full load 2	1.536	2.099	2.158	1.682	1.868

Table 7.6: Calculated Static Eccentricity (SE) severity in Generator 2, calculated from the measured voltages presented in table 7.5.

Generator 2: Computed SE severity			
Load status	**x-direction** [-]	**y-direction** [-]	**Severity** [%]
No load	-0.368	-0.199	41.8703
Half load	-0.378	-0.201	42.8036
Full load 1	-0.360	0.222	42.2519
Full load 2	-0.333	0.223	40.0505
Average	-0.360	-0.211	41.7073

Table 7.7: Radius of Gyration (RoG) values computed for Generator 2.

Generator 2: Computed RoG					
Load status	**RoG 1**	**RoG 2**	**RoG 3**	**RoG 4**	**RoG average**
No load	0.187	0.256	0.275	0.196	0.229
Half load	0.193	0.270	0.285	0.218	0.242
Full load 1	0.175	0.256	0.274	0.197	0.225
Full load 2	0.223	0.306	0.319	0.242	0.272

Table 7.8: Calculated Static Eccentricity (SE) angle in Generator 2, based on the radii of gyration presented in table 7.7.

Generator 2: Computed SE angle					
Load status	**diff 1** [-]	**diff 2** [-]	**share 1** [degrees°]	**Share 2** [degrees°]	**Angle** [degrees°]
No load	0.0467	0.0278	56.379	33.621	146.379
Half load	0.0439	0.0282	54.744	35.357	144.744
Full load 1	0.0484	0.0303	55.367	34.634	145.367
Full load 2	0.0465	0.0331	52.582	37.412	142.582
Average	0.0464	0.0299	54.768	35.232	144.768

Chapter 8

Discussion of results

This chapter offers a comprehensive analysis and discussion of the results acquired, which are detailed in the chapters 5: Pattern recognition results on simulated models, 6: Stray flux test on field-joints in a synchronous generator and 7: Stray flux test on static eccentricity in two generators. Some general discussion points regarding limitations and considerations pertaining to the methodologies and procedures are provided. Based on the analysis, an algorithm is presented for the fault diagnosis of a synchronous generator with either field-joint fault, static eccentricity fault or a combination of the two. Finally, some suggestions are presented as possible prospective steps for future research, building upon the work presented in this thesis.

8.1 Discussion of pattern recognition results on the simulated models

In this section, the results obtained from the pattern recognition analyses of the simulated models are further examined. The results were presented in chapter 5: Pattern recognition results on simulated models. Each result section in chapter 5 is analyzed here in a separate subsection, except for Method I, as these results were repeated from the preproject. The plots were included as they are relevant for future discussion, and a thorough discussion regarding these results alone can therefore be found in [2]. Finally, the laboratory generator models with both field-joint fault and static eccentricity are analyzed separately, as these results consistently diverged from the models with only static eccentricity.

The base simulation models for both the laboratory generator and the industrial generator underwent rigorous testing for diverse applications, prior to the commencement of this Master's thesis. The term "base simulation models" refers to the two models of healthy generators without field-joints. They have been refined over time, and it is assumed that any significant errors or sources of discrepancy would have been identified before the models were utilized in this project. Therefore, no decisive model faults are anticipated or considered.

8.1.1 Method II: Discussion of the general voltage comparison

In this subsection, the results obtained in section 5.2 of chapter 5: Pattern recognition results on simulated models are analyzed. The essence of this method was a general presentation of the behaviour, shape and size of the stray flux sensor voltages during static eccentricity fault and during a combination of static eccentricity and field-joint fault.

Static eccentricity increases the recorded stray flux voltage at the sensors closer to the smaller air gap side, and decrease the voltage at the opposite side. This is illustrated in figure 8.1, which displays four stray flux sensor voltages for a laboratory generator model with 20 % static eccentricity at 180° and without field-joints. Without static eccentricity, the voltage amplitudes would be approximately equal in respectively 8.1a and 8.1b. Instead, in figure 8.1a, the voltage peak is 0.11 V higher in Sensor 6 compared to Sensor 1, which is due to the smaller reluctance on the smaller air gap side.

In figure 8.1b, it can be observed that the static eccentricity manifests as a slight voltage amplitude difference also in Sensor 4 and Sensor 9. As these sensors are equidistant from the static eccentricity's angular position, the air gap length, and thus magnetic reluctance, is identical at both sensors. The reason for the observed voltage variation is due to the winding layout in the laboratory generator. As previously stated, there are seven magnetic symmetries in the generator [16]. The magnetic flux density pattern is therefore repeated seven times in the air gap. The symmetry axis is not directly through Sensor 4 and Sensor 9, which is why static eccentricity is expressed differently in each of these sensors.

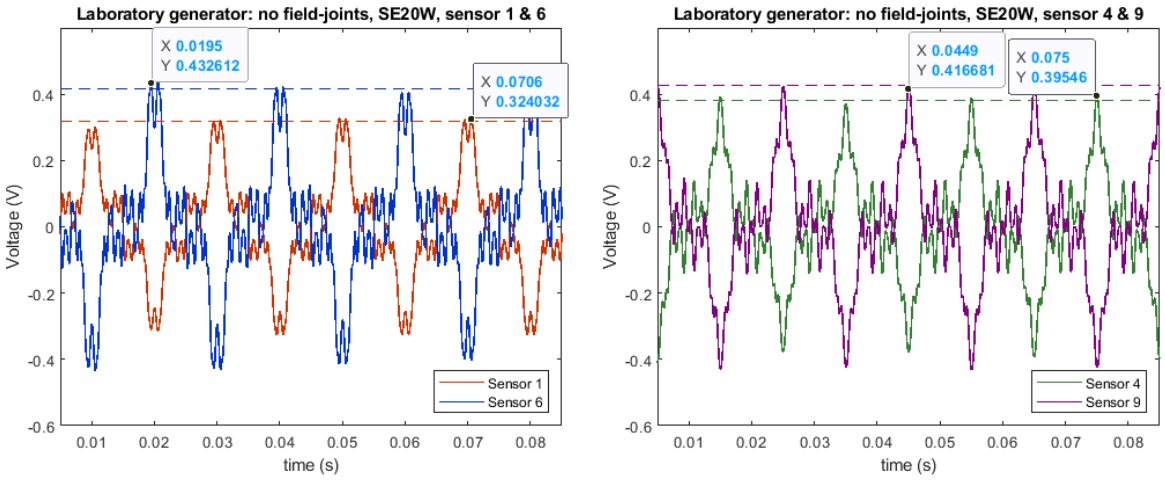

(a) Simulated voltages in Sensor 1 & 6.

(b) Simulated voltages in Sensor 4 & 9.

Figure 8.1: Voltage amplitude differences in **(a)** Sensor 1 & 6 and **(b)** Sensor 4 & 9, for the laboratory generator model with 20 % static eccentricity at 180° and without field-joints.

The voltage plots presented in section 5.2 show that the field-joints have larger effect on the stray flux voltage than a static eccentricity fault. This is also visualized in figure 8.2. The figures show normalized RMS values of the stray flux voltage for the four sensors 1, 4, 6 and 9 for selected

laboratory generator models with SE fault and with SEFJ fault. The normalization method used is min-max normalization: the minimum voltages has been subtracted from all voltages and the result was then divided by the difference between the maximum and minimum voltage. This normalizes every RMS voltage value to a number between 0 and 1.

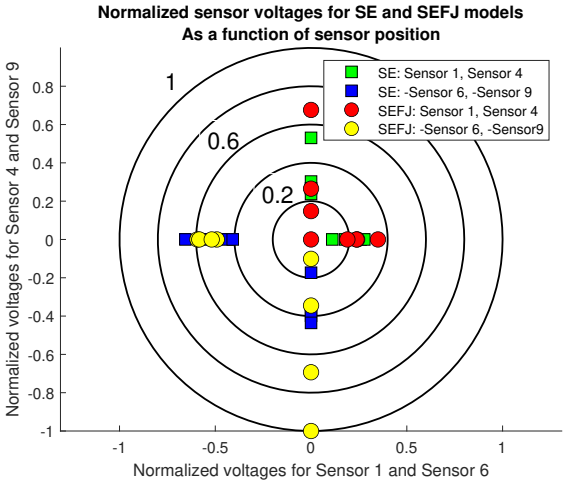

(a) Normalized sensor voltages, plotted on an axis mirroring the sensors' position. For sensors 6 & 9, the plotted values are therefore multiplied by -1.

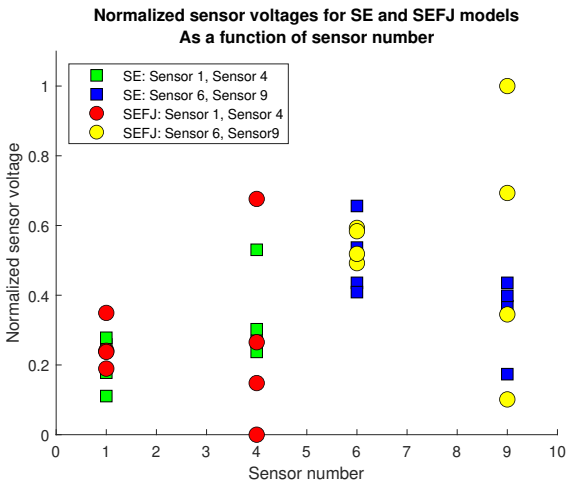

(b) Normalized sensor voltages, plotted by sensor number.

Figure 8.2: Comparison of the simulated voltages in Sensor 1, 4, 6 and 9, normalized with min-max feature scaling, for the laboratory generator models with Static Eccentricity (SE) and Static Eccentricity and Field-joints (SEFJ). The values are categorized by fault type and **(a)** sensor angular position, and **(b)** sensor number.

In figure 8.2a, sensor voltages from the laboratory generator models with Static Eccentricity (SE) and with Static Eccentricity and Field-Joints (SEFJ) are plotted on axes corresponding to their sensor positions. The voltages for Sensor 6 and Sensor 9 are therefore turned into negative values, by multiplication with -1. All voltage values were normalized to a value between 0 and 1 by means of min-max feature scaling. The figure shows that the values for Sensor 4 & 9 are more dispersed than the values for Sensor 1 & 6. More specifically, the voltages from the SEFJ-models are more dispersed than the models solely exhibiting static eccentricity. This indicates that the field-joints have a larger effect on the simulated stray flux voltage than static eccentricity. The same can be observed in figure 8.2b, where the normalized voltages are plotted by sensor number. The same normalization procedure as in figure 8.2a was utilized, but the values from Sensor 6 and 9 are not multiplied by -1. The perception of both figures is influenced by the choice of included models.

The standard deviations of all the laboratory generators models have been computed for Sensor 1, 4, 6 and 9. The results are presented in table 8.1. It shows that the standard deviation, a statistical tool to measure diversification, is larger for the models with both field-joint and static eccentricity fault, for all models. The difference in percentage is larger for Sensor 9 than for the other sensors, which can be explained from the structure and position of the field-joints: all the models were made with a healthy field-joint at the top position, at Sensor 4, and either a healthy, a looser or a tighter field-joint at the bottom position at Sensor 9.

Table 8.1: Computed standard deviations for Sensors 1, 4, 6 and 9 for the laboratory generator models with Static Eccentricity (SE) fault, Field-Joints (FJ) and with Static Eccentricity and Field-Joints (SEFJ).

Standard deviations for Sensor 1, 4, 6 and 9				
Model type	**Sensor 1** [V]	**Sensor 4** [V]	**Sensor 6** [V]	**Sensor 9** [V]
Static eccentricity	0.0160	0.0177	0.0158	0.0187
Field-joints	0.0028	0.0264	0.0027	0.0333
Static eccentricity and field-joints	0.0237	0.0260	0.0218	0.0318
Difference: SEFJ to SE [V]	0.0077	0.0083	0.0060	0.0131
Difference: SEFJ to SE [%]	48.13	46.89	37.97	70.05
Difference: SEFJ to FJ [V]	0.0209	-0.0004	0.0191	-0.0015
Difference: SEFJ to FJ [%]	746.43	-1.52	707.41	-4.50

Standard deviations were also computed for the RMS values of the laboratory generator models with field-joint variations, for Sensors 1, 4, 6 and 9. These simulations were performed in the preproject [2]. The computed standard deviations are presented in table 8.1. When comparing the SEFJ- and FJ-models, the difference in standard deviation is positive and very large for Sensor 1 and Sensor 6. This indicates that Sensors 1 and 6 are more sensitive to static eccentricity fault than field-joint fault. Interestingly, the same difference for Sensor 4 and Sensor 9 is negative, but very small. This indicates that for Sensors 4 and 9, a static eccentricity fault has little influence on the variability in the models with both field-joints and static eccentricity compared to the field-joints.

It should be noted that the standard deviation was calculated with a rather small sample size. More models, especially with both field-joints and a static eccentricity fault could have be simulated in order to increase the reliability of the computed standard deviation value.

8.1.2 Method III: Discussion of space vectors

In this section, the results obtained in section 5.3 of chapter 5: Pattern recognition results on simulated models are analyzed. The method introduced the concept of space vectors, with the goal of discovering patterns and relations between the stray flux sensor voltages. The analyzed measurements stem from the four sensors which correspond to Sensors 1, 4, 6 and 9 in figure 8.7. The various constructed space vectors can be found in equation (4.1). Six result figures, figures 5.17 through 5.22, were created; one for each constructed space vector. Furthermore, each figure consists of four subfigures of space vector plots from selected laboratory generator models. In all figures, subfigure **(a)** display the space vector computed for the laboratory generator model without field-joints and without static eccentricity, to show the space vector plot in a healthy condition.

The voltage data is recorded from eight full rotations of the laboratory generator. On closer inspection of the pattern in figure 5.17, it is revealed that they are repeated 56 times, which can be factorized to $56 = 7 \cdot 8$. This can be explained from the number of full rotations and the number of pole pairs in the laboratory generator, which is seven. The pattern is thus repeated once for every electrical period in the generator.

The cyclic repetition of data plots is more concentrated in the models without any field-joints or eccentricity fault, in all result figures. In figure 5.17a, enlarged in figure 8.3a the minimum value at the top left loop was found to be -0.359 V, while it was found to be -0.366 V at the outer end of the top left loop. There is therefore a difference of 0.007 V from largest to smallest value. In comparison, in figure 5.17c, the difference was found to be 0.019 V. In figure 5.17d, also enlarged in figure 8.3b, the difference was 0.038 V, and it can be observed on the figure that it is even larger on the bottom left loop. The increasing in asymmetry in the cyclic pattern from healthy models to an increasing degree of eccentricity is a trend in all the result figures.

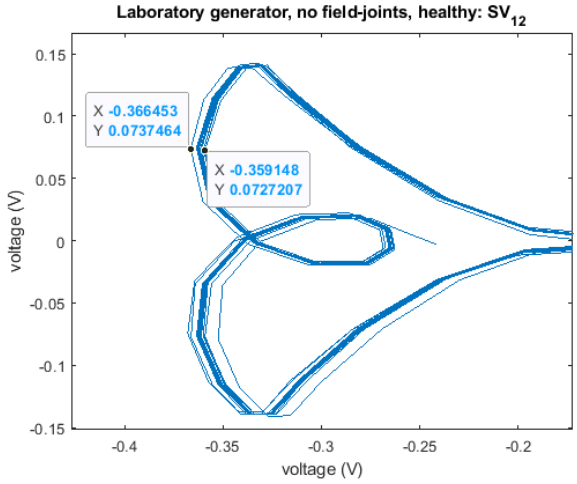

(a) Enlarged plot of space vector $SV_{1,2}$ for the laboratory generator model without both field-joints and static eccentricity.

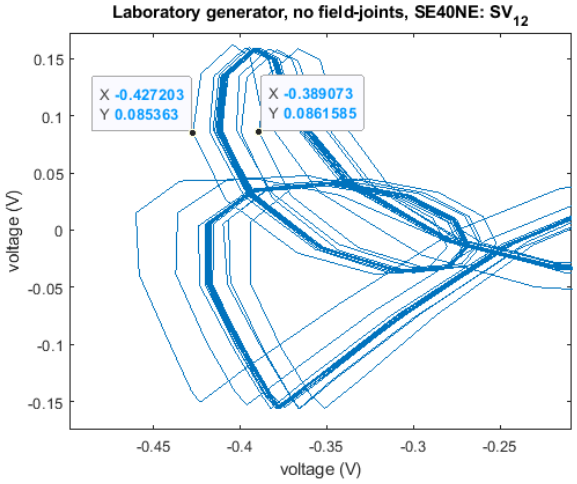

(b) Enlarged plot of space vector $SV_{1,2}$ for the laboratory generator model without field-joint and with 40 % static eccentricity at 45°.

Figure 8.3: Enlarged plots of space vector SV_{12} for the laboratory generator model without field-joints and **(a)** no static eccentricity, and **(b)** 40 % static eccentricity at 45°. The static eccentricity increases the dispersion in the cyclic space vector pattern.

An interesting phenomenon occurs for space vectors constructed for models with faulty field-joints. The skew in magnetic forces causes the space vector to form an odd symmetric figure, instead of what was previously even symmetry. This can be observed in figure 5.17b and 5.18b.

Healthy field-joints, i.e. field-joints with equal widths, do not seem to affect the dispersion or symmetry in the same was as eccentricity or faulty field-joints do. In figure 5.18c, the dispersion at the top right loop was measured to be 0.032 V between minimum and maximum cyclic repetition. In figure 5.18d, which has healthy field-joint, the dispersion was measured as 0.038 V. This difference is small compared to in the case in figure 8.3. The measuring points are enlarged and presented in figure 8.4a and figure 8.4b.

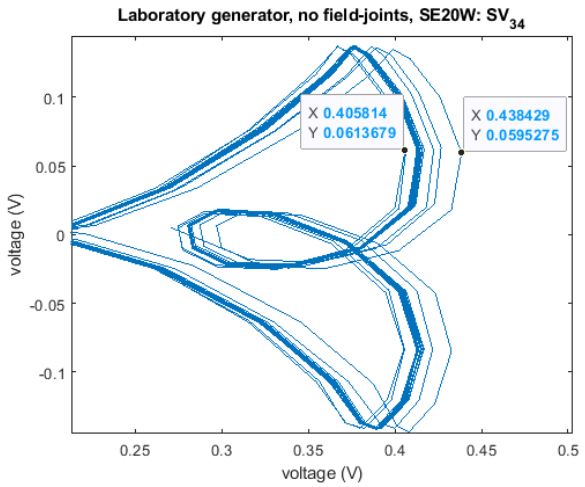

(a) Enlarged plot of space vector $SV_{3,4}$ for the laboratory generator model with 20 % static eccentricity at 180° and without field-joints.

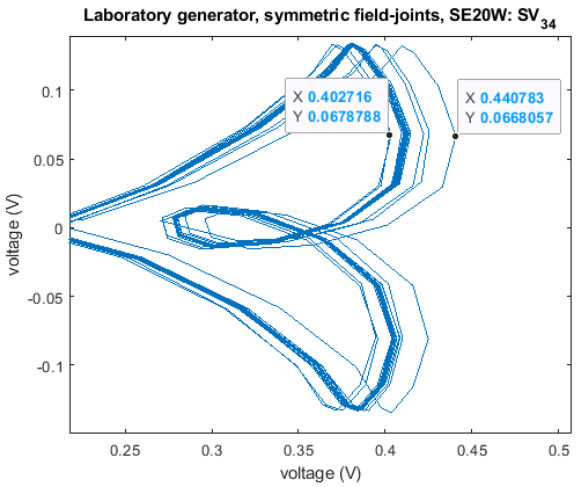

(b) Enlarged plot of space vector SV_{34} for the laboratory generator model with 20 % static eccentricity at 180° and symmetric field-joints.

Figure 8.4: Enlarged plots of space vector $SV_{3,4}$ for the laboratory generator model with 20 % static eccentricity at 180° and **(a)** no field-joints, and **(b)** symmetric field-joints. The healthy field-joints do not increase the dispersion in the cyclic space vector pattern.

The space vectors $SV_{1,3}$ in figure 5.19 and SV_{24} in figure 5.20, show a clear linear dependency for the generator model without field-joints and without static eccentricity, as the plot show simply a straight line along the left diagonal. This model is represented in subfigure **(a)** for both figures. Space vector $SV_{12,34}$, plotted in figure 5.21, is a linear combination of SV_{13} and $SV_{2,4}$, and has therefore the same property. This characteristic is due to these space vectors being constructed from stray flux voltages which are identical in shape, but opposite in phase.

When faults are added to these three space vectors, the symmetry condition which renders the space vector a straight diagonal line, fails. The pattern thus diverges into something with more dispersion and waves, while the original line pattern is still visible. For space vector $SV_{13,24}$, figure 5.21b display the space vector with 20 % static eccentricity and asymmetric loose field-joints, and figure 5.21d display it with 50 % static eccentricity. The figures deviate from the line pattern in the same way, and it is hard to distinguish how the faults are expressed without any further analysis.

Figure 5.22 introduces the final space vector, $SV_{13,24}$. This vector is unique; it is composed of the sum of voltages identical in shape and size but opposite in phase. As a result, under healthy conditions and without field-joints, it is expressed merely as a compact dot of noise. This scenario is illustrated in figure 5.22a, with the plot's limits set around 10^{-4} to properly display the graph. When a fault is introduced, for example 20 % static eccentricity at 45°, shown in figure 5.22c, plot area is enlarged by a factor of 100. When the fault severity is doubled to 40 %, the plot's height and width is approximately also doubled, although the plot maintains its original shape. This suggests that in the absence of asymmetry, space vector $SV_{13,24}$ is reduced to almost zero. However, the presence of asymmetric conditions gives the space vector a substantial existence.

When analyzing the results obtained with Method III, all plots were analyzed in their real scale. One of the observations was deviation from symmetry in the space vectors when asymmetric conditions were applied. Size and dispersion width variation during faults was another. This is a problematic fault tell, as the plot sizes differ between different generators. Measurements of a generator in healthy condition are rarely available, so there will not be plots to compare with. Some sort of normalization trending should therefore be performed on the space vectors. More advanced analyses could be performed by means of machine learning to detect patterns which are not as evidently obvious as the ones discussed in this section.

8.1.3 Method IV: Discussion of static eccentricity severity computation

Three approaches were suggested in order to determine the severity of a static eccentricity fault. The three approaches were each tested on ten models of the laboratory generator with only a static eccentricity fault, five models where it had both a static eccentricity fault and a field-joint fault and five models of the industrial generator model with different static eccentricity faults. The approaches were also tested on the laboratory generator model and industrial generator model in a healthy condition.

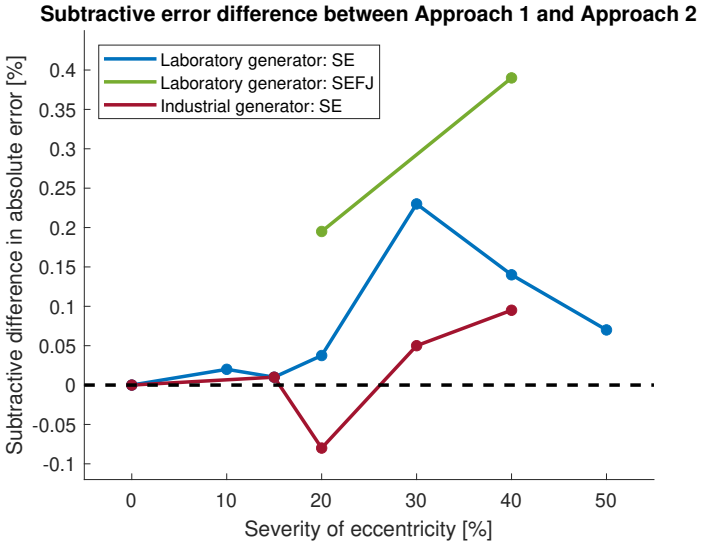

Figure 8.5: The absolute error subtractive difference in computed Static Eccentricity (SE) severity between Approach 1 and Approach 2. The differences are calculated as error of Approach 1 minus error of Approach 2, for the three model types. It can be observed that the absolute error difference between the two approaches is negligible.

The severities computed through Approach 1 and Approach 2 are largely similar, as seen in the result tables in section 5.4. Figure 8.5 visualizes the discrepancy, illustrating the error differences as a function of static eccentricity severity. The error difference is calculated as the average of all errors of Approach 1 minus error of Approach 2, at each severity. Figure 8.5 demonstrates that all values except one are positive. This indicates that Approach 2 has better accuracy than Approach 1. However, the figure also demonstrates a maximum difference of around 0.4 % between the two approaches, which is an insignificant value. While Approach 2 yields marginally better results,

Approach 1 may provide greater reliability as it is uses an average value based on all four sensors. In a real generator, it may not be possible to install sensors exactly 90° apart, and an average based on all four sensors is therefore more stable than two averages based on two and two sensors.

Figure 8.6 represents the absolute error for all three model types - laboratory generator models with Static Eccentricity (SE) or with Static Eccentricity and Field-joints (SEFJ), and the industrial generator models, which solely exhibit static eccentricity. The absolute error from Approach 1 is presented in figure 8.6a, and from Approach 3 in figure 8.6b. Solid lines depicts the best fit linear line corresponding to the error points of each model type. It was computed using the MATLAB function *polyfit*, which applies the method of least squares to find polynomial coefficients, with a linear fit found to be adequate in this case.

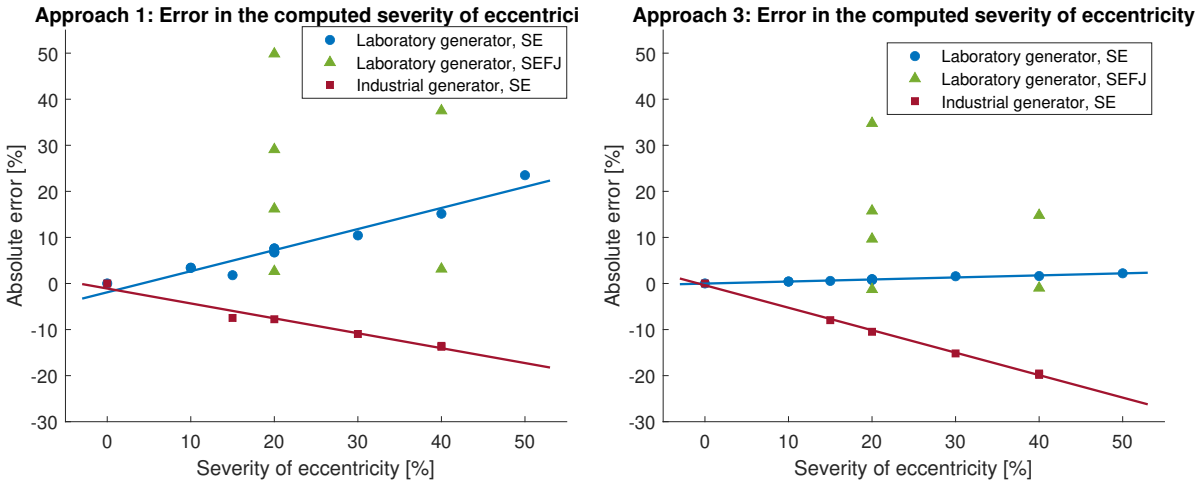

(a) Absolute error in static eccentricity severity, computed by Approach 1.

(b) Absolute error in static eccentricity severity, computed by Approach 3.

Figure 8.6: Absolute error in static eccentricity severity computed by **(a)** Approach 1 and **(b)** Approach 3, for the laboratory generator with Static Eccentricity (SE), and with Static Eccentricity and Field-joints (SEFJ) and the industrial generator models. The solid lines are best fit lines, computed by the method of least squares, for the model type of the same color. The absolute errors for the SEFJ-models are too dispersed to compute a best fit line.

The best fit lines in figure 8.6a demonstrate an increase in absolute error with increasing severity, for both the laboratory and the industrial generator models. In figure 8.6b, the industrial generator models demonstrate the same trend, while the absolute error is almost stagnant for the laboratory generator models. Consequently, Approach 1 appears more accurate for the industrial generator models, while Approach 3 yields higher accuracy for the laboratory generator models. Additionally, the computed severity consistently overestimate the actual severity for the laboratory generator models, while it is underestimated for the industrial generator models. Given these findings, determining a superior method for calculating the severity of static eccentricity is challenging. In fact, it is questionable whether any of them hold any value at all. If a field test is carried out on an arbitrary generator, and the static eccentricity severity is computed to be 30 %, with potential true values ranging from 10 % to 50 %, supplementary testing must anyway be performed. Nevertheless, both the approaches could arguable still be used to demonstrate the

presence of static eccentricity, which would be a significant first step to determine the severity.

Figure 8.6 excludes best fit lines for the laboratory generator models with SEFJ-fault. This is because the error dispersion was considered too large, and because the field-joint width-variation should also be considered when analyzing these models. Among the four SEFJ-models with 20 % severity, the absolute error ranged from 2.6 % to 49.9 % for Approach 1, and from -1 % to 34.8 % for Approach 3. In comparison, for the four laboratory generator models also exhibiting 20 % static eccentricity, the absolute error ranged from 6.7 % to 7.6 % for Approach 1, and from 0.8 % to 1 % for Approach 3. As the only difference between these laboratory generator models is the addition and variation of field-joints, this result indicates that the field-joints have a major impact on the approaches proposed here to compute the static eccentricity severity. It also indicates that the effect from a field-joint fault is considerably larger than the effect from static eccentricity.

8.1.4 Method V: Discussion of static eccentricity angle computation

This subsection discusses the results obtained in section 5.5 of chapter 5: Pattern recognition results on simulated models. The section proposed a method to determine the angle of a static eccentricity fault by means of time-series data mining and the radius of gyration of the sensor voltages. Figure 8.7 illustrates a stator, with the ten sensor positions marked. A protractor has been added to the illustration, to clarify in which direction a static eccentricity reacts. The cardinal directions east, north, west, south, northeast, northwest, southwest and southeast are also added, to further explain the naming of the static eccentricity generator models.

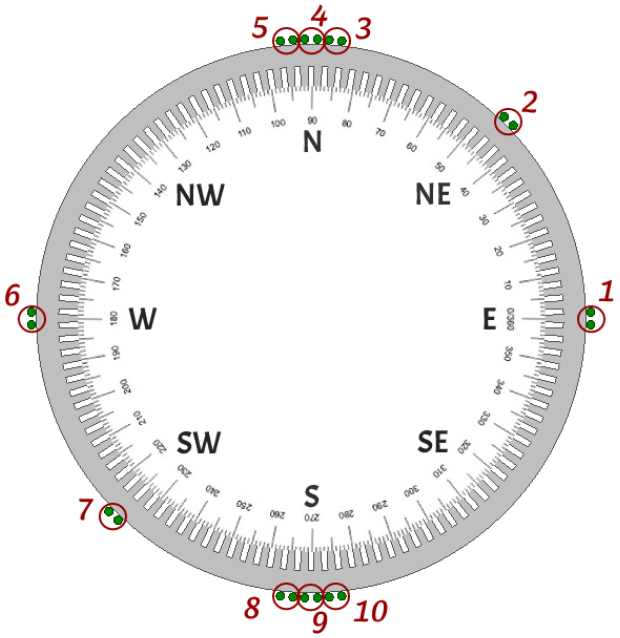

Figure 8.7: Illustration of a stator with ten stray flux sensors. The protractor explains the mechanical degree references in this thesis. Eight cardinal directions clarify the naming of the generator models.

Figure 8.8 visualizes the absolute error in the static eccentricity angle computations, for all the generator models. In figure 8.8a, the absolute error is plotted against the angle of eccentricity.

In figure 8.8b, the same error is plotted against the severity of the static eccentricity. In both figures, the blue circles represent the laboratory generator model with a static eccentricity fault, the green triangles represent the laboratory generator models with both static eccentricity and field-joint fault, and the red squares represent the industrial generator models. The healthy-case models are not included in figure 8.8a, as they would not make sense on the x-axis.

The solid lines in both subfigures in 8.8 represent linear trends. Trend lines for the laboratory generator with SEFJ-fault were not computed, as the results were too dispersed to display a clear linear trend. This is further discussed in subsection 8.1.5. In figure 8.8a, the trend line for the industrial generator appears constant, while the laboratory generator appears to decrease with an increasing angle. Due to the computation method, the angle of eccentricity should not affect the results and a flat line was therefore expected. A plausible reason for the decrease is the sample variation, as more models were included with a small angle than a large angle. The trend line computed by method of least squares is therefore influenced by outliers. In figure 8.8b, the trend line for the laboratory generator appear constant, and of the same values as in 8.8a. This is a more surprising result, as an increase in severity tends to affect the induced sensor voltages, assumingly increasing the absolute error. The trend line for the industrial generator decreases with higher SE severity, which again is assumed to be caused by the sample distribution. The results indicate that the computation method is robust against severity variations, in the models without field-joints. However, more simulations should be computed with the industrial generator especially, but also the laboratory generator, to verify this.

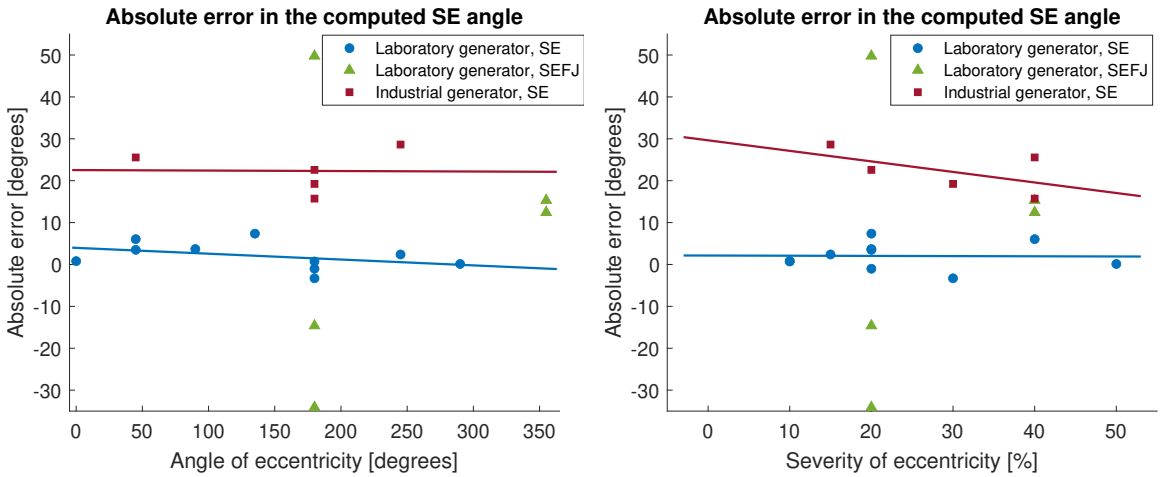

(a) Absolute error, in mechanical degrees°, of the computed SE angle for the simulated models, as a function of the models' actual SE angle position.

(b) Absolute error, in mechanical degrees°, of the computed SE angle for the simulated models, as a function of the models' severity of eccentricity.

Figure 8.8: Absolute error in the computed Static Eccentricity (SE) angular position for the simulated models exhibiting solely SE or both SE and Field-Joint (SEFJ) fault, as a function of **(a)** the model's SE angle and **(b)** the model's SE severity. The solid lines represent linear trend lines.

For the laboratory generator with static eccentricity fault, represented as blue circles in figure 8.8, the maximum error is 7.4° and the minimum error is -3.3°. This minor error would not impact finding the location of the static eccentricity. The absolute errors are greatest for the the

laboratory generator models with both static eccentricity and field-joint fault, with a maximum error of 49.8°. The values are dispersed and do not display an obvious pattern. As these models are identical to laboratory generator models exhibiting only static eccentricity fault, except for the addition of field-joints, this indicates that field-joints affect the computation method more than does a static eccentricity fault. The industrial generator models have absolute error ranging from 15.7° to 28.6°. A reason for the overestimation could be the greater radius of the industrial generator compared to the laboratory generator, as the sensors are positioned further apart and are thus further from the static eccentricity than for the laboratory generator.

In figure 8.9, the computed Radii of Gyration (RoG) are displayed for the sensors 1, 4, 6 and 9. The sensor positions can be reviewed in figure 8.7. A selection of the laboratory generator models with Static Eccentricity (SE) fault are presented in figure 8.9a, while the industrial generator models are presented in figure 8.9b. Both figures clearly show how the RoG's variation in the healthy case models compared to the models with static eccentricity. The RoG increases in sensors close to the static eccentricity, and in sensors far from it, the RoG decreases.

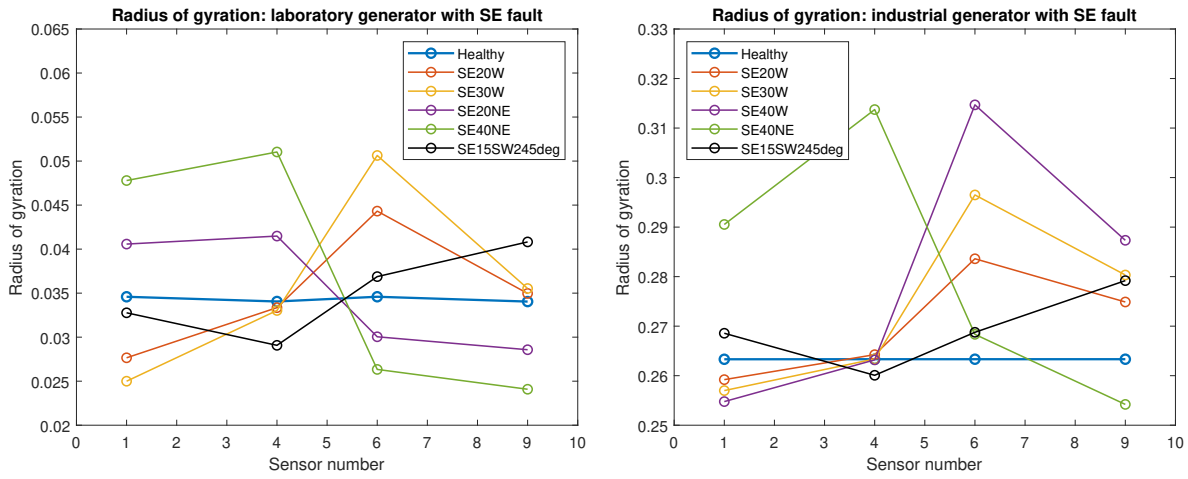

(a) Computed RoG for some of the laboratory generator models with SE fault.

(b) Computed RoG for the industrial generator models with SE fault.

Figure 8.9: Computed Radius of Gyration (RoG) for **(a)** selected models of the laboratory generator models with Static Eccentricity (SE) fault and **(b)** the industrial generator models.

The maximum and minimum computed radius of gyration can be used to find the quadrant in which there is a static eccentricity fault. Four sensors (named 1, 4, 6 and 9 for consistency) were utilized to measure the stray magnetic flux, located 90° apart. The cross-section of the generator is divided into four quadrants (named QI, QII, QIII and QIV), as in figure 4.1. Then, Sensor 1 and Sensor 4 mark the beginning and end of QI, Sensor 4 and 9 mark the beginning and end of QII, and so forth. For the models with an SE fault in figures 8.9a and 8.9b, the two largest computed RoG were computed at the sensors which enclose the quadrant in which is the angle of the static eccentricity. This agrees with the theory, as the reduced magnetic reluctance on the smaller air gap side lead to higher induced sensor voltages and thus a higher computed radius of gyration as of equation (4.8).

8.1.5 Simulations of combined static eccentricity and field-joints

The simulated models with combined static eccentricity and field-joint fault demonstrated larger and more dispersed errors than the models with only field-joint fault, as has briefly been established in the previous subsections. These models varied in two factors, namely static eccentricity and field-joint widths, and comparisons of their results are therefore performed separately from the models with only static eccentricity fault. Only models of the laboratory generator were equipped with field-joints, and therefore no industrial generator models are considered here. A total of six different models exhibiting both Static Eccentricity and Field-Joint (SEFJ) fault were simulated. They were presented in table 3.5. This is a rather small sample size, but as much time was devoted to static eccentricity as an isolated fault, less time was correspondingly allocated for the SEFJ fault models. The possibility to draw conclusions is therefore limited.

The computed results for the static eccentricity severity see significant difference in the models with healthy, symmetric field-joints compared to the models with faulty, asymmetric field-joints. The two models with healthy field-joints, namely SE20W SYM and SE40SE355deg SYM, have minor absolute errors of -1.2 % and -1 %, respectively. Among the four models with faulty field-joints, the minimum absolute error is 9.7 % and the maximum error is 34.8 %. The severities are computed by means of Approach 3, defined in subsection 4.4.3. These results indicate that Method IV: Computation of static eccentricity severity is robust to influence on the stray flux from field-joints. However, it must not be disregarded that on these models the real angular position of the static eccentricity is far from the location of the field-joint. If it was closer, there is still a probability that healthy field-joints could affect the severity computations.

Method V, computation of static eccentricity angle, appears more affected by the field-joints than Method IV, which computes the severity. The absolute errors from Method V are plotted for the SEFJ-models in figure 8.8. Of all simulated models, those with SEFJ faults have the maximum and minimum errors, of values 49.8° and -34.1°. Interestingly, the two models exhibiting 40 % eccentricity at 355° have approximately the same error, despite the fact that one has healthy and one has faulty field-joints. In contrast, all models with 20 % eccentricity at 180° have larger errors, even though the two locations at 180° and 355° are approximately equidistant from the field-joints. This indicates that the method is influenced by the presence of field-joints, regardless of whether they are healthy or faulty.

Figure 8.8 does not include the model SE20N ASYM TIGHT, due to its exceptionally large absolute error of 131.05°. The significant deviation is a result of the method's failure to identify the correct quadrant for this model. As the actual angle is 90°, either QI or QII should have been identified as the correct quadrant. However, the two largest radii of gyration were computed at sensors 6 and 9, establishing the angular position in the third quadrant, $QIII$. This model differed from the others as its static eccentricity was positioned directly on a field-joint. In a real generator, it could be argued that this concurrence is improbable. The model is the only case in which the method for computation of the static eccentricity angle did not recognize the correct quadrant. This indicates the method's robustness in identifying the correct angle, unless

the position of static eccentricity and a field-joint coincide. Additionally, it is another argument that field-joints affect the stray flux more than static eccentricity does.

Simulations show that presence of static eccentricity does not affect the detection of faulty field-joints. This is demonstrated in figures 8.10 and 8.11, which represent two laboratory generator models exhibiting 40 % static eccentricity at 355°, but with different field-joints. In both figures, voltages are plotted for sensors 3 & 5 in figure **(a)**, and for sensors 8 & 10 in figure **(b)**. The sensor pairs are located near the top field-joint and the bottom field-joint, respectively. In figure 8.10, the field-joints are healthy. It can be observed that the shapes and amplitudes of the voltages are equal, as would also have been expected in an identical model without static eccentricity. In figure 8.11, the bottom field-joint is larger than the top field-joint. As expected, the larger amplitude is observed at the larger field-joint, and the smaller amplitude at the smaller field-joint. Based on this, the field-joints can correctly be identified as faulty, which would also be the conclusion in a generator model with the same field-joint fault but without the static eccentricity.

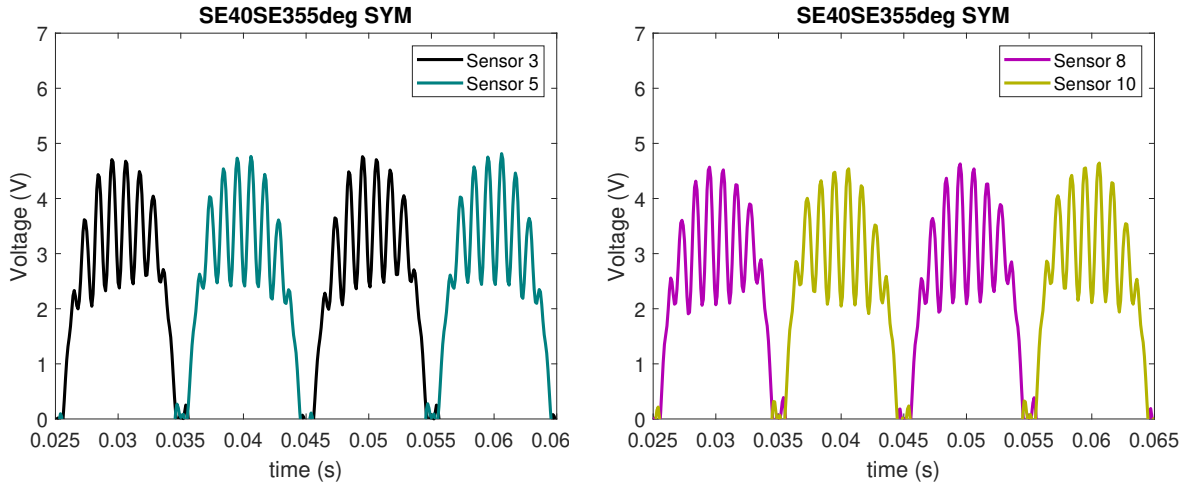

(a) Voltages in Sensors 3 & 5, which are located close to the top field-joint.

(b) Voltages in Sensors 8 & 10, which are located close to the bottom field-joint.

Figure 8.10: Comparison of the simulated voltages for the laboratory generator model with 40 % static eccentricity at 355° and symmetric field-joints for **(a)** sensors 3 & 5, and **(b)** sensors 8 & 10.

Another deduction made from figures 8.10 and 8.11, is that the presence of static eccentricity does not modify the voltages induced in the sensors on either side of a single field-joint. This observation is in line with expectations, as the fringing flux in the generator model simulations is conserved. It exits the stator yoke on one side of the field-joint and re-enters on the opposite side. Despite this, the introduction of static eccentricity causes some imbalance in the flux distribution, which could theoretically contribute to the sensor voltages on one side of a field-joint. Nevertheless, it appears that the influence from the fringing flux surpasses the influence from the static eccentricity, to such an extent that this is not observable in the simulated models.

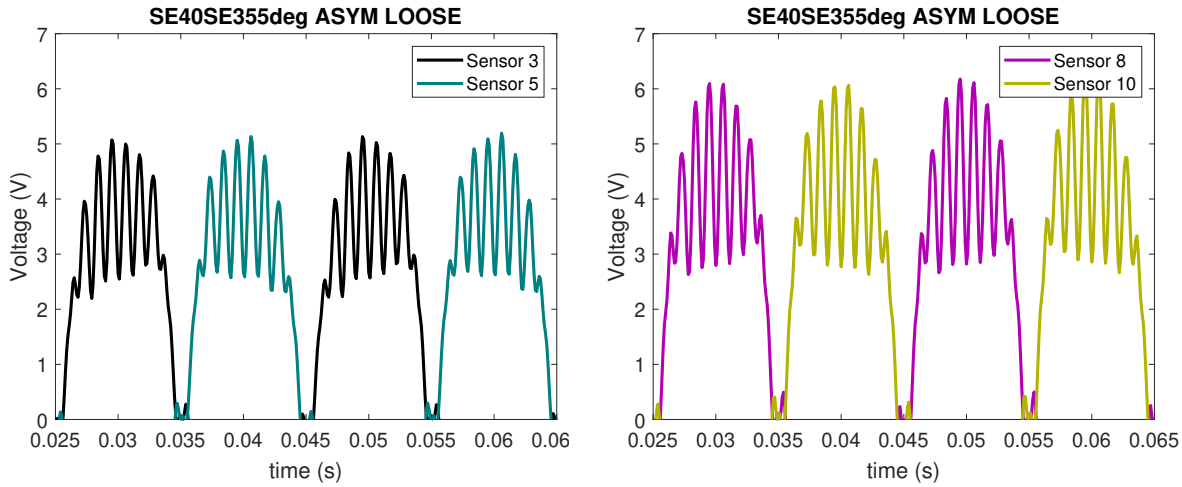

(a) Voltages in Sensors 3 & 5, which are located close to the top field-joint.

(b) Voltages in Sensors 8 & 10, which are located close to the bottom field-joint.

Figure 8.11: Comparison of the simulated voltages for the laboratory generator model with 40 % static eccentricity at 355° and asymmetric loose field-joints for **(a)** sensors 3 & 5, and **(b)** sensors 8 & 10.

8.2 Discussion of stray flux test on field-joints

In chapter 6: Stray flux test on field-joints in a synchronous generator, the results from a stray flux test, performed on a synchronous hydroelectric generator with two field-joints, were presented. The field-joints had previously been assessed with the conclusion that they were asymmetric and loose. Two load conditions, one with no load and one with a small load, were applied, and three sensors were installed on each field-joint. The field-joints were located on opposite sides of the generator, 180° mech apart.

In the preproject [2], stray flux variation related to field-joints was investigated. Stray flux sensor voltages were simulated in several healthy and faulty field-joint cases, and with various sensor positions. The results from the preproject have been presented in section 4.1. In summary, it was found that one sensor on each side of the field-joint, on every field-joint, was necessary to be able to determine field-joint fault in a 2D cross-sectional plane. No 3D models were considered during the preproject work.

During the work with stray flux analysis at NTNU, this field test was the first time the stray flux was measured on a field-joint [23]. There was therefore some uncertainty as to what the test results should look like. However, in the preproject it was found that different amplitudes and RMS voltages indicate a variation in the field-joint width. The RMS voltages from each sensor, each field-joint and each load case are presented in table 6.1. The RMS values are also visualized in figure 8.12, with the no load-cases in figure 8.12a and partial load cases in figure 8.12b. It can immediately be observed that the top sensors recorded the highest voltages for both load cases and field-joints. The voltage at the top sensors increases from no load-case to partial load case. The other voltages decrease slightly from no load to loaded case. The voltages at the bottom field-joint are approximately equal during partial loading.

During the preproject, it was concluded that one sensor should be installed on each side of a field-joint to detect field-joint fault. In the simulations, the sensors directly on top of the field-joint caught only a minimal amount of fringing flux, and thus scarcely any increase in voltage amplitude, compared to the sensors on the sides. By side of field-joint is meant approximately 5° mechanical to each side of the field-joint. Due to the larger size of the real sensor and the support struts on the sides of the field-joint, there was only room to install one sensor directly on top of the field-joint. However, due to the area of the real sensor, around 10 cm^2, compared to the small width of the field-joint of approximately 0.1 mm, it was assumed that the sensor would still capture fringing flux. As can be observed on figure 8.12, different voltage values were registered at all sensors. This indicates that the assumption was correct.

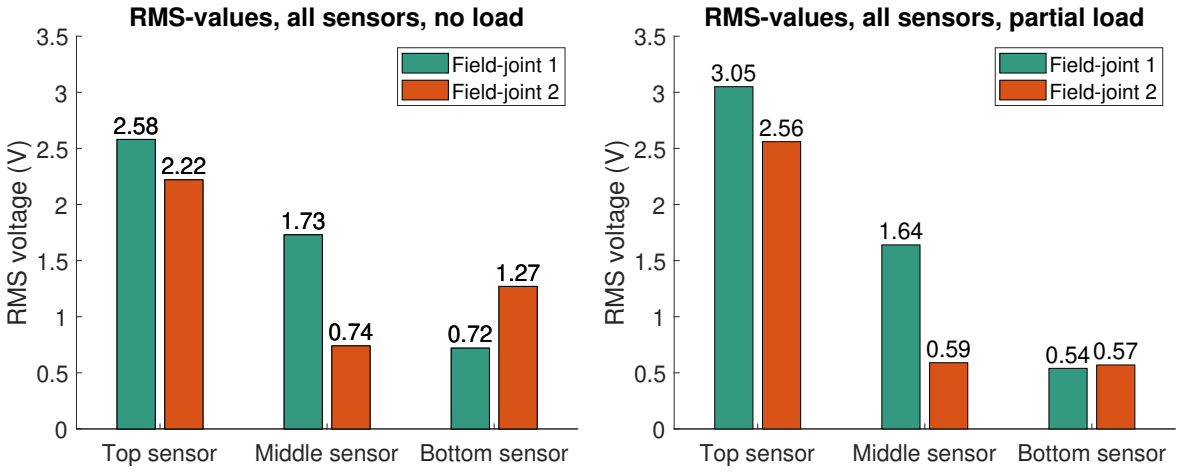

(a) RMS voltages of all the sensors installed during the field test, in the no load-case.

(b) RMS voltages of all the sensors installed during the field test, in the partial load case.

Figure 8.12: Bar graph-representation of the RMS voltages measured in the sensors installed on two field-joints during the field test, in **(a)** the no load-case and **(b)** the partial load case.

According to conclusions from the preproject [2], discrepancies in RMS voltages from sensors situated on the same vertical level should signify field-joint fault. In the no load-situation, table 6.1 presents a difference of 0.4 V between the top sensors, 1 V between the middle sensors and 0.55 V between the bottom sensors. These variances suggest that the most significant field-joint fault occurs at the middle sensors. Nonetheless, the generator used in this field test may have other, unexplored faults in addition to the field-joints, and these may manifest differently. Based solely on visual inspection of the voltages presented in figures 6.3 and 6.4, there is more harmonic disturbance in some measurements compared to others. This could be a fault indication, or it could be due to disturbances from sensors or the generator. Consequently, without comprehensive analysis and understanding of potential other faults, diagnosing the field-joint fault from the results of this field test is a challenging task.

Prior to the field test, no investigations had been carried out on 3D models of field-joints. Consequently, the voltage measurements in the vertically placed sensors provided new insights. Figure 8.12 visualizes a trend were the highest voltages were measured by the topmost sensors, median

voltages were recorded by the middle sensors and lowest voltages were recorded by the bottom-most sensors. Additionally, only no load-cases had been explored in the simulations. Compliant with the results from chapter 7: Stray flux test on static eccentricity in two generators, and the consequent discussion in section 8.3, the load changes did not have major impact. This can be observed in figure 8.12. The exception is the bottom sensor at field-joint 2, which is decreased by 0.7 V.

An interesting aspect of the measured voltages, is the phase shift that occurs in the sensors installed at the top compared to those at the middle and bottom, as depicted in figures 6.3 and 6.4. The induced voltages in the top sensors appear to be shifted approximately 180 electrical degrees from the others. This was unexpected, as it is not possible for the magnetic flux to flow in one direction at the top part of the stator core, and the opposite direction in the middle and the bottom part. A potential explanation is that the top sensors were wound in the opposite direction, which would induce voltages of an opposite phase.

8.3 Discussion of stray flux test for static eccentricity

In chapter 7: Stray flux test on static eccentricity in two generators, the pattern recognition results from the stray flux sensor voltages measured on two generators were presented. The voltages had been recorded some years earlier in relation with the PhD dissertation in [4]. The generators were named Generator 1 and Generator 2.

Different load cases were investigated during the generator field tests. For both generators, a no load test was conducted. For Generator 1, one additional case with partial load was carried out, while one partial load case and two full load cases were done for Generator 2. The results presented in chapter 7 are summarized in table 8.2 for the reader's convenience. In the table, the calculated severity and angle is presented for each load case for each generator.

One can in table 8.2 immediately notice that the calculated severity in Generator 1 is very large, approximately 80 %. This would mean that the rotor has moved almost the distance of one air gap length and therefore nearly touches the stator, which is impossible during generator operation. Indeed, even a severity of more than 50 %, would cause the vibrations related to the eccentricity to have increased to an unacceptable strength [23]. As this was not the case during the field test of any of the generators, there is the probability that the calculated severities are inaccurate.

Table 8.2: Computed severity and angle of the static eccentricity in Generator 1 and Generator 2.

Generator 1 & 2: results summary			
Generator	**Load status**	**Severity** [%]	**Angle** [degrees°]
Generator 1	No load	83.98	310.63
	Half load	75.74	306.13
Generator 2	No load	41.87	146.38
	Half load	42.80	144.74
	Full load 1	42.25	145.37
	Full load 2	40.05	142.58

The computed severity and angle of the static eccentricity have some small variations as a consequence of the load change. For Generator 1, a decrease of 8 % was recorded when the load was adjusted from no load to half load. For Generator 2, severity increased by 1 % and 0.5 % respectively from no load to half load, and to Full load 1. It decreased by almost 2 % to Full load 2. Due to the generators' parallel windings, the computed eccentricity should have decreased during the load increase. This is because a larger load cause a smaller synchronous reactance on the smaller air gap side [21]. The small synchronous reactance pull a larger stator current, which to a higher extent has a counteracting force pushing the rotor away from the stator, decreasing the severity of the static eccentricity. The fact that this result was not achieved during the analysis could have several reasons. One of them could be the positioning of the sensors during the field tests. Alternatively, the reliability of the computational method could also be questioned.

Neither the severity nor the angle of the static eccentricity are much changed in the different load cases for the two generators. The angle computed for Generator 1 varies with 4.5° and for Generator 2 it varies with 3.8°. This variation is assumed to stem from unreliability of the method. However, as a hydroelectric generator typically has a diameter of several meters, the variation has no consequences in practice. The severity for Generator 1 varies with 8.24 %, and for Generator 2 it varies with 2.75 % from the case with the largest to the smallest severity. Again, this variation has little significance. Therefore, based on the results presented in this thesis, the methods proposed to compute the angle and severity of a static eccentricity fault is not affected by different load cases.

8.4 General discussion points

Most of the research conducted during the work with this Master's thesis has been performed on computer simulated models in ideal conditions. Both the models of the laboratory generator and the industrial generator are based on real synchronous generators, but complexities inherent in real-world situations have not been added. For example, the generator models are not impacted

by deterioration due to aging or externalities, like corrosion effects, increased vibrations, increased losses, insulation degradation or something entirely different. Electrical, mechanical or thermal stresses could influence the stray magnetic field, and alter the magnetic sensor induction from what would be measured in an ideal case. Additionally, there are integral parts of the generator construction which are not included in the very simple generator models. They include, but are not constricted to, an outer protection shell, support beams, ventilation and cooling systems, ventilation ducts and clamping bolts. Deviations from ideality contribute to noise in the sensor measurements, and discrepancy from simulation results.

All simulations have been performed with two-dimensional models. This implies that axial conditions have been assumed constant and end conditions have been ignored. During the field test, sensors were installed at three vertical locations on each of the two field-joints. The measurements demonstrated that the induced voltages were different at each of the heights. With regards to a 2D model, this was unsuspected and could imply serious fault. However, considerations can be made with regards to the generator's physical structure. The lowest sensors are located the closest to the floor, and thus also the bearing, ground support, shaft and rotor spider. These conditions increase the noise levels in the induced sensor voltage. The top sensors, on the other hand, are closer to the upper deck, upper spider and held bearing, which also cause noise. Some variation in the induced voltages along the vertical axis of the generator is therefore expected and does not necessarily imply a generator fault. However, a misalignment fault would imply a physical variation in the axial direction, which would also be expressed as a difference between the sensors at different heights. The variations have not been covered in this thesis, and more analyses are required in order to determine what type of fault or noise contributor cause a field-joint voltage variation along the axial direction of a generator.

Many of the fault indications discovered through analysis of the stray flux sensor voltages, would easily be distinguishable from a healthy generator if only measurements of the healthy case was available. Unfortunately, fault measurements are rarely performed when a fault or suspicion of a fault is not present. Upon reflection, this is reasonable because generator surveillance incurs financial and temporal expenditures. Additionally, the stray flux technique employed is rather novel, and as generator faults may take years to develop, the method may actually not have been available when the generator was still healthy. However, to an inexperienced student, initially this was not obvious. In fact, during the first part of the thesis work, it was assumed that some information about the healthy case would be available. Later it was discovered that the developed fault detection methods could not relay on comparison with a healthy case.

Figures 8.13 and 8.14 show the radial component of the magnetic flux density in, respectively, the air gap and in the sensors, for both the laboratory generator and the industrial generator. The flux densities are plotted around the circumference of the generators. It can be observed that the stray magnetic flux density through the sensors, in figure 8.14, is a representation of the air gap magnetic flux density of smaller magnitude and less detail. At both locations - in the air gap and in the sensors - the presence of seven magnetic periods in the laboratory generator

and eight magnetic periods in the industrial generator are discernible. These figures are included to demonstrate the utility of stray flux analysis as a diagnosis tool, providing evidence of the congruity of information contained within the stray magnetic field and the air gap magnetic field.

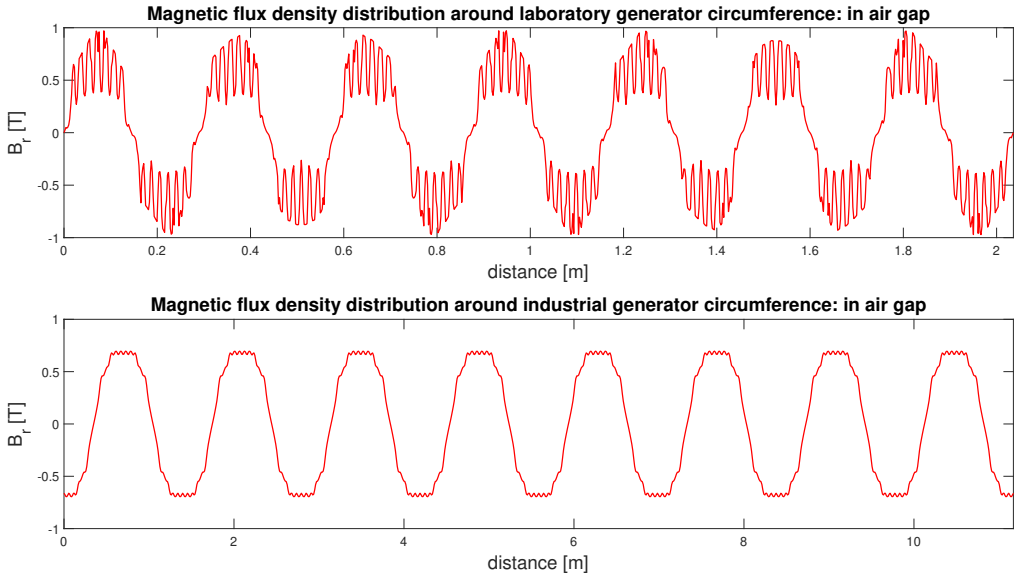

Figure 8.13: Plot of the air gap magnetic flux density. For the laboratory generator model (top), seven magnetic periods can be observed. For the industrial generator model (bottom), eight periods can be observed.

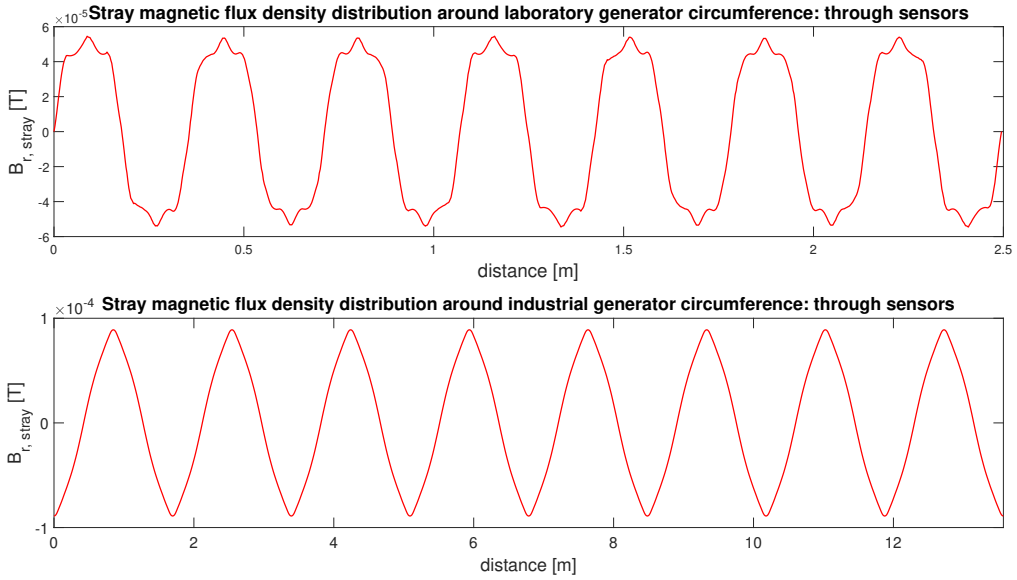

Figure 8.14: Plot of the stray magnetic flux density distribution in the sensors. For both the laboratory generator model (top) and the industrial generator model (bottom), the stray magnetic flux is an attenuated mirror of the air gap magnetic flux depicted in figure 8.13.

8.4.1 Considerations on the sensor positioning in static eccentricity calculations

In the static eccentricity simulations and computations performed in the Master work, the relative distance between each of the four sensors has always been assumed to be equal and equivalent to 90°. Therefore, all error estimates of the developed methods are based on a constant distance between the sensors, but this may not always be true. On a real generator, it may not be possible to install sensors at every desired position around the stator circumference. Obstacles like ventilation, cooling systems and support beams may block the access to the stator backside. If the core is also protected by an outer shell, as with the generator from chapter 6, access to the stator backside is only possible through hatches in the shell. The sensors must then be installed where the hatches are, which may not be at the desired locations. The deviation from equal circumferential distance between the sensors lowers the accuracy of the computation methods for static eccentricity fault.

The laboratory generator and industrial generator models were made with ten sensor located around the circumference, at different positions. The positions can be reviewed in figure 8.7. For the static eccentricity calculations presented in previous chapters, sensors 1, 4, 6 and 9 were employed, located equally 90° apart. To investigate the effect of unequal distance between the sensors, the calculations and errors were also computed with the sensors 1, 3, 6 and 8, and with the sensors 1, 2, 6 and 7. That gives a difference of 5° for the first group, and 45° for the second group. The results are presented in table 8.3 and table 8.4, respectively. The calculations were performed on laboratory generator models, and only by means of Approach 1. The equations used to compute the angle shares, equations (4.11a) and (4.11b), were altered to accommodate to the new quadrant angle sizes. That means that if the static eccentricity was found to be for example between sensors 6 and 7, the shares would be multiplied by 45° instead of the original 90°.

Table 8.3: Calculated severity and angle for six laboratory generator models with Static Eccentricity (SE) fault, computed from sensors 1, 3, 6 and 8.

Computation of SE severity and angle: Sensors 1, 3, 6, 8				
Model name	**Severity** [%]	**Error** [%]	**Angle** [degrees°]	**Error** [degrees°]
SE10E	14.26	4.26	8.05	8.05
SE20W	28.57	8.57	186.13	6.13
SE30W	42.80	12.80	183.39	3.39
SE40NE	56.53	16.53	50.82	5.82
SE15SW245deg	16.83	1.83	245.22	0.22
SE50SE290deg	70.61	20.61	287.58	-2.42

Table 8.4: Calculated severity and angle for six laboratory generator models with Static Eccentricity (SE) fault, computed from sensors 1, 2, 6 and 7.

Computation of SE severity and angle: Sensors 1, 2, 6, 7				
Model name	**Severity** [%]	**Error** [%]	**Angle** [degrees°]	**Error** [degrees°]
SE10E	19.23	9.23	14.68	14.68
SE20W	38.25	18.25	196.25	16.25
SE30W	57.31	27.31	196.44	16.44
SE40NE	55.79	15.79	29.17	-15.83
SE15SW245deg	12.79	-2.21	210.05	-34.95
SE50SE290deg	38.46	-11.54	311.85	21.85

The results in table 8.3 and table 8.4 show that, as expected, a deviation of the sensor position from the constant 90° angle has an effect on the computed static eccentricity severity and angle. The effect is visualized in figure 8.15. Figure 8.15a depicts the error of the computed static eccentricity severity for the selected models, and figure 8.15b show the error of the computed angle. In both subfigures, it can be observed that the largest absolute error occurs with the sensors 1, 2, 6 & 7. Of the three sensor groups in the figure, this is the one with the largest deviation from a constant 90°. The largest error is 27.3 % for the severity, and -35° for the angle. In a few computations this group has approximately equal or smaller error than the two other sensor groups.

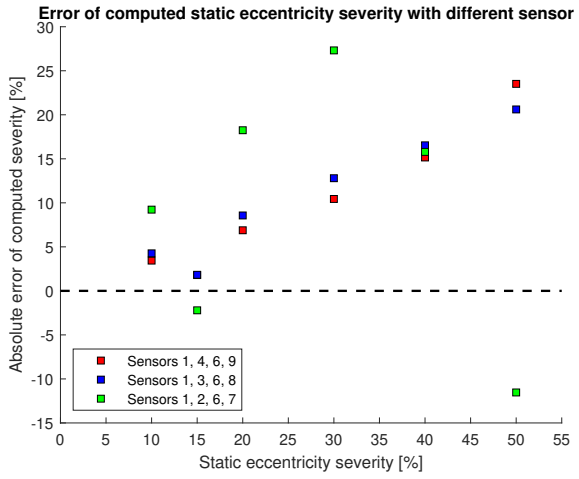

(a) Error of calculated SE severity, computed from three different sensor groups.

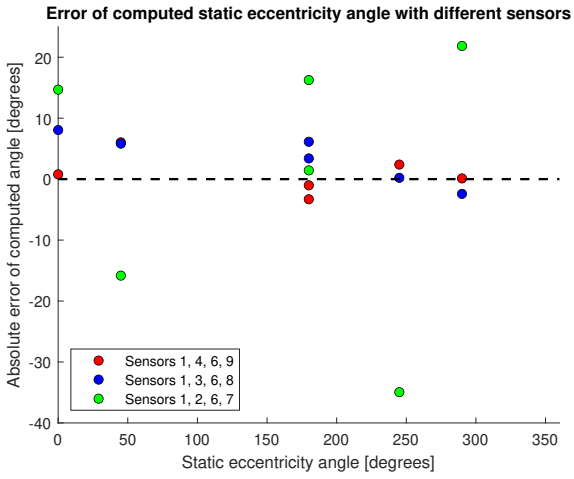

(b) Error of calculated SE angle, computed from three different sensor groups.

Figure 8.15: Error of calculated **(a)** severity, and **(b)** angle for a selection of laboratory generator models with Static Eccentricity (SE) fault, computed from three different sensor groups.

The absolute error differences between sensor groups 1, 4, 6 and 9, and 1, 3, 6 and 8 are in-

significant for both severity and angle, of only a few percent or degrees°. The largest error for these two groups are found at 50 % severity, with a difference of 2.9 %, and at 0°, with a 7.3° difference. This indicates that a sensor installed 5 % mech from its theoretical position, does cause unacceptable errors in the computed static eccentricity. These conclusions depend on the static eccentricity position being known, and that the new relative angles between the sensors are accounted for.

During the calculations of static eccentricity angle with different sensor positions, the actual sensor positions have always been assumed to be known. This means that the exact angles between the sensors are known, and accounted for when the angle shares are calculated. The quadrant sizes are thus changed to accommodate to the new angles. In reality, the angles may not be known exactly. Therefore, it was investigated how much the error changed if the angles between the sensors were assumed 90°, when in reality they were the angles of sensors 1, 3, 6 & 8 and sensors 1, 2, 6 & 7. The results are presented in table 8.5. They show that for sensors 1, 3, 6 & 8, where the difference to the true angle is only 5°, the change in computed angle is very small. At maximum, it is 3.84°, for model SE15SW245deg, and at for the model SE50SE290deg, the error is actually smaller. For sensors 1, 2, 6 & 7 on the other hand, the results are more ambiguous. For the model SE15SW245deg, the absolute error has decreased from 34.95° to 4.90°. For the other models, it is either unchanged or increased.

Table 8.5: Computed Static Eccentricity (SE) angle for six laboratory generator models with SE fault, based on sensors 1, 3, 6 & 8 and on sensors 1, 2, 6 & 7. The variation in quadrant size is not accounted for in the angle calculations.

Computation of SE angle: Unknown sensor positions				
Model name	Sensors 1, 3, 6 & 8		Sensors 1, 2, 6 & 7	
	Angle [degrees°]	**Error** [degrees°]	**Angle** [degrees°]	**Error** [degrees°]
SE10E	8.53	8.52	29.26	29.36
SE20W	186.49	6.49	212.50	32.50
SE30W	183.59	3.59	212.88	32.50
SE40NE	53.81	8.81	58.34	13.34
SE15SW245deg	249.05	4.05	240.10	-4.90
SE50SE290deg	291.39	1.39	327.90	37.90

In general, the discussion around the sensor locations has shown that the most accurate results are produced when the sensors are located exactly 90° from each other. If this is not possible, the increased error in the computed static eccentricity can be tolerated with a deviation of 5° in sensor location, so that the sensors are 85° and 95° apart. If the difference increases to 45°, the error also increases drastically. No calculations were made with two and two sensors not located on opposite sides of the generator, 180° mech apart.

8.5 Presentation of an algorithm to detect field-joint fault and static eccentricity

Based on the obtained results, analyses and discussion points presented in this thesis, an algorithm has been developed to detect and diagnose field-joint fault and static eccentricity. It is presented as a flow chart in figure 8.16. The algorithm uses color coding: red signifies a potential fault, green signifies absence of fault, yellow relates to tasks to be performed, and blue pertains to questions. Additionally, the question boxes are distinguished by their parallelogram shape.

The flow chart depicts the suggested line of action to determine whether a synchronous generator suffers from field-joint fault or static eccentricity, or possibly both. Prior to conducting a stray flux field test, the presence of field-joints in the generator must be established. If there are none, the field test may be performed utilizing four sensors spaced approximately 90° mechanical difference around the stator circumference, as close as possible to the stator backside, and at the same vertical level. If the generator does have field-joints, sensors must also be installed on every field-joint. The initial four sensors should be positioned as far from the field-joints as possible, while still maintaining their relative distance of 90° spacing around the generator. This should minimize the effect from the field-joints' fringing field, which may disturb the computation of static eccentricity. This is especially important if the field-joints are faulty, as their influence on the stray magnetic field in this case may be significant.

Upon completing the field test, data analyses may be initiated. Firstly, a frequency analysis should be performed on the measured sensor voltages to exclude other types of faults typical for a synchronous generator. Certain increased harmonics may be a clear indication of a dynamic fault. As none of the simulated models tested in this thesis exhibit dynamic faults, how they affect the developed methods is uncertain. Based on this research, or lack thereof, it can therefore not be advised to continue with the proposed line of action in this case. If an FFT does not indicate unexpected harmonics, however, either field-joints or static eccentricity, or both, may be attributed to the generator behaviour, and the diagnosis operation may continue.

If the generator has field-joints, comparison of the voltage amplitude and shape from the sensor on each field-joint is necessary. If the voltages are approximately identical, the field-joints can be assumed healthy. If there is a difference between the voltage waveforms, the field-joints may be faulty. In either case, the static eccentricity attributes may be computed as the next and final step. However, simulation results indicate a higher possibility of success for the severity in the case of healthy than faulty field-joints. The computation of the angular position may be affected, and must be scrutinized for their precision, regardless of the field-joint state.

In the absence of field-joints, the severity and angle of an eventual static eccentricity fault may be computed with greater precision than in a field-joint case. However, obtained results should still be critically examined for their accuracy and validity, particularly those related to severity computations.

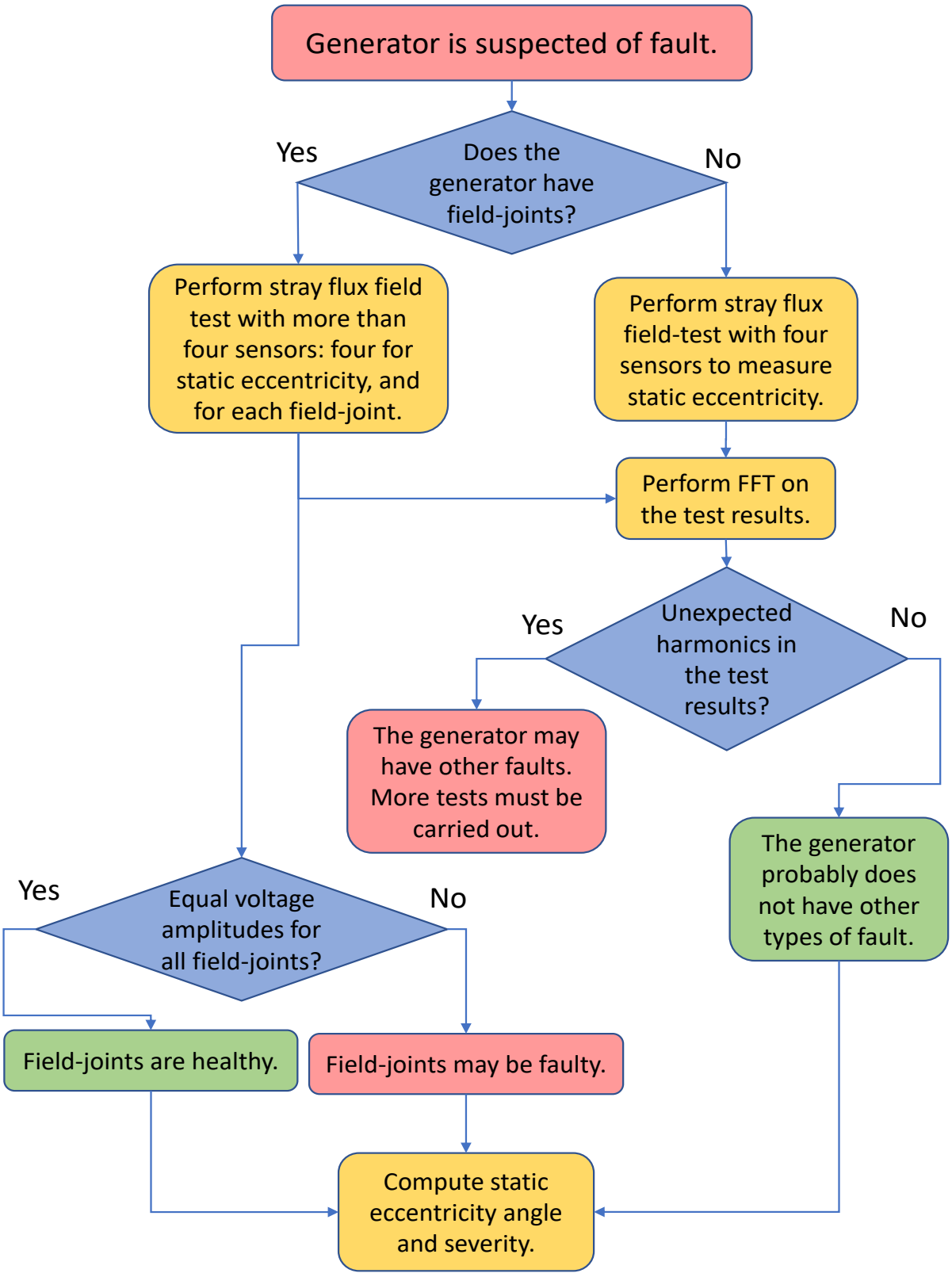

Figure 8.16: Flow chart presenting the algorithm suggested to detect and diagnose field-joint fault and static eccentricity, and distinguish them from other synchronous generator faults.

8.6 Future work

Building upon the findings gained from this Master's research, there are several potential directions for future investigations. They can further enhance the understanding of health diagnosis of electric generators, particularly salient-pole synchronous generators. In the following bullet points, some suggestions are listed as possible next steps:

- The methods introduced in this thesis for severity and angle computation of static eccentricity, need refinement to reduce their error. This is especially relevant to the severity calculations. The methods developed in this work were in major part based on empiricism, which the findings from this thesis indicate do not hold a sufficient level of detail. A better strategy could therefore be to base the methods on numerical calculations of the magnetic field.

- A more precise method should be developed to differentiate between static eccentricity and field-joint fault. The simulation results demonstrated that faulty field-joints significantly distort the static eccentricity calculations, rendering them virtually ineffective. Given this method limitation, it may be challenging to detect static eccentricity at all in a generator suffering from a severe field-joint fault.

- The research undertaken in this thesis could be expanded from salient-pole synchronous generators to other electrical machine types. Field-joints are characteristic in machines with large stators, and thus are not always present. Conversely, static eccentricity is more prevalent, and its fault signature in the stray magnetic field for other types of electrical machines could offer interesting insights. Such a study could further contribute to the evolution of stray flux analysis as a tool for health diagnosis of these systems.

- Some of the results, particularly the space vector results, could benefit from an examination with machine learning tools. These rapidly emerging systems would be able to detect pattern-based faults both faster and with higher accuracy than human capabilities. This task should preferably be performed by someone with more knowledge on the subject than the author of this thesis.

- The first field test investigating field-joints with stray magnetic flux was conducted during this project. The results were ambiguous, with their root cause proving difficult to determine. Whether they were due to field-joints or other faults remain uncertain. More tests and analyses should be performed on both healthy and faulty field-joints, to establish a baseline or "norm". This process would also help determine if the observed voltages were typical outcomes or a direct consequence of the fault.

Chapter 9

Conclusions

This final chapter contains a summary of the most important findings and conclusions drawn in chapter 8: Discussion of results, along with a review of the work process.

In this Master's thesis, detection and diagnostic strategies for static eccentricity and field-joint faults have been investigated through an analysis of the stray magnetic field in salient-pole synchronous generators. Primarily, the strategies have been scrutinized using simulated models of two generators, exhibiting either one or a combination of the two faults. The generator models are named the laboratory generator model and the industrial generator model. In addition, analyses were performed on voltage data from real-life field tests, where one focused on field-joints, and two on static eccentricity.

Five distinct methods for pattern recognition and fault diagnosis, based on voltage data from stray flux sensors, have been proposed in this thesis. The first method, Method I, explains identification of faulty field-joints based on a comparison of the amplitude and shape of voltages, from sensors installed on or near the field-joints. This method was carried over from the Master preproject.

Method II builds upon Method I by also incorporating models exhibiting both static eccentricity and a combination of static eccentricity and field-joint fault, in the voltage comparisons. Simulation results showed that static eccentricity does not impair the ability to detect faulty field-joints. However, the application of Method II to real-world stray flux data, derived from suspected faulty field-joints, proved a challenge. The observed voltages did not show the expected variations, which is assumed to be caused by faults or asymmetries not addressed in this thesis.

Method III recommended the construction of different voltage vector representations, from four stray flux sensors. The vectors were named space vectors. Their configuration yielded distinct patterns that demonstrated high symmetry in a healthy scenario, and various degrees of asymmetry in faulty scenarios. The pattern disorder appeared to increase with higher fault severity. Despite the evident distinction in space vector patterns, the level of fault disorder was challenging to quantify. Therefore, Method III did not prove immediately useful. For enhanced pattern analysis, machine learning tools were recommended for future studies.

Method IV suggested three approaches for computing static eccentricity severity. The method employed RMS voltages measured from four stray flux sensors, located equidistantly around the generator's circumference. In the simulated models, the results varied. For the laboratory generator models exhibiting only static eccentricity fault, Approach 3 yielded the best results, with absolute errors of only 1 - 2 %. For the industrial generator models, which all solely exhibited static eccentricity, all three approaches resulted in similar computed severities, underestimated by 7 - 20 %. There was a trend were higher severity resulted in larger absolute error for both model types. The laboratory generator models exhibiting both static eccentricity and field-joints had the largest and most dispersed absolute errors. For healthy field-joints, the method satisfactorily computed the severity with an error of only 1 %, but the application of field-joint fault led to a maximum absolute error of 35 %. When Method III was tested on stray flux data from real generators, the computed severities were 80 % and 40 %, much larger than what is anticipated to be the actual value.

The fifth and last method, Method IV, suggested an adapted method for data mining to calculate the angular position of a static eccentricity fault, by utilizing radii of gyration computed from four stray flux sensors. In the simulations, the maximum absolute error for the models exhibiting only static eccentricity was 26 %. In the models with both static eccentricity and field-joints, the error was larger and more dispersed. The method's absolute error did not depend on the health state of the field-joints. One model with faulty field-joints, where the angular position was directly on a field-joint, had an absolute error of 131°, indicating that the influence of static eccentricity is intercepted by the more potent influence of the field-joints.

An analysis was performed with different sensor locations. Static eccentricity severity and angular position were recomputed. Based on simulations, it was concluded that a sensor displacement of 45° from the original 90° distribution, caused errors too large to accept. A displacement of 5°, however, rendered little effect on the computed results.

Finally, an algorithm was proposed in the form of a flow chart, to detect and diagnose static eccentricity and field-joint fault. The algorithm detects faulty field-joints and may also detect and diagnose static eccentricity. If the generator does not have field-joints, static eccentricity severity and angular position can be computed by means of Method IV and Method V. If it has healthy field-joints, the static eccentricity severity may be calculated but the computation of static eccentricity angular position is unreliable. If the field-joints are faulty, the computation of static eccentricity severity and angular position may be performed, but the results must be scrutinized as they may have high inaccuracy.

Bibliography

[1] Statistisk Sentralbyrå. *Table 12824 Electricity balance (MWh) 2010M01 - 2022M12.* 2023. Retrieved from https://www.ssb.no/statbank/table/12824.

[2] I. N. Nergård. *Detection and operational problems of damaged stator core field-joints in hydroelectric generators through analysis of the stray magnetic field.* M.S. preproject report, Norwegian University of Science and Technology, 2022.

[3] G. C. Stone, I. Culbert, E. A. Boulter, H. Dhirani. *Electrical insulation for rotating machines: design, evaluation, aging, testing and repair.* Published by *IEEE Press*, 2014.

[4] H. Ehya. *A Novel Health Monitoring System for Synchronous Generators using Magnetic Signatures.* Ph.D. dissertation, Norwegian University of Science and Technology, 2022. Accessible at https://hdl.handle.net/11250/3021850.

[5] H. Ehya, J. Faiz. *Electromagnetic analysis and condition monitoring of synchronous generators.* Published by Wiley-IEEE Press, 2023.

[6] H. Ehya, A. Nysveen and J. Daviu. *Advanced fault detection of synchronous generators using stray magnetic field.* Published by IEEE Press, 2022. DOI: 10.1109/TIE.2021.3118363.

[7] C. Jiang, S. Li and T. Habetler. *A review of condition monitoring of induction motors based on stray flux.* Published by IEEE Press, 2017.

[8] D. P. Kothari and I. J. Nagrath. *Electric machines (fifth edition).* Published by MacGraw Hill Education (India) Private Limited, 2018.

[9] R. Romary, D. Roger and J. F. Brudny. *Analytical computation of an AC machine external magnetic field.* Published in *European Physical Journal: Applied Physics*, issue 47, 2009.

[10] R. Romary, R. Pusca and J. P. Lecointe. *Electrical machines fault diagnosis by stray flux analysis.* Published by IEEE, 2013. DOI: 10.1109/WEMDCD.2013.6525184.

[11] D. Thailly, R. Romary and J. F. Brudny. *Diagnosis of induction machines: definition of health machine electromagnetic signature.* Published in *Recent Development of Electrical Drives* by Springer, 2006.

[12] H. Ehya and A. Nysveen. *Comprehensive broken damper bar fault detection of synchronous generators*. Published in *IEEE Transactions on Industrial Electronics*, vol. 69, 2021. DOI: 10.1109/TIE.2021.3071678.

[13] H. Ehya, A. Nysveen and J. A. Antonino-Daviu. *Static, dynamic and mixed eccentricity faults detection of synchronous generators based on advanced pattern recognition algorithm.* Published by *IEEE*, 2021. DOI: 10.1109/SDEMPED51010.2021.9605488.

[14] H. Ehya and A. Nysveen, *Pattern recognition of interturn short-circuit fault in a synchronous generator using magnetic flux*. Published in *IEEE Transactions on Industry Applications*, vol. 57, no. 4, 2021.

[15] J. G. Proakis and D. K. Manolakis. *Digital signal processing (fourth edition) (Pearson New International Edition)*. Published by Pearson, 2014.

[16] J. Pyrhönen, T. Jokinen and V. Hrabovcová. *Design of rotating electrical machines*. Published by John Wiley & Sons, 2008.

[17] NVE: Norges vassdrags- og energidirektorat, *Vannkraft*. Retrieved from https://www.nve.no/energi/energisystem/vannkraft/ on 13. December 2022.

[18] I. L. Groth. *On-line magnetic flux monitoring and incipient fault detection in hydropower generators*. M.S. thesis, Norwegian University of Science and Technology, Trondheim, 2019.

[19] G. L. Rødal, *Online condition monitoring of synchronous generators using vibration signal*. M. S. preproject report. Norwegian University of Science and Technology, Trondheim, 2019.

[20] Personal communication, Geir Aalvik in Statkraft, 01. November 2022.

[21] Personal communication, Arne Nysveen, 6. October 2022, 13. December 2022.

[22] Personal communication, Arne Nysveen, 6. March 2023, 24. April 2023, 5. June 2023.

[23] Personal communication, Hossein Ehya, 24. April 2023, 22. May 2023.

[24] A. Roque, J. Maia, D. M. Sousa, G. D. Marques and E. Margato. *Characterization of the fringing window of a magnetic core*. Published by IEEE, 2011. DOI: 10.1109/EUROCON.2011.5929404.

[25] C. R. Sullivan. *Fringing effects*. PowerPoint slides from the *Power magnetics @ high frequency workshop 2018*, organized by the PSMA: Power Sources Manufacturers Association. Slides retrieved from https://cpb-us-e1.wpmucdn.com/sites.dartmouth.edu/dist/c/87/files/2018/03/fringing-sullivan-2018.pdf on 17. December 2022.

[26] P. Stoica and R. Moses. *Spectral analysis of signals*. Published by Prentice Hall, 2005. ISBN: 0-13-113956-8.

[27] COMSOL. *The Finite Element Method (FEM).* Part of the digital series *Multiphysics Cyclopedia.* Retrieved from https://www.comsol.com/multiphysics/finite-element-method on 17. April 2023.

[28] Ansys. *Ansys Maxwell: low frequency EM field simulation.* Retrieved from https://www.ansys.com/products/electronics/ansys-maxwell on 25. April 2023.

[29] Indiamart. *Armature core lamination.* Illustration retrieved from https://www.indiamart.com/globeengineering-hyderabad/electrical-motor-lamination.html#6733681088 on 06. April 2023.

[30] M. M. Znidarich. *Hydro generator stator cores part 1 - constructional features and core losses.* Published by IEEE, 2008.

[31] Electrical Academia. *Synchronous generator working principle.* Illustration retrieved from http://electricalacademia.com/synchronous-machines/synchronous-generator-working-principle/ on 08. April 2023.

[32] Y.-L. He, et al. *A new external search coil based method to detect detailed static air-gap eccentricity position in nonsalient pole synchronous generators.* Published in *IEEE Transactions on Industrial Electronics*, vol. 68, no. 8, pp. 7535-7544, 2021. DOI: 10.1109/TIE.2020.3003635.

[33] I. Sadeghi, H. Ehya, J. Faiz. *Eccentricity fault indices in large induction motors: an overview.* Published by IEEE, 2017. DOI: 10.1109/PEDSTC.2017.7910347.

[34] Electric Power Research Institute (EPRI). *Main generator on line monitoring and diagnostics.* Technical report, 1996.

[35] A. C. Smith, D. Bertenshaw, C. W. Ho, M. Sasic *Detection of stator core faults in large turbo-generators.* Published by IEEE, 2009. DOI: 10.1109/IEMDC.2009.5075290.

[36] M. Kazimierczuk, H. Sekiya. *Design of AC resonant inductors using area product method.* Published by IEEE, 2009. DOI: 10.1109/ECCE.2009.5316501.

[37] J. Skaar. *Elektromagnetisme.* Compendium for the course TFE4120 Electromagnetism. Norwegian University of Science and Technology, 2017.

[38] E. Kreyszig. *Advanced engineering mathematics.* Tenth edition. Published by John Wiley & sons, 2011.

[39] R. Povinelli, J. Bangura, N. Demerdash and R. Brown. *Diagnostics of bar and end-ring connector breakage faults in polyphase induction motors through a novel dual track of time-series data mining and time-stepping coupled FE-state space modeling.* Published by IEEE, 2002.

[40] R. Bangura, R. Povinelli, J. Demerdash and R. Brown. *Diagnostics of eccentricities and bar/end-ring connector breakages in polyphase induction motors through a combination of time-series data mining and time stepping coupled FE-state space techniques.* Published by IEEE, 2003.

[41] S. Chakrabarti et al. *Data mining curriculum: a proposal (Version 1.0).* The Association for Computing Machinery's Special Interest Group on Knowledge Discovery and Data Mining (SIGKDD). 2006. PDF accessible at https://kdd.org/exploration_files/CURMay06.pdf on 28. April 2023.

[42] A. Hasan, M. Meia and M. Mostafa. *Applications of Fourier series in electric circuit and digital multimedia visualization signal process of communication system.* Published in *American Journal of Circuits, Systems and Signal Processing*, Vol. 4, No. 4, pp. 72-80, 2018.

[43] S. Tumanski. *Induction coil sensors - a review.*

[44] O. Kokoko et al. *Detection of short circuits in the rotor field winding in large hydro generator*, in *Proceedings of the 2018 XIII International Conference on Electrical Machines*, 2018.

[45] L. Bain and M. Engelhardt. *Introduction to probability and mathematical statistics. PDF manual.* 2nd edition. Published by Brooks/Cole, 1992.

[46] P. Gnacinski, M. Peplinski and M. Szweda. *The effect of subharmonics on induction machine heating*, 2008. Presented at the 13th International Power Electronics and Motion Control Conference, Poznan, Poland, 2008, pp. 826-829, DOI: 10.1109/EPEPEMC.2008.4635369.

[47] D. J. Griffiths. *Introduction to electrodynamics.* 3rd edition. Published by Prentice-Hall, 1999. ISBN: 0-13-805326-X.

[48] A. E. Fitzgerald, Jr. C. Kingsley and S. D. Umans. *Electric Machinery.* 6th edition. Published by McGraw-Hill, 2003. ISBN: 0-07-366009-4

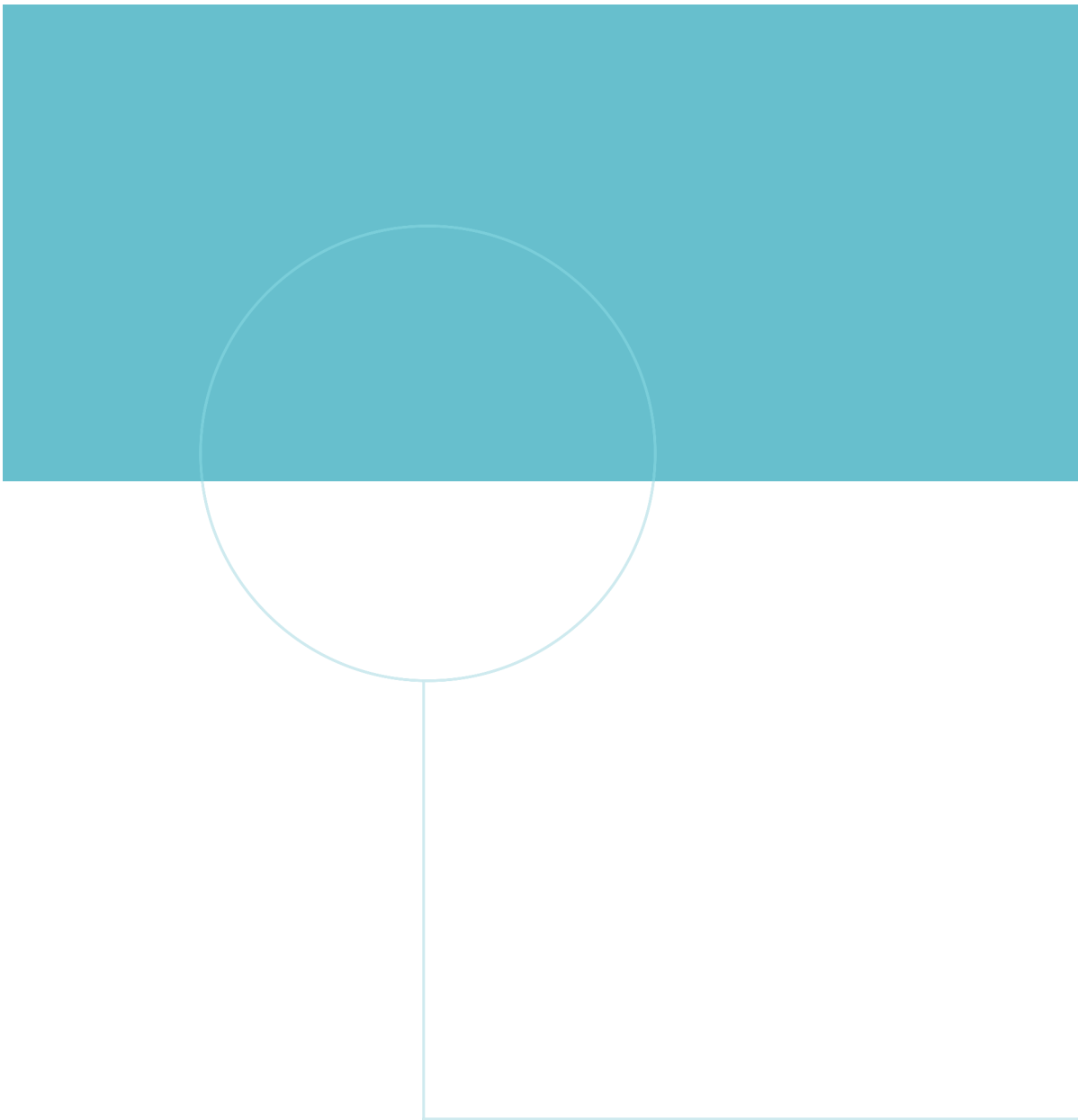

NTNU

Kunnskap for en bedre verden